

**FIELD INHOMOGENEITY COMPENSATION IN HIGH FIELD MAGNETIC
RESONANCE IMAGING (MRI)**

by

Zhenghui Zhang

B.Eng, Shanghai Jiao Tong University, 1998

Submitted to the Graduate Faculty of
School of Engineering in partial fulfillment
of the requirements for the degree of
Doctor of Philosophy

University of Pittsburgh

2006

UNIVERSITY OF PITTSBURGH
SCHOOL OF ENGINEERING

This dissertation was presented

by

Zhenghui Zhang

It was defended on

August 14, 2006

and approved by

George D. Stetten, M.D., Ph.D., Associate Professor, Department of Bioengineering

Fernando E. Boada, Ph.D., Associate Professor, Departments of Radiology and Bioengineering

William F. Eddy, Ph.D., Professor, Carnegie Mellon University Department of Statistics

V. Andrew. Stenger, Ph.D., Associate Professor, University of Hawaii, Departments of Medicine

Dissertation Director

Copyright© by Zhenghui Zhang
2006

ABSTRACT

FIELD INHOMOGENEITY COMPENSATION IN HIGH FIELD MAGNETIC RESONANCE IMAGING (MRI)

Zhenghui Zhang, PhD

University of Pittsburgh, 2006

This thesis concentrates on the reduction of field (both main field B_0 and RF field B_1) inhomogeneity in MRI, especially at high B_0 field. B_0 and B_1 field inhomogeneity are major hindrances in high B_0 field MRI applications. B_1 inhomogeneity will lead to spatially varying signal intensity in the MR images. B_0 inhomogeneity produces blurring, distortion and signal loss at tissue interfaces. B_0 artifacts are usually termed off-resonance or susceptibility artifacts. None of the existing methods can perfectly correct these inhomogeneity artifacts.

This thesis aims at developing three-dimensional (3D) tailored RF (TRF) pulses to mitigate these artifacts. A current limitation in the use of 3D TRF techniques, however, is that pulses are often too long for practical clinical applications. Multiple transmission techniques are proposed to decrease pulse lengths and provide an inherent correction for B_1 inhomogeneity. Shorter pulses are also more robust to profile distortions from susceptibility effects.

Specifically, slice-selective 3D TRF pulses for multiple (or “parallel”) transmitters were designed and validated in uniform phantom and human brain experiments at 3 Tesla. A pseudo-transmit sensitivity encoding (“transmit SENSE”) method was introduced using a body coil

transmitter and multiple receivers to mimic the real parallel transmitter experiment. The k_z -direction was controlled by fast switching of gradients in a fashion similar to Echo planar imaging (EPI). The transverse plane (k_x - k_y) was sampled sparsely with hexagonal trajectories, and accelerated with the transmit SENSE method. The transmit SENSE 3D TRF pulses reduced the B_1 inhomogeneity compared to standard SINC pulses in human brain scans. The undersampled transmit SENSE pulses were only 4.3ms long and could excite a 5mm thick slice, which is very promising for clinical applications. Furthermore, these pulses are shown by numerical simulation to have promise in correcting through-plane susceptibility artifacts.

TABLE OF CONTENTS

ACKNOWLEDGEMENT	xvi
1.0 INTRODUCTION	1
1.1 THE USES OF HIGH FIELD MAGNETIC RESONANCE IMAGING.....	1
1.2 PROBLEMS OF HIGH FIELD MRI	1
1.3 SIGNIFICANCE OF THIS THESIS	2
1.4 THE AIMS OF THIS THESIS	3
2.0 BACKGROUND	4
2.1 INTRODUCTION	4
2.2 MR PHYSICS.....	4
2.2.1 Spin Systems.....	4
2.2.2 Interaction with External Magnetic Fields.....	6
2.2.3 Relaxation	7
2.2.4 Rotating Frame.....	10
2.2.5 The Bloch Equation	11
2.3 EXCITATION	12
2.3.1 Basic Excitation Principles	13
2.3.2 On-Resonance Excitation.....	13
2.3.3 Off-Resonance Excitation.....	15
2.4 SIGNAL RECEPTION.....	16

2.4.1 Faraday’s Law and the Reciprocity Law	16
2.4.2 Free Induction Decay (FID).....	18
2.4.3 Frequency Encoding	18
2.4.4 Phase Encoding.....	19
3.0 IMAGE RECONSTRUCTION AND PARALLEL IMAGING.....	20
3.1 INTRODUCTON.....	20
3.2 <i>k</i> -SPACE	20
3.2.1 Cartesian Grid	21
3.2.2 Non-Cartesian Sampling.....	23
3.3 SAMPLING REQUIREMENTS	25
3.3.1 Nyquist Criteria.....	25
3.3.2 Aliasing.....	26
3.3.3 Variable Density Sampling.....	27
3.4 PARALLEL IMAGING	29
3.4.1 Coil Sensitivity.....	32
3.4.2 SNR and g-Factor	34
4.0 RF PULSE DESIGN.....	36
4.1 INTRODUCTION	36
4.2 THE SMALL-TIP ANGLE APPROXIMATION	36
4.2.1 Fourier Relationship.....	36
4.2.2 <i>k</i> -Space Interpretation	38
4.3 TWO-DIMENSIONAL PULSE DESIGN	41
4.3.1 Spiral Pulse	42

4.3.2 Off-Center Excitation.....	46
4.4 3D TAILORED RF PULSE DESIGN.....	47
4.4.1 Separable Design.....	47
5.0 TRANSMIT SENSE.....	52
5.1 TRANSMIT SENSE FORMULISM.....	52
5.2 TRANSMIT SENSE NUMERICAL SIMULATION.....	54
5.3 PSEUDO-TRANSMIT SENSE.....	56
5.4 VARIABLE DENSITY EXCITATION WITH TRANSMIT SENSE.....	60
5.5 SPECIFIC ABSORPTION RATE (SAR).....	61
6.0 REDUCTION OF B ₁ INHOMOGENEITY WITH TRANSMIT SENSE SLICE-SELECT PULSES.....	64
6.1 INTRODUCTION.....	64
6.2 THEORY.....	66
6.3 METHODS.....	69
6.4 RESULTS.....	73
6.5 DISCUSSION AND CONCLUSIONS.....	81
7.0 B ₀ INHOMOGENEITY CORRECTION WITH TRANSMIT SENSE 3D TRF PULSES IN ULTRA-HIGH FIELD MRI.....	83
7.1 INTRODUCTION.....	83
7.2 THEORY.....	84
7.3 METHOD.....	85
7.4 RESULTS.....	87
7.5 DISCUSSION and CONCLUSIONS.....	91

8.0 CONCLUSIONS.....	92
8.1 KEY CONTRIBUTIONS.....	92
8.2 FUTURE DIRECTIONS.....	94
APPENDIX A.....	96
OBSERVATION OF OFF-RESONANCE BLURRING IN SPIRAL IMAGING.....	96
BIBLIOGRAPHY.....	102

LIST OF TABLE

Table 1: Full width at half maximum (FWHM) of histograms as well as standard deviations (SD) divided by the mean of the image magnitudes of the slices shown in Fig. 6.6. Also shown are p-values from a t-test between the respective column and the corresponding Transmit SENSE slices.	79
--	----

LIST OF FIGURES

Figure 2.1: Longitudinal relaxation characterized by a time constant T_1 of 1000 ms.	9
Figure 2.2: Transverse relaxation decay after a 90^0 -tip characterized by a time constant T_2 of 200 ms and T_2^* of 50 ms.	9
Figure 3.1: (a) A FLASH (gradient echo) sequence. The frequency encoding gradient is applied along the x-axis, and the phase encoding gradient is applied along the y-axis.(b) The Cartesian k -space defined by the FLASH sequence in (a). Corresponding time points are plotted in both figures to illustrate how k -space is filled by the gradients.	22
Figure 3.2: (a) One of the 24 arms of the interleaved spiral trajectory in k -space. (b) The corresponding gradients along the x and y axis for one arm. (c) The time map in k -space. The gray scale in this time map corresponds to the readout time from 0 (k -space center) to 5.8 ms (k -space edges) (d) The sampling density in k -space. The k -space is not uniformly sampled by the spiral trajectory. During reconstruction, this non-uniform sampling needs to be compensated.	24
Figure 3.3: The interpretation how aliasing artifact generated with numerical simulation. (b) and (d) show the reconstructed phantom images using the sampling schemes represented in (a) and (c) respectively.	27
Figure 3.4: The high frequency components of k -space define the details of the image. Image in (d) is much sharper than image in (b), because more lines are acquired at the edge k -space in (c) than in (a).	28
Figure 3.5: Comparison of the (a) uniform spiral and (b) variable density spiral trajectory. Reducing sampling density at k -space edges dramatically reduce the sampling points, which is at the expense of a little bit blurring of the reconstructed image.	28
Figure 3.6: The GRAPPA reconstruction phantom data using 4-channel GE Cardiac coil. The 2 fold undersampled k -space (a) and its Fourier transform (b) are shown in the first row. The GRAPPA recovered k -space (c) and its Fourier transform (d) are shown in the second row. The third row shows the GRAPPA reconstructed images with k -space reductions from 1 to 4. We can see the SNR becomes lower and the residue aliasing becomes larger as the reduction factor becomes bigger.	30
Figure 3.7: The sensitivity maps of a commercial 3T phased array coil estimated with (a) the conventional smoothed array/body ratio method; (b) the iterative fitting method.	32

Figure.3.8: a-d: (top) Normalized low-resolution images obtained from the $2\times$ undersampled data in a k-space center of radius $4/\text{FOV}$, acquired with a four-element coil array. e-h: (middle) Corresponding normalized low-resolution images from fully sampled data. i-l: (bottom) The difference between the top and middle images, with an average error of 4%. All images are displayed with the same window/level. The slight difference indicates that the undersampling artifacts at k-space size of $4/\text{FOV}$ are marginal 34

Figure. 4.1: The k-space interpretation of RF pulse.(45)..... 40

Figure 4.2: k-space trajectory design. (a) the single-shot spiral k-space. (b) the image space (45). 42

Figure 4.3: a) Single-shot spiral with a 22cm FOV and 6.9mm resolution. b) Its corresponding gradients G_x, G_y 43

Figure 4.4: a) The spiral RF pulse and its phase. b) The point-spread-function in mesh plot. 45

Figure 4.5: a) The point spread function of the spiral pulse in a extended FOV so that we can see side lobes. b) The profile from the center line of a). We can see the first side lobe appears at $\pm 22\text{cm}$, which is the defined excitation FOV. 45

Figure 4.6: The shift FOV by modulation..... 46

Figure 4.7: The 3D tack spirals trajectory. The transverse plan is sampled with spiral trajectory, and the through-plan is covered using phase encoding. 47

Figure 4.8: The 3D EPI trajectory. The through-plan is sampled densely with frequency encoding, and the transverse plan is sampled sparsely with a hexagonal trajectory. 49

Figure 4.9: 3D TRF pulse designs. (a) Diagram of the RF magnitude envelope and (b) Diagram of the RF magnitude envelope. 50

Figure 4.10: a) The hexagonal trajectory used in transverse plane, and b) its point spread function. 51

Figure 5.1: Transmit SENSE simulation. (a) Input jpeg image. (b) (Top) Sensitivity maps measured from array coil displayed as real and imaginary images. (Bottom) Real and imaginary magnetization profiles from Bloch equation simulations. (c) Complex summation of the magnetization from all transmitters. 55

Figure. 5.2: The point spread function profile of the 3D EPI pulse. The resolution is increased with the SENSE reduction factor. 56

Figure 5.3: (a) One of the eight pulses we applied. This pulse used a spiral trajectory to achieve high resolution in transverse plane, and was embedded into a spin-echo sequence. (b) The 8

individual images resulted by the 8 pulses on corresponding coil elements. (c) The complex sum of the 8 images in Fig. 2, which is the R=3 transmit SENSE pulse image. 59

Figure 5.4: 2D L-shape transmit SENSE pulse images acquired with a SE sequence on a uniform ball phantom. The upper row uses uniform spiral trajectory with different reduction factors R from 1 to 4. The lower row uses variable density spirals that maintain the sampling density at the center k -space as that of the R=1 uniform spiral trajectory, while undersampled at the edges of k -space. RF pulse lengths are shown underneath images..... 61

Figure 5.5. SAR Calculations. (a) Geometry of two coils and the head model on axial plane through level of eyes (left), and 3D shaded surface diagram (right). (b) Magnetic field magnitude (μ T) on axial plane through level of eyes (left), and mid-sagittal plane (right). White contour shows interface between tissue and air. (c) SAR magnitude (W/kg) at a resolution of $(2\text{mm})^3$ on axial plane through level of eyes (left), and mid-sagittal plane (right). (in courtesy to Dr. Collins) 63

Figure 6.2: One of the eight R=2 transmit SENSE pulses used in human brain images. The rows from top to bottom are the real and imaginary parts of the RF, and the x , y , and z gradients. 69

Figure 6.3: The coil sensitivity of the eight-channel phased array coil (up row), and the eight individual coil images of a R=2 transmit SENSE 3D TRF pulse. The complex sum of the eight images is shown as Slice 1 in Fig. 6.6 71

Figure 6.4: The slice profile along the z axis. (a) The transmit SENSE 3D TRF pulse image with readout in z direction. (b) The z profile from the center line of image (a). The fitted Gaussian has a FWHM of 4.7 mm which is very close to the prescribed 5 mm slice thickness..... 74

Figure 6.5: The uniform ball phantom images acquired with the transmit SENSE 3D TRF pulses (a) and the SINC pulse (b-d). The three SINC pulse images are complex sum (b) and sum of squared (c) images of the phased array receiver and the body coil receiver image (d). The histograms of the four images in (a-d) are shown in (e) with the FWHM measurements shown in the legend. 76

Figure 6.6: Four slices generated with the $R=1$ transmit SENSE pulses and by the complex and magnitude sums using the standard pulse. Images acquired with the transmit SENSE pulses are more uniform than those generated using the other two methods. 78

Table 1: Full width at half maximum (FWHM) of histograms as well as standard deviations (SD) divided by the mean of the image magnitudes of the slices shown in Fig. 6.6. Also shown are p-values from a t-test between the respective column and the corresponding Transmit SENSE slices. 79

Figure 6.7: Histograms of the distribution of image magnitude among the pixels in the slices shown in Fig. 5.6. The black, dashed and dotted lines correspond to the histograms from the

slices generated with the $R=1$ pulses and from the complex and magnitude sums using the standard pulse. The histograms from images acquired with the transmit SENSE pulses are narrower, indicative of a more homogeneous distribution of pixel magnitudes..... 80

Figure 6.8: The images acquired with the $R=1$ (Left) and $R=1.5$ (Right) transmit SENSE 3D TRF pulses. The image of the $R=1.5$ pulses is more inhomogeneous than that of the $R=1$ pulses..... 81

Figure 7.1: The sensitivity map from an eight-channel phased array coil..... 86

Figure 7.2: (a, b) True image and through plane phase at 3T. (c-e) Phase excitation produced by Bloch equations simulation of $R=1$ 34.3 ms, $R=2$ 10.7 ms, and $R=1$ 10.7 ms transmit SENSE 3D TRF pulses, respectively. The 10.7 ms $R=2$ pulse produces the desired result. Note that in a real experiment we will tailor minus the phase to cancel the phase on (b)... 88

Figure 7.3: The numerical simulation with a regular 3D TRF pulse with 54.4 ms long. (a) The magnitude and phase of the 3D TRF pulses. (b) The simulated phase of the 3D transverse magnetization M_{xy} . (c) The through-plane phase profile from one point in sinus region of the simulated phase..... 89

Figure 7.4: The numerical simulation with an $R=2$ transmit SENSE 3D TRF pulses with 17.5 ms long. (a) The magnitude and phase of one of the eight transmit SENSE 3D TRF pulses. (b) The simulated phase of the 3D transverse magnetization M_{xy} . (c) The through-plane phase profile from one point in sinus region of the simulated phase..... 90

Figure A.1: The blurred FWHM vs. the original FWHM (a), and vs. the off-resonance frequency (b). At a certain off-resonance frequency, there is a minimum blurred FWHM achieved... 97

Figure A.2: Profiles of round discs (Gaussian intensity profile) with different sizes were plotted in (a). The upper row is the original profile, and the lower row is the corresponding profiles blurred with 200Hz off-resonance. The blurred FWHM vs. original FWHM was plotted in (b). The measurements from the numerical simulation are in squares, and analytical solution from equation (A.1) is in spaces. The two types of measurements match each other as we expected..... 97

Figure A.3: Numerical simulation of round discs (rectangular profile) with different sizes ($r=1, 1.25, 1.5, 1.75, 2, 2.25, 2.5, 2.75$ pixels) were blurred with off-resonance frequency 0(a), 50Hz(b), 100Hz(c), 150Hz(d), 200Hz(e). Profiles along the round disc ($r=1.75$) were plotted correspondingly in (f-j). The blurred FWHM vs. off-resonance frequency was plotted in (k). A minimum FWHM is achieved when off-resonance is 150Hz..... 98

Figure A.4: The bottle phantom with gadolinium filled tubes inside was imaged at the center frequency (a). The profiles along the center bright dot with different off-resonance frequencies were plotted in (b). The FWHM vs. the off-resonance frequency was plotted in (c). The phantom measurements (space) and the numerical simulation data (square) have the

same trend, and the former are slightly larger than the latter. This difference might be caused by the DC component of the inhomogeneity and field variance of the scanner. 100

ACKNOWLEDGEMENT

I would like to use this opportunity to thank all the people who helped and supported me. I am greatly indebted to Dr. V. Andrew Stenger, my academic advisor. He is a great mentor. He taught me not only how to do research but also how to be a good person. He is always patient and considerate. He is an expert to inspire people and creates a great working environment for me. I really enjoy the time to work with him.

I want to thank other members in my committee: Dr. Boada, Dr. Steten and Dr. Eddy for their time and comments on my dissertation. I want to thank Dr. Yi Wang for his training and help.

I would also like to thank my lab-mates in Pittsburgh and Honolulu: Suwit Saekho, Yongxian Qian, Shaolin Yang, Pascal Spincemaille, Thanh Ngyuen, Weiyin Dai, Mingjie Wu, Cecil Yan, He Zhu, Azma Mareyam, Ryan Brown, and Anthony Nuval in Pittsburgh; Napapon Sailasuta, Laura Girton, Renat Yupov, Kenneth Yu in Honolulu for their friendship and help.

Finally, I want to say thank you to my family. My parents always support and trust me. They are always standing behind me and giving me strength. My biggest thank you goes to my wife, Sheng Chen, and son, Ken. They are the source of my happiness and motivation. My wife sacrificed her own college study to move together with me to Honolulu, Hawaii, and the next stop will be Waukesha, Wisconsin. She also brought me my dearest son, Ken, who came to this world three months ago. Without them, I could never accomplish this dissertation. I want to dedicate this thesis to my wife and son.

1.0 INTRODUCTION

1.1 THE USES OF HIGH FIELD MAGNETIC RESONANCE IMAGING

Increased image signal to noise ratio (SNR) (1-3), contrast to noise ratio (CNR) (4), favorable spin-lattice relaxation time T_1 value (5) and spectral dispersion (6,7) sparks current interest in high (3-4 T) or ultra-high magnetic field (>7 T) Magnetic Resonance Imaging (MRI). The increased SNR can be traded for either increased image resolution or reduced scan time. The increased magnetic susceptibility enhances the blood oxygenation level dependent (BOLD) contrast (8-11) in fMRI at high field. Together with the increased SNR, this effect greatly increases the ability to detect signal changes due to neural activities. The increased chemical selectivity benefits Magnetic Resonance Spectroscopy (MRS) significantly. Other applications like Magnetic Resonance Angiography (MRA) also benefit from high field. At high field strengths, T_1 becomes longer, which suppresses the background in time-of-flight MRA (12).

1.2 PROBLEMS OF HIGH FIELD MRI

Although 3T MRI was recently approved by the Food and Drug Administration (FDA) for clinical use, 3T MRI is still largely restricted to research use because of a number of technical

challenges. High field strengths will cause high heat in tissue if the power is not well managed (13,14). It will also result in non-uniform intensities in images due to dielectric effects and RF attenuation. This non-uniformity of signal intensity is termed as “ B_1 inhomogeneity” in MRI (15,16). Susceptibility artifacts, although beneficial to BOLD contrast in fMRI and spectral selectivity in MRS, will degrade image quality at air/tissue or fat/tissue interface regions (17-19). All these issues must be resolved before the high field and even ultra high field MRI can be used routinely in the clinic. Details of these technical challenges will be addressed in following chapters.

1.3 SIGNIFICANCE OF THIS THESIS

At frequencies higher than 100 MHz, susceptibility artifacts and B_1 inhomogeneity artifacts become more severe and hamper applications of high field MRI systems. Susceptibility artifacts result from local field variations that usually occur at interfaces of substances with different susceptibilities. These artifacts will lead to blurring, distortion or even signal loss, especially in T_2^* -weighted images (19). There are two main factors lead to decreased RF field homogeneity within samples at high magnetic field strength. One is the shorter wavelength, further shortened by the dielectric properties of tissue, which creates a standing wave phenomenon inside the object and causes local maxima and minima inside the sample. A second factor is the attenuation of RF amplitude due to conductivity of tissue. The net result of both effects is a spatial dependence of the transmitted and received sensitivities, producing areas of increased and

decreased magnitude in the images (15,16,20,21). A more complete description of these artifacts is presented later.

The three-dimensional transmit sensitivity encoded “SENSE” Tailored Radio Frequency (TRF) pulses introduced in this thesis can reduce both B_0 and B_1 inhomogeneity at high field and ultra-high field MRI. These pulses can be made short enough to be practical for many applications. They can also excite thin slices and can be used in multi-slice 2D MRI.

1.4 THE AIMS OF THIS THESIS

(a) To develop and optimize transmit SENSE 3D TRF pulses to compensate B_0 and B_1 inhomogeneity. The desired pulse should be slice selective, can excite 3-5 mm thin slice. The pulse length should not be longer than 20 ms to use routinely in the clinic.

(b) To validate the inhomogeneity correction effects by comparing phantom and human brain images acquired with the designed transmit SENSE TRF pulse and the regular SINC pulse.

2.0 BACKGROUND

2.1 INTRODUCTION

This chapter will provide general background information about several technical aspects of MRI which will serve as the basis for further Chapters. Topics discussed in this chapter are concepts of MR physics, excitation and signal reception. The section on MR physics will introduce the basic concepts of nuclear spin systems, the interaction of spins with magnetic fields, the relaxation behavior of spins after they are excited, the rotating frame and the Bloch Equations. The excitation section will describe the magnetization behaviors under the on-resonance and off-resonance conditions. The signal reception section will discuss the underlying physics of the MRI signal, the free induction decay, and spatial encoding methods.

2.2 MR PHYSICS

2.2.1 Spin Systems

Spin is a physical property of nuclear particles like protons, electrons and neutrons. Individual unpaired nuclear particles possess a spin of $1/2$. Spins can have positive or negative signs. Two or more spins with different signs can be paired together to eliminate the net spin. In MRI

experiments, only nuclei with non-zero net spin are of importance. When placed in a static magnetic field, spins will act like magnet dipoles that will be aligned parallel or anti-parallel to the external field. The magnetic dipole moment $\boldsymbol{\mu}$ of a spin is given by

$$\boldsymbol{\mu} = -\gamma\mathbf{S} = \gamma\hbar\mathbf{I} \quad (2.1)$$

where \mathbf{S} is the spin angular momentum, and \mathbf{I} is the spin. From a classical point of view, one can imagine a charged sphere spinning about its axis, thereby giving rise to a current loop that creates the magnetic dipole moment. Spins are in the lower energy stage when aligned in the same direction of the external field, or in a higher energy stage otherwise. Particles with spin can undergo transitions between the energy stages by absorbing or releasing photons with energy

$$E = h\nu \quad (2.2)$$

where h is Planck's constant, and ν is the frequency of the photon. In MR experiments, this is also the "resonance frequency" and is called the Larmor frequency, which is

$$\nu = \frac{\omega}{2\pi} = \frac{\gamma}{2\pi} B_0 \quad (2.3)$$

where γ is called the gyromagnetic ratio which is 42.56 MHz/Tesla for proton MRI. The corresponding Larmor frequency is approximately 64 MHz at 1.5T, and 128 MHz at 3.0T.

The energy and spin temperature determine the ratio of the number of particles in the lower energy state N^- to number in the higher energy state N^+ :

$$\frac{N^-}{N^+} = e^{-\frac{E}{kT}} \quad (2.4)$$

The difference of N^+ and N^- gives rise to the magnetization, which is discussed below. In MR experiments, the nuclei will interact with three types of magnetic fields: the main magnetic field B_0 , the excitation RF field B_1 and the gradient fields G .

2.2.2 Interaction with External Magnetic Fields

In MRI it is convenient for us to consider the local magnetic dipole moment per unit volume, or magnetization

$$\mathbf{M} = \sum \boldsymbol{\mu} \quad (2.5)$$

In static magnetic field, the torque that \mathbf{M} experiences from the external B_0 results in nuclear precession at the Larmor frequency. Macroscopically, the sample will be polarized by the B_0 field. If there is no other magnetic field, the net magnetization vector will point to in the same direction as the B_0 field, usually assigned as the z direction. This magnetization is called the equilibrium magnetization M_0 .

When an excitation RF field B_1 is added at the Larmor frequency, a resonance condition is met. The magnetization will be tipped away from the z direction at an angle of a certain degree. The equilibrium is broken because the rotating magnetic field B_1 induces a torque on the magnetization resulting in a net transverse magnetization. The magnetization will rotate about the z direction at the Larmor frequency, and eventually come back to the equilibrium state. This motion is called precession. The recovery process of the magnetization along the z axis, which is called the longitudinal magnetization (M_z), is characterized by an exponential curve with a time constant T_1 . At the same time, the magnetization in the xy plane, called the transverse magnetization (M_{xy}), will decay at the rate characterized by a constant T_2 .

To have spatial resolution of the object, the spatial information has to be encoded. In 1973, Lauterbur *et al.* introduced linear gradient magnetic fields into NMR experiments, and

demonstrated the first MR image on small test tube samples using back projection reconstruction (22). These gradient fields make the Larmor frequencies of the spins become a function of spatial location. Two years later, Ernst et al. proposed the classic Cartesian frequency and phase encoding methods using gradient magnetic fields as well. Images can be easily obtained by the Fourier Transform (23).

2.2.3 Relaxation

In the presence of a static magnetic field, the magnetization tries to stay in the equilibrium state. The transition back to equilibrium after a perturbation is called relaxation. The recovery of the longitudinal magnetization M_z to its equilibrium state is called longitudinal relaxation, also named the spin lattice relaxation. The longitudinal magnetization behavior is defined by:

$$\frac{dM_z}{dt} = -\frac{M_z - M_0}{T_1} \quad (2.6)$$

Given the initial condition that $M_z(0)$ right after a 90° RF pulse is zero, the solution of this equation will be

$$M_z = M_0(1 - e^{-t/T_1}) \quad (2.7)$$

where T_1 is the spin–lattice relaxation time constant of the imaging sample. T_1 in tissue is typically longer at higher field strengths than that of the lower field and M_z takes longer to recover (24). The behavior of longitudinal relaxation shows in Figure 2.1.

At the same time of longitudinal relaxation, the transverse magnetization will decay to zero at an exponential rate of T_2 . Unlike the case of longitudinal relaxation, energy remains within the spin

system. The behavior is called transverse relaxation, or spin-spin relaxation. The equation describing this relaxation will be:

$$\frac{dM_{xy}}{dt} = -\frac{M_{xy}}{T_2} \quad (2.8)$$

This is just an exponentially decayed function:

$$M_{xy} = M_0 e^{-t/T_2} \quad (2.9)$$

where T_2 is the spin-spin time constant. T_2 in tissue is typically independent of field strength because the decay is caused by loss of phase coherence. The behavior of the transverse component decay shows in Figure 2.2.

In an MRI experiment, we cannot see the pure T_2 effects because the transverse magnetization decay is a result of both the spin interactions and the B_0 inhomogeneity. The combined time constant is called T_2^* , which is related to T_2 by:

$$\frac{1}{T_2^*} = \frac{1}{T_2} + \frac{1}{T_2'} \quad (2.10)$$

The two relaxations occur simultaneously. For the same species, the T_2 value is always less than or equal to the T_1 value (24).

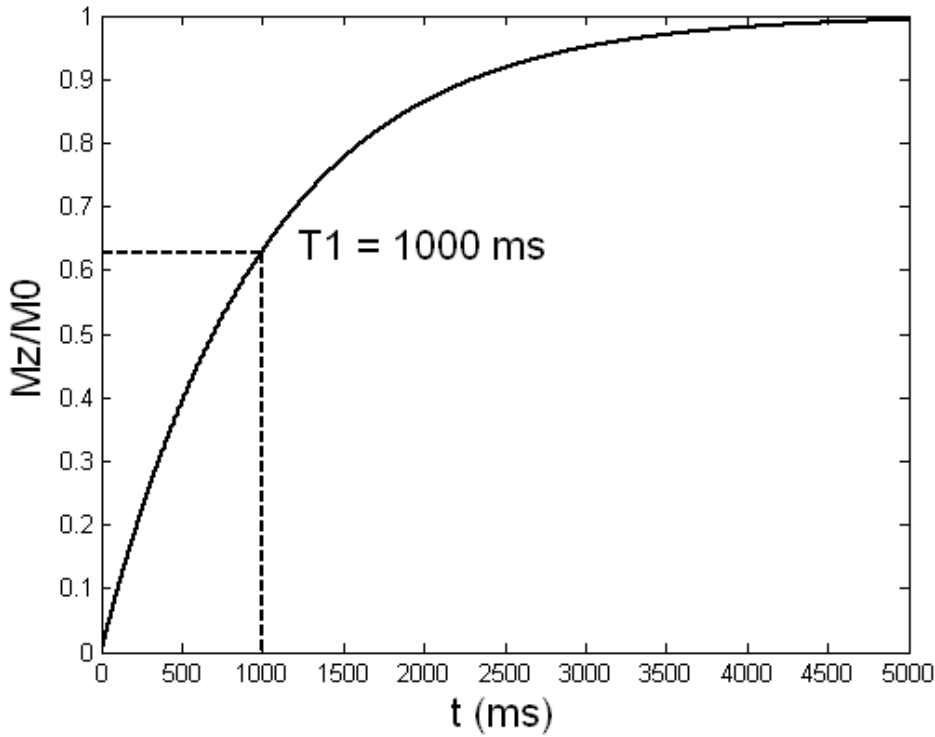


Figure 2.1: Longitudinal relaxation characterized by a time constant T_1 of 1000 ms.

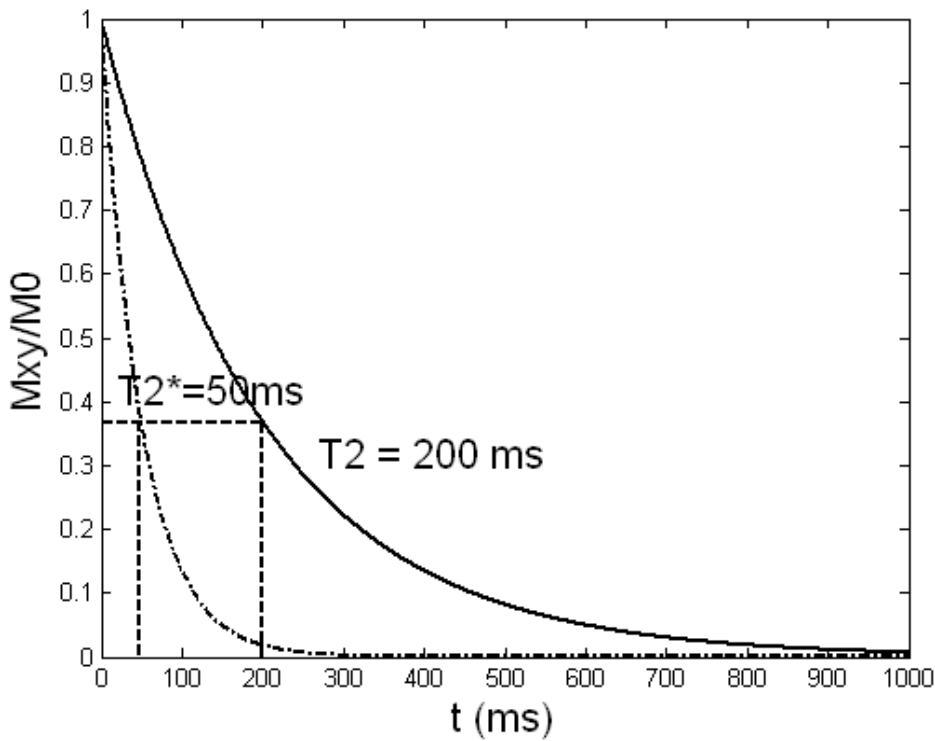


Figure 2.2: Transverse relaxation decay after a 90° -tip characterized by a time constant T_2 of 200 ms and T_2^* of 50 ms.

2.2.4 Rotating Frame

It is easier to describe the time dependence of magnetization in a rotating frame of reference instead of the previously used laboratory coordinates. The rotating frame is defined to rotate about the z -axis at the Larmor frequency clockwise. Mathematically, the rotation can be expressed by a rotation matrix:

$$\mathbf{R}_{3D} = \begin{bmatrix} \cos(\omega t) & -\sin(\omega t) & 0 \\ \sin(\omega t) & \cos(\omega t) & 0 \\ 0 & 0 & 1 \end{bmatrix} \quad (2.11)$$

Let us define the original and rotating coordinate as column vectors \mathbf{r} and \mathbf{r}' :

$$\mathbf{r} = \begin{bmatrix} x \\ y \\ z \end{bmatrix}, \text{ and } \mathbf{r}' = \begin{bmatrix} x' \\ y' \\ z' \end{bmatrix} \quad (2.12)$$

Then the rotating frame is related to the original frame by:

$$\mathbf{r}' = \mathbf{R}_{3D} \mathbf{r} \quad (2.13)$$

The RF field \mathbf{B}_1 is only applied in the transverse plane at the Larmor frequency. In the rotating frame, the \mathbf{B}_1 field will always be applied along a fixed axis. We assign this axis as y' . In matrix form,

$$\mathbf{B}_1 = \begin{bmatrix} B_{1x} \\ B_{1y} \end{bmatrix}, \mathbf{B}_{1\text{rot}} = \begin{bmatrix} B_{1,x'} \\ B_{1,y'} \end{bmatrix}, \mathbf{R}_{2D} = \begin{bmatrix} \cos(\omega t) & -\sin(\omega t) \\ \sin(\omega t) & \cos(\omega t) \end{bmatrix} \quad (2.14)$$

and

$$\mathbf{B}_{1\text{rot}} = \mathbf{R}_{2D} \mathbf{B}_1 \quad (2.15)$$

Another way to describe the rotating frame is to use complex notation. Defining the transverse magnetization as

$$M_{xy} = M_x + iM_y, \text{ and } M_{x'y'} = M_{x'} + iM_{y'} \quad (2.16)$$

Then

$$M_{x'y'} = M_{xy} e^{i\omega t} \quad (2.17)$$

In the same way, the RF field B_1 will be

$$B_{1,rot} = B_1(t) e^{i\omega t} \quad (2.18)$$

where $B_I = B_{I,x} + iB_{I,y}$ and $B_{1,rot} = B_{1,x'} + iB_{1,y'}$.

2.2.5 The Bloch Equation

The motion of magnetization vector can be described using the Bloch equation:

$$\frac{d\mathbf{M}}{dt} = \gamma \mathbf{M} \times \mathbf{B} - \frac{M_x \mathbf{i} + M_y \mathbf{j}}{T_2} - \frac{(M_z - M_0) \mathbf{k}}{T_1} \quad (2.19)$$

where \mathbf{i} , \mathbf{j} , \mathbf{k} are unit vectors in x , y , z directions, respectively. \mathbf{B} is the combined magnetic field vector consists of all the three types of magnetic field: the static field B_0 , the RF pulse B_1 , and the gradients.

The Bloch equation can be used in any condition. The first term on right hand side describes the free precession without considering T_1 and T_2 effects. The second term is the T_2 effect and the third term is the T_1 effect on the magnetization vectors.

Rewriting the Bloch equation in the rotating frame and ignoring the relaxation effects, we get:

$$\frac{\partial \mathbf{M}_{rot}}{\partial t} = \gamma \mathbf{M}_{rot} \times \mathbf{B}_{eff} \quad (2.20)$$

where

$$\frac{\partial \mathbf{M}_{rot}}{\partial t} = \frac{dM_{x'}}{dt} \mathbf{i} + \frac{dM_{y'}}{dt} \mathbf{j} + \frac{dM_{z'}}{dt} \mathbf{k}, \text{ and } \mathbf{B}_{eff} = \mathbf{B}_{rot} + \frac{\boldsymbol{\omega}}{\gamma} \quad (2.21)$$

\mathbf{B}_{eff} is the effective magnetic field that the bulk magnetization experiences in the rotating frame.

Following the same analysis, the general Bloch equation can be expressed in the rotating frame as:

$$\frac{\partial \mathbf{M}_{rot}}{\partial t} = \gamma \mathbf{M}_{rot} \times \mathbf{B}_{eff} - \frac{M_x \mathbf{i} + M_y \mathbf{j}}{T_2} - \frac{(M_{z'} - M_0) \mathbf{k}'}{T_1} \quad (2.22)$$

2.3 EXCITATION

In presence of only the main magnetic field B_0 , the magnetization M will align to the same direction as B_0 . There is no transverse magnetization in this equilibrium state because the phases of individual magnetic moments in this bulk magnetization are random and cancel with each other. The excitation process is the way to establish the phase coherence of these magnetic moments so that a transverse magnetization is generated. In order to achieve the phase coherence, an external force must be applied to the spin system. This external force is provided by an oscillating B_1 field which is perpendicular to the main magnetic field. In general, this B_1 field is rotating at the same angular frequency as the Larmor frequency to facilitate energy exchange.

2.3.1 Basic Excitation Principles

A typical RF pulse can be described by an amplitude modulated sinusoidal function:

$$\mathbf{B}_1(t) = 2\mathbf{B}_{1e}(t) \cos(\omega_{rf}t) \quad (2.23)$$

where $\mathbf{B}_{1e}(t)$ is an envelope function that modulates the amplitude, and ω_{rf} is the carrier frequency of the RF pulse. Using complex notation, the $\mathbf{B}_1(t)$ field can be rewritten as:

$$\mathbf{B}_1(t) = \mathbf{B}_{1e}(t)e^{i\omega_{rf}t} + \mathbf{B}_{1e}(t)e^{-i\omega_{rf}t} \quad (2.24)$$

We can see there are two rotating fields. The one rotating clockwise is called $\mathbf{B}_1^+(t)$, and the other rotating counterclockwise is called $\mathbf{B}_1^-(t)$. Because the counterclockwise component has a negligible effect on the magnetized spin system compared to the clockwise component (25,26), the effective $\mathbf{B}_1(t)$ field becomes

$$\mathbf{B}_1(t) = \mathbf{B}_{1e}(t)e^{-i\omega_{rf}t} \quad (2.25)$$

or in the matrix form:

$$\mathbf{B}_1 = \begin{bmatrix} B_{1,x} \\ B_{1,y} \end{bmatrix} = \begin{bmatrix} B_{1e} \cos \omega_{rf}t \\ -B_{1e} \sin \omega_{rf}t \end{bmatrix} \quad (2.26)$$

The property of an RF pulse is uniquely determined by the envelope function $\mathbf{B}_{1e}(t)$, which we will see more clearly in Chapter 4 that discusses pulse design.

2.3.2 On-Resonance Excitation

When the carrier frequency of an RF pulse is set to the Larmor frequency, a phase coherence of spins is established and the transverse magnetization will emerge (24). We call the excitation

induced by this pulse an on-resonance excitation. At this condition, the B_1 field will always align along the x' axis. Mathematically, we will have

$$\mathbf{B}_{1,\text{rot}} = \begin{bmatrix} B_{1,x'} \\ B_{1,y'} \end{bmatrix} = \mathbf{R}_{2D} \mathbf{B}_1 = \begin{bmatrix} \cos \omega_{rf} t & -\sin \omega_{rf} t \\ \sin \omega_{rf} t & \cos \omega_{rf} t \end{bmatrix} \begin{bmatrix} B_{1e} \cos \omega_{rf} t \\ -B_{1e} \sin \omega_{rf} t \end{bmatrix} = \begin{bmatrix} B_{1e} \\ 0 \end{bmatrix} = [B_{1e} \mathbf{i}'] \quad (2.27)$$

Then the effective magnetic field \mathbf{B}_{eff} will become

$$\mathbf{B}_{\text{eff}} = \left(B_0 - \frac{\omega_{rf}}{\gamma} \right) \mathbf{k}' + B_{1e} \mathbf{i}' \quad (2.28)$$

At the on-resonance excitation condition $\omega_{rf} = \omega_0 = \gamma B_0$, then

$$\mathbf{B}_{\text{eff}} = B_{1e} \mathbf{i}' \quad (2.29)$$

The effect of the main magnetic field B_0 is offset by the carrier frequency of the RF pulse. The only observed magnetic field in the rotating frame is B_{1e} applied along the x' axis. Then, the magnetization M will be tipped away from the z' axis, and tries to align itself to the y' axis. This is why a much smaller B_1 field can flip the magnetization away from the direction of the much stronger main magnetic field. The angular frequency of this rotation resulted by the RF pulse will be:

$$\omega_1 = \gamma B_{1e} \quad (2.30)$$

and the flip angle is the time integral of the angular frequency over the pulse duration T :

$$\alpha = \int_0^T \omega_1(\tau) d\tau = \gamma \int_0^T B_{1e}(\tau) d\tau \quad (2.31)$$

For a rectangular RF pulse,

$$\alpha = \omega_1 T = \gamma B_{1e} T \quad (2.32)$$

Then, ignoring the relaxing effects, we will have:

$$\frac{dM_{x'y'}}{dt} = \gamma B_{1e}(t) M_{x'y'} \quad (2.33)$$

The solution of this equation will be:

$$\begin{bmatrix} M_{x'} \\ M_{y'} \\ M_{z'} \end{bmatrix} = \begin{bmatrix} 0 \\ M_z^0 \sin(\alpha) \\ M_z^0 \cos(\alpha) \end{bmatrix} \quad (2.34)$$

where α is the flip angle defined in Equation (2.31).

2.3.3 Off-Resonance Excitation

The on-resonance excitation assumes that there is a constant Larmor frequency or uniform B_0 field so that the RF pulse can be tuned to the same frequency. In the real environment, however, the B_0 field is not perfectly uniform within the whole volume due to hardware imperfections, chemical shifts, or even the effects of the RF pulse. The B_0 field will be a space variant function. The difference of the local B_0 field with respect to the assumed Larmor frequency, which the RF pulse is tuned to, is called the off-resonance:

$$\Delta\omega(r) \equiv \omega(r) - \omega_0 \quad (2.35)$$

In presence of the off-resonance, the effective magnetic field \mathbf{B}_{eff} will have an additional term along the z axis,

$$\mathbf{B}_{eff} = \left(\frac{\omega(r)}{\gamma} - \frac{\omega_{rf}}{\gamma} \right) \mathbf{k}' + B_1 \mathbf{i}' = \frac{\Delta\omega}{\gamma} \mathbf{k}' + B_1 \mathbf{i}' \quad (2.36)$$

The Bloch equation in the rotating frame, ignoring relaxation effects is then

$$\frac{\partial M_{rot}}{\partial t} = \begin{bmatrix} 0 & \Delta\omega & 0 \\ -\Delta\omega & 0 & \omega_1(t) \\ 0 & -\omega_1(t) & 0 \end{bmatrix} \begin{bmatrix} M_{x'} \\ M_{y'} \\ M_{z'} \end{bmatrix} \quad (2.37)$$

In general, there is no close-form solution for this equation. For a constant RF field, we have the solution:

$$\begin{bmatrix} M_{x'} \\ M_{y'} \\ M_{z'} \end{bmatrix} = \begin{bmatrix} M_z^0 \sin \theta \cos \theta [1 - \cos(\alpha)] \\ M_z^0 \sin \theta \sin(\alpha) \\ M_z^0 [\cos^2 \theta + \sin^2 \theta \cos(\alpha)] \end{bmatrix} \quad (2.38)$$

where

$$\alpha = \omega_{eff} T = \sqrt{\Delta\omega^2 + \omega_1^2} T, \text{ and } \theta = \arctan\left(\frac{\omega_1}{\Delta\omega}\right)$$

Here α is the flip angle about the axis of the effective magnetic field B_{1eff} , so the magnetization after the excitation is not along the y' axis as the on-resonance case. This produces a phase shift. This dephasing effect caused by the off-resonance is characterized by the T_2' in Equation (2.10).

2.4 SIGNAL RECEPTION

After excitation, the magnetization will precess at the Larmor frequency, which can be detected with a coil. This is the basis of the NMR phenomenon. In this section, we will discuss the principles of signal reception.

2.4.1 Faraday's Law and the Reciprocity Law

Faraday's law states that a time-varying magnetic field will induce a voltage in a coil placed perpendicular to the direction of this magnetic field. Mathematically, it is represented by:

$$V = -\frac{\partial\Phi(t)}{dt} \quad (2.39)$$

where Φ is the magnetic flux. To determine this flux in MRI experiments, we make use of the principle of reciprocity. Specifically, if a unit current flows in the coil, it will produce a magnetic field $\mathbf{B}^{receive}(\mathbf{r})$ at location \mathbf{r} . Thus, the magnetic flux through the coil by $\mathbf{M}(\mathbf{r},t)$ is given by:

$$\Phi(t) = \int \mathbf{B}^{receive}(\mathbf{r}) \cdot \mathbf{M}(\mathbf{r}, t) d\mathbf{r} \quad (2.40)$$

Substituting this into Equation (2.39), we have

$$V = -\frac{\partial}{\partial t} \int \mathbf{B}^{receive}(\mathbf{r}) \cdot \mathbf{M}(\mathbf{r}, t) d\mathbf{r} \quad (2.41)$$

Since the z component of the magnetization \mathbf{M} is parallel to the plane of the coil, the M_z component can be ignored. That is why many people often refer the MR signal as the transverse magnetization M_{xy} . The real MR signal we record is usually the voltage generated after the demodulation of the high frequency term, which corresponds to the signal in the rotating frame.

(25)

$$S(t) \propto \omega_0 \int \mathbf{B}_{xy}^{receive*}(\mathbf{r}) \mathbf{M}_{xy}(\mathbf{r}, 0) e^{-t/T_2(\mathbf{r})} e^{-i\Delta\omega(\mathbf{r})t} d\mathbf{r} \quad (2.42)$$

where $\mathbf{B}_{xy}^{receive*}$ is the complex conjugate of the transverse receive magnetic field $\mathbf{B}_{xy}^{receive}$, or the “coil sensitivity.” As such, we can define $\mathbf{C} \equiv \mathbf{B}_{xy}^{receive*}$ to represent the receive coil sensitivity.

The dependence of signal on the “transmit coil sensitivity” is implicitly included in the magnetization \mathbf{M} . We will discuss the receiver and transmitter coil sensitivities in subsequent chapters, as they are central to the ideas of parallel imaging.

Ignoring the T_2^* effect, we can see the signal amplitude is proportional to the Larmor frequency, the coil sensitivity, the transverse magnetization, and the sample volume.

$$|S| \propto \omega_0 M_{xy} C V_s \quad (2.43)$$

The Larmor frequency is linearly related to the main magnetic field B_0 , as is the transverse magnetization. This is why the high field MRI has the advantage on the image SNR.

2.4.2 Free Induction Decay (FID)

The simplest NMR experiment is to detect a global signal from the sample. The signal is collected right after an RF pulse is applied. No gradient fields are involved here. The signal is called the Free Induction Decay (FID). The signal equation derived in last section can be applied directly to FID experiments.

The FID experiments are usually used to optimize MRI systems (25). They are routinely used in the pre-scan steps in pulse sequences to locate the resonance peak and determine the transmit and receive gains. It can be also used to measure the field inhomogeneity, or determine the abundance of different chemical compounds in a sample, which is often referred as MR Spectroscopy (MRS) or chemical shift imaging.

2.4.3 Frequency Encoding

Spatial information can be encoded during the free decay period by adding gradient magnetic fields on top of the main magnetic field. The first proposed encoding method is frequency encoding, which was used in the first MRI experiment by Lauterbur *et al.* in 1972 (22). Adding a gradient field along an arbitrary line \mathbf{r} in the space will establish a linear relationship between the spatial information along \mathbf{r} and the frequencies of MR signal. In this case, the Larmor frequency at position \mathbf{r} is:

$$\omega(\mathbf{r}) = \omega_0 + \gamma G_{FE} \mathbf{r} \quad (2.44)$$

Ignoring the T_2^* and coil sensitivity effects, the 1D image signal acquired with the frequency encoding will be:

$$S(t) \propto \int_{-\infty}^{\infty} M(r) e^{-i\gamma(B_0 + G_{FE}r)t} dr = \int_{-\infty}^{\infty} M(r) e^{-i(\omega_0 + \gamma G_{FE}r)t} dr \quad (2.45)$$

Removing the center frequency ω_0 , we have

$$S(t) \propto \int_{-\infty}^{\infty} M(r) e^{-i\gamma G_{FE}rt} dr \quad (2.46)$$

The direction of the frequency-encoding gradient is always along the main magnetic field direction. At a given time, only one direction can be frequency encoded. To generate a multi-dimensional image, we need either repeat the frequency encoding along other directions or use other encoding methods such as the phase encoding method we will discuss in the following.

2.4.4 Phase Encoding

As the name suggests, the phase encoding method encodes the spatial location with different initial phases. To prepare the incrementally changed phase, a gradient field along a line \mathbf{r} is turned on for a short period of time, and then turned off. The demodulated signal after this period time T_{PE} will be:

$$S(t) \propto \int_{-\infty}^{\infty} M(r) e^{-i\gamma G_{PE}rT_{PE}} dr \quad (2.47)$$

The phase term in this equation is

$$\phi(r) = -\gamma G_{PE}rT_{PE} \quad (2.48)$$

Combining the frequency and phase encoding methods, we can conveniently encode a 2D or 3D space in an arbitrary coordinate.

3.0 IMAGE RECONSTRUCTION AND PARALLEL IMAGING

3.1 INTRODUCTON

In the previous chapter, we discussed the fundamental principles of the NMR phenomenon and the basis of signal detection. In this chapter, we will discuss the way to generate images from the raw signal. On the scanner, a separate image reconstruction server does this step. We will focus our discussion on the currently evolving parallel imaging technique (27,28). The coil sensitivity information of multiple coil elements on a phased array coil will be exploited to encode some of the spatial information so that we can use a less number of gradient frequency and phase encodings. The advantage of this technique is reduced scan time and/or increased resolution.

3.2 *k*-SPACE

The signal equation for a 2D MR experiment with frequency and phase encoding suggests a Fourier relationship between the raw signal and the MR image.

$$S(t) = \int_{-\infty}^{\infty} M(\mathbf{r}) e^{-iy \int_0^t \mathbf{G}_r(s) \cdot \mathbf{r} ds} d\mathbf{r} \quad (3.1)$$

If we define a *k*-space as:

$$\mathbf{k}_r(t) = \frac{\gamma}{2\pi} \int_0^t \mathbf{G}_r(s) ds \quad (3.2)$$

Then, the signal $S(k_r)$ is a Fourier transform of the magnetization.

$$S(\mathbf{k}_r) = \int_{-\infty}^{\infty} M(\mathbf{r}) e^{-i2\pi\mathbf{k}_r \cdot \mathbf{r}} d\mathbf{r} \quad (3.3)$$

The k -space is also called the spatial frequency space. It is the conjugate of the image space. The raw data is written onto the grid of k -space determined by Equation (3.3). Taking the Fourier transform to this k -space generates MR images.

3.2.1 Cartesian Grid

The Cartesian trajectory in k -space is defined by applying a frequency-encoding gradient in one axis and a phase encoding gradient in the other axis. In Figure 3.1, we show a FLASH (“Fast Low Angle Shot” gradient echo) sequence plot. After a slice selective pulse (the details of slice-selection will be presented later), a phase encoding gradient along the y -axis is applied. Together with a fixed amplitude dephasing gradient along the x -axis, these gradients move the trajectory from the origin (time point a) to the starting point (time point b) of the acquisition in k -space. Then the frequency-encoding gradient along the x -axis is turned on to acquire data along the horizontal lines (time point b to c) in the k -space. Rephasing gradients along the x and y -axes are used to move the trajectory back to the origin. The sequence is repeated multiple times with phase encoding gradients of different amplitudes so that multiple horizontal lines (i.e. b' to c') can be acquired. The Fast Fourier transform (FFT) algorithm can be applied directly on the data acquired on the rectangular grid to generate the MR images.

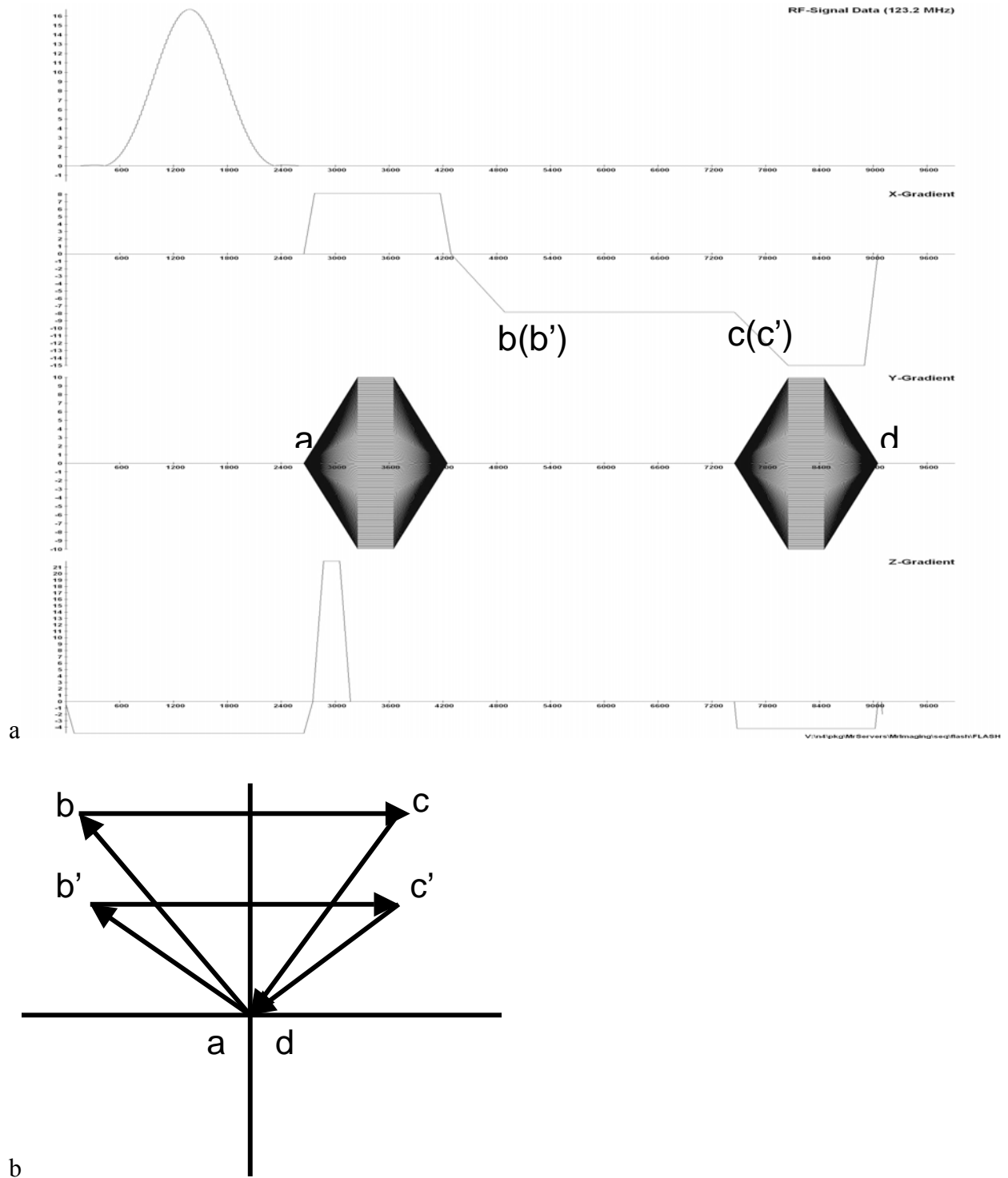


Figure 3.1: (a) A FLASH (gradient echo) sequence. The frequency encoding gradient is applied along the x-axis, and the phase encoding gradient is applied along the y-axis. (b) The Cartesian k -space defined by the FLASH sequence in (a). Corresponding time points are plotted in both figures to illustrate how k -space is filled by the gradients.

3.2.2 Non-Cartesian Sampling

Although Cartesian sampling schemes are widely used because of the convenience of the FFT reconstruction, non-Cartesian trajectories have advantages in sampling time efficiency. As we can see from the FLASH sequence, the regular Cartesian sampling using the phase encoding method can only acquire one horizontal line in k -space each TR. To fill the whole k -space, the sequence needs to repeat N_{PE} times. One option is to use single shot Cartesian trajectories such as Echo Planar Imaging (EPI) to remedy this. Non-Cartesian single-shot trajectories can also be used to acquire a greater portion of k -space per TR. A common non-Cartesian trajectory is the spiral trajectory. A single-shot spiral trajectory can cover the full k -space with one TR. Multi-shot spirals are also used in high-resolution images to make the readout less sensitive to off-resonance artifacts. In Figure 3.2 we show one of the 24 arms of a multi-shot spiral trajectory in (a) and the gradients that generate this trajectory in (b). The time map and the sampling density function are also shown in Figure 3.2 (c) and (d). Notice that k -space is not uniformly sampled by the spiral trajectory. During reconstruction, this non-uniform sampling needs to be compensated.

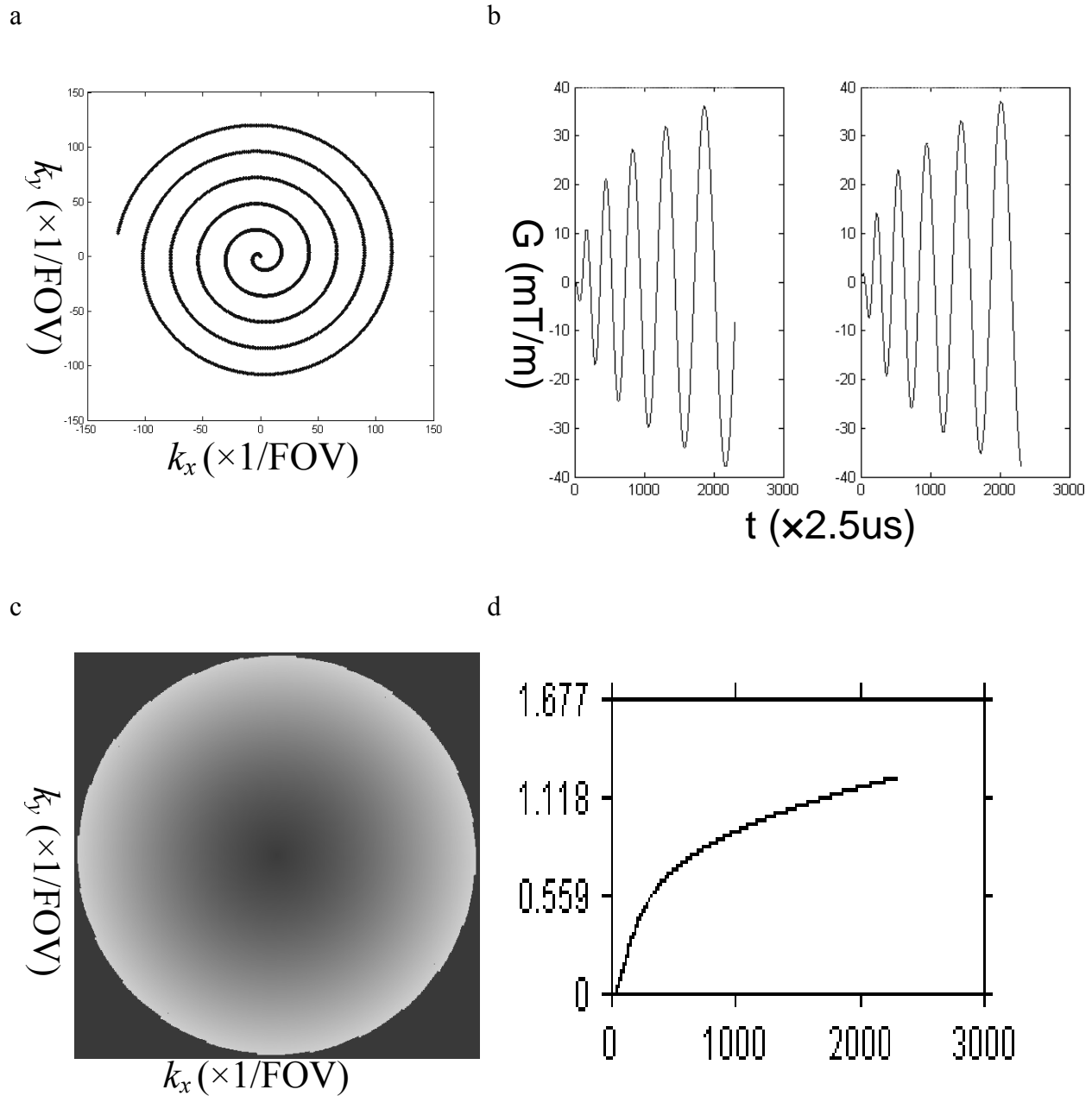


Figure 3.2: (a) One of the 24 arms of the interleaved spiral trajectory in k -space. (b) The corresponding gradients along the x and y axis for one arm. (c) The time map in k -space. The gray scale in this time map corresponds to the readout time from 0 (k -space center) to 5.8 ms (k -space edges) (d) The sampling density in k -space. The k -space is not uniformly sampled by the spiral trajectory. During reconstruction, this non-uniform sampling needs to be compensated.

3.3 SAMPLING REQUIREMENTS

To get the desired image, k -space has to be sampled correctly. Critical parameters that control the sampling scheme include: the image resolution (Δx), the field of view (FOV), the sampling interval (Δk), and k -space extent (k_{max}).

3.3.1 Nyquist Criteria

Without losing generality, we will discuss the sampling requirement for one-dimensional uniformly sampled data. The concept can be extended to higher dimensional data easily by treating each dimension separately. Discrete sampling in k -space is equivalent to the multiplication of the MR signal by a comb function (24):

$$\hat{S}(k) = \Delta k \sum_{m=-\infty}^{\infty} S(m\Delta k) \delta(k - m\Delta k) \quad (3.4)$$

The reconstructed image can be obtained by inverse Fourier transformation:

$$\hat{I}(r) = IFT(\hat{S}(k)) = IFT(S(k)) * IFT(\Delta k \sum_{m=-\infty}^{\infty} \delta(k - m\Delta k)) = \sum_{n=-\infty}^{\infty} I(r - n / \Delta k) \quad (3.5)$$

where the signal $S(k)$ and image $I(r)$ are the Fourier conjugates. To recover an unaliased copy for the reconstructed image $\hat{I}(r)$, we need to have:

$$\frac{1}{\Delta k} \geq A \quad (3.6)$$

where A is the size of the object being imaged. We define the field of view (FOV) of an image as:

$$FOV \equiv 1 / \Delta k \quad (3.7)$$

Then we have

$$FOV \geq A \text{ or } \Delta k \leq \frac{1}{A} \quad (3.8)$$

This is referred to as the Nyquist criteria (24,29).

3.3.2 Aliasing

When the Nyquist criteria are not met, the image will wrap around on itself. This artifact is called aliasing. In Figure 3.3 we show the relationship between the sampling interval and aliasing artifact. Assuming the k -space is sampled by the trajectory in (a) and generates the image in (b), sparser k -space coverage with double interval along the y -axis will cause a 1/2 FOV aliasing artifact along the y -axis in the image (d). Specifically, the upper half of the image is overlapped on top of the lower half of the image, and the lower half of image is overlapped on the top half of the image.

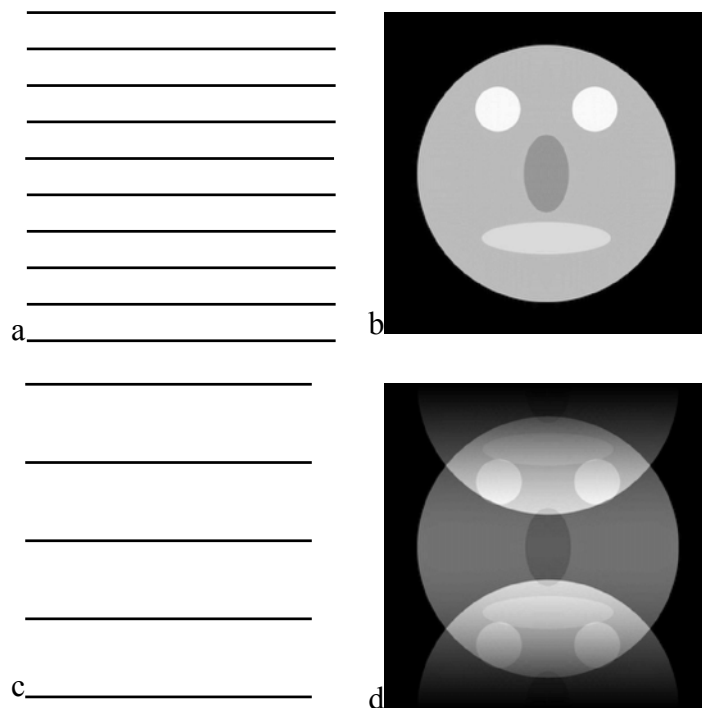


Figure 3.3: The interpretation how aliasing artifact generated with numerical simulation. (b) and (d) show the reconstructed phantom images using the sampling schemes represented in (a) and (c) respectively.

3.3.3 Variable Density Sampling

The k -space has strong signals around the origin due to most of the image being comprised of low spatial frequencies. Signals approach the noise level when sampling is at the edge of k -space. If we look at the example shown in Figure 3.4, we can see that the center of k -space defines most of the image, and adding outside lines in the k -space only adds details to it. This gives us a hint that we might be able to sample the center k -space uniformly but the edges of k -space sparser. In Figure 3.5 (b), we show a variable density spiral trajectory that accomplished this goal. Compared to the uniform spiral (a), it has the same density as that of (a) at the center k -space. However, the edges of k -space are sampled much sparser. This sampling scheme can

reduce the scan time at the expense of little bit high frequency aliasing due to the undersampling at the edges of k -space.

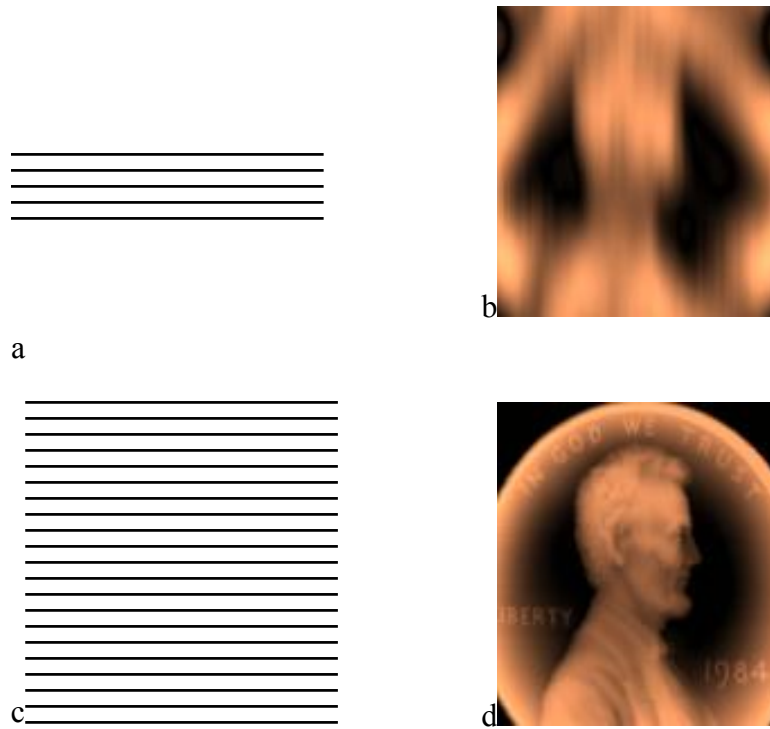


Figure 3.4: The high frequency components of k -space define the details of the image. Image in (d) is much sharper than image in (b), because more lines are acquired at the edge k -space in (c) than in (a).

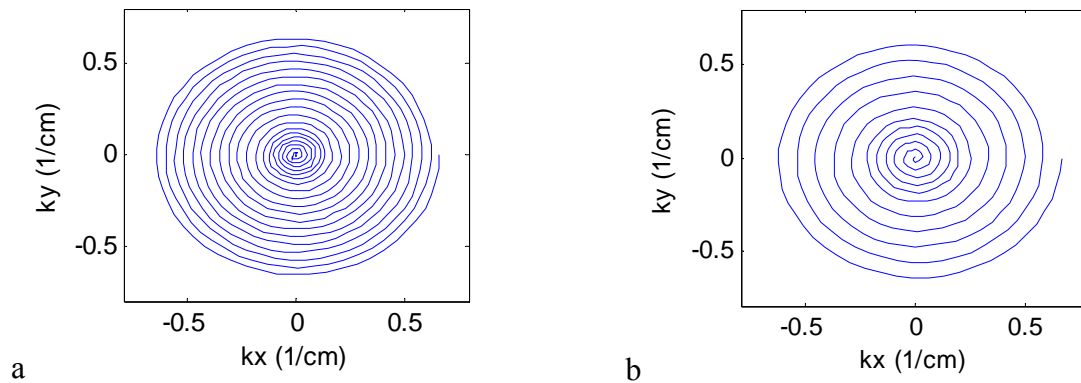


Figure 3.5: Comparison of the (a) uniform spiral and (b) variable density spiral trajectory. Reducing sampling density at k -space edges dramatically reduce the sampling points, which is at the expense of a little bit blurring of the reconstructed image.

3.4 PARALLEL IMAGING

Multiple-channel phased array coils were originally introduced to increase SNR. Recently, people found that a carefully designed phased array coil can also be used for reduced data requirements with parallel imaging techniques (27,28,30-33). The idea is that the inherent spatial sensitivity of the receiver coils can be used to generate missing data in an undersampled k -space acquisition with a penalty in increased artifact and decreased SNR. As we discussed in last section, an undersampled k -space acquisition will have wrap-around aliasing. By using the coil sensitivities, parallel imaging techniques are able to remove the aliasing artifact.

Sodickson *et al.* proposed a simultaneous acquisition of spatial harmonics (SMASH) technique (28) which uses the coil sensitivities to fit to the higher order spatial harmonics so that the missing phase encoding lines in the k -space can be recovered, and an unaliasing image is able to be generated from the full k -space. The original SMASH technique has evolved into several other methods like generalized SMASH (31), AUTO-SMASH (32) and GRAPPA (33). All these methods are used to recover the missing lines in k -space with different fitting schemes. The GRAPPA technique is the most widely used SMASH-like method. In Figure 3.6, we show a phantom data with a Cartesian gradient echo sequence on a 1.5T GE Signa scanner with GRAPPA reconstruction.

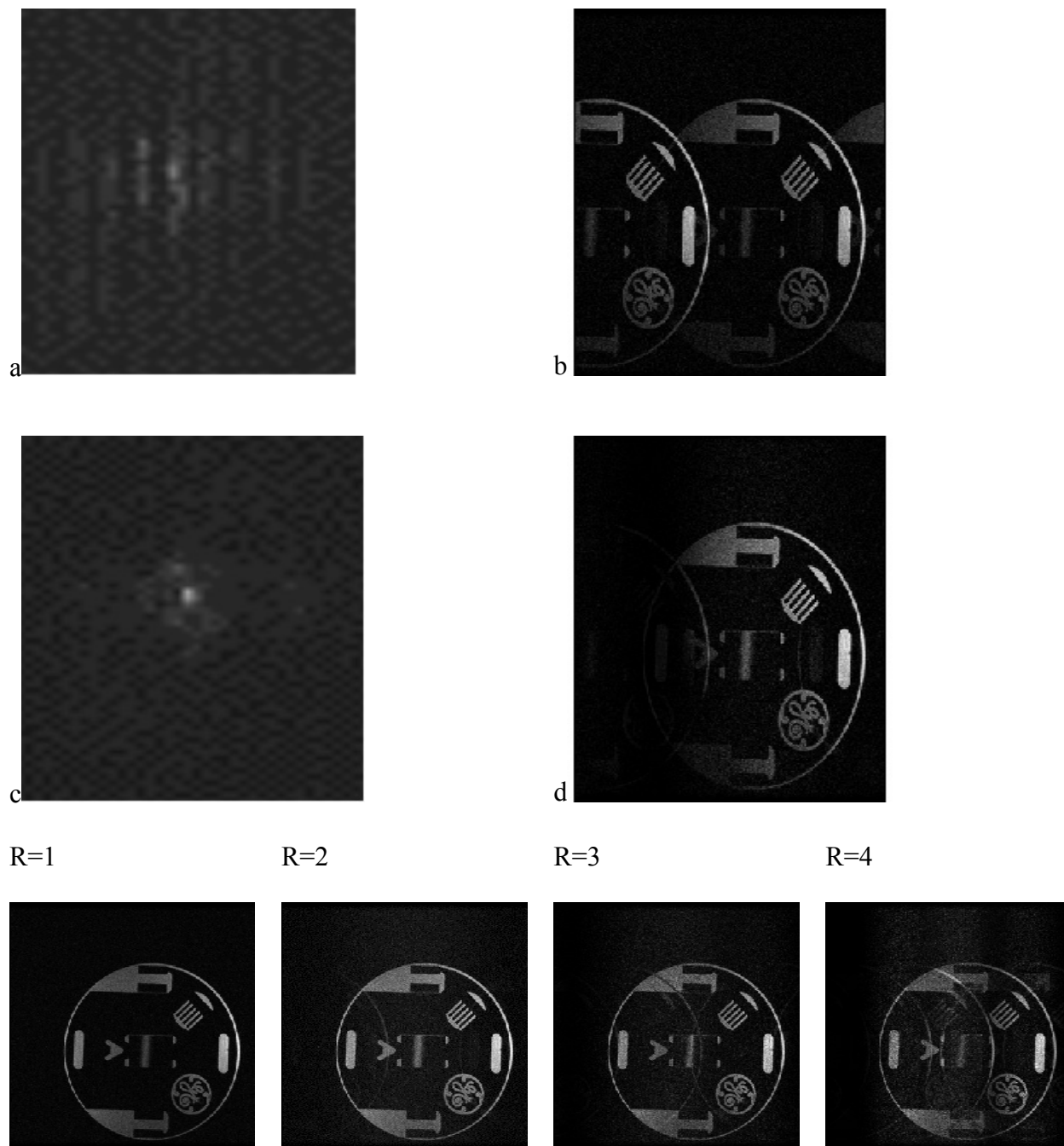


Figure 3.6: The GRAPPA reconstruction phantom data using 4-channel GE Cardiac coil. The 2 fold undersampled k -space (a) and its Fourier transform (b) are shown in the first row. The GRAPPA recovered k -space (c) and its Fourier transform (d) are shown in the second row. The third row shows the GRAPPA reconstructed images with k -space reductions from 1 to 4. We can see the SNR becomes lower and the residue aliasing becomes larger as the reduction factor becomes bigger.

In 1999 Pruessmann *et al.* proposed another parallel imaging technique called sensitivity encoding (SENSE) (27). The SENSE method is one of the most widely used approaches because it provides a generalized signal equation description, and has no limit on coil configurations and k -space trajectories. Assuming a uniform transmission, the signal from receiver i can be written:

$$S_i(t) = \int C_i(\mathbf{r})M(\mathbf{r})e^{-i2\pi\mathbf{k}(t)\cdot\mathbf{r}} d\mathbf{r} \quad (3.9)$$

Rewriting as a matrix equation and including an error term ε ,

$$\mathbf{s} = \mathbf{A}\mathbf{m} + \varepsilon, \text{ with } a_{mn} = C_m e^{-i2\pi\mathbf{k}(t_m)\cdot\mathbf{r}_n} \quad (3.10)$$

This equation is no longer a simple Fourier transform relationship. Conjugate gradient iterative methods have been applied to solve a least squares minimization problem with the addition of regularization term $\Phi(m)$ to penalize the roughness of the estimate:

$$\hat{m} = \arg \min_m \|s - \mathbf{A}m\| + \Phi(m) \quad (3.11)$$

By including the sensitivity information, the sampling density of k -space can be reduced. This “reduction factor” R is often defined by the ratio of the original sampling density to the undersampled density. The advantages of SENSE imaging have been explored in cardiac imaging and fMRI. The decreased readouts allowed by SENSE have been shown to increase temporal resolution and reduce susceptibility artifacts. The penalty of this acceleration in readout is decreased image SNR and incomplete alias cancellation, which is a result of the ill-posed inversion of the matrix \mathbf{m} due to imperfect coil configuration or imaging plane for example. Self-calibrating parallel imaging has also been demonstrated with variable density Cartesian sampling schemes (32-34) or multi-shot uniform spiral sampling (35,36), where the central k -space regions can be used to generate coil sensitivity maps in real-time (63,64). This approach reduces the misregistration between the coil calibration scan and the data acquisition.

3.4.1 Coil Sensitivity

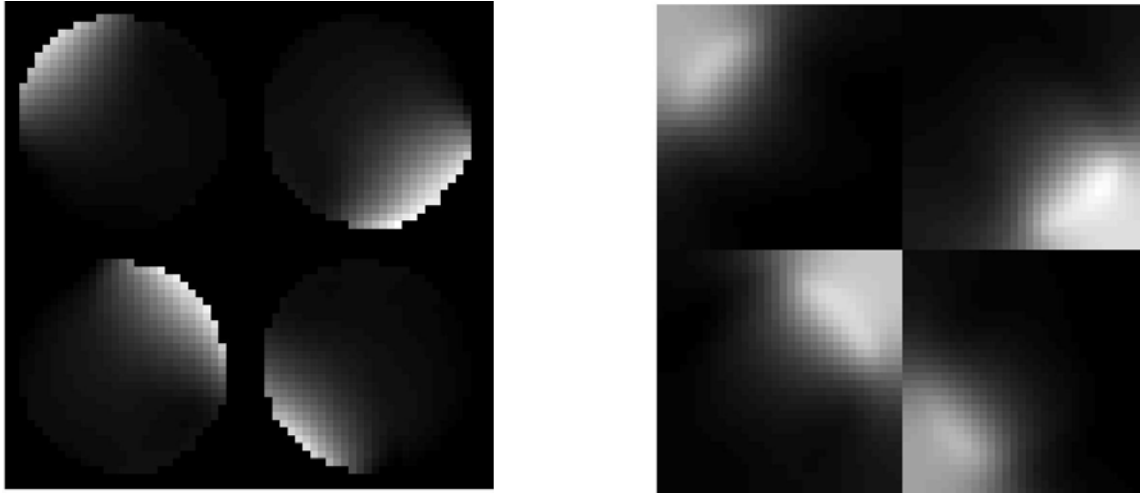


Figure 3.7: The sensitivity maps of a commercial 3T phased array coil estimated with (a) the conventional smoothed array/body ratio method; (b) the iterative fitting method

It is crucial to obtain an accurate estimate of the coil sensitivity for parallel imaging. In parallel imaging applications the coil sensitivities must be known and one typically uses the smoothed ratio between the images from each receiver and the body coil obtained in a pre-scan. The problem of this approach is the discontinuity at the edge of the sensitivity maps. When applied to an image object equal or larger than the support region of the sensitivity maps, this discontinuity will cause ill conditioning in the inverting matrix. One way to circumvent this problem is to use an iterative fitting method proposed by Fessler *et al.* (37). Instead of directly taking the ratio of the array images over body coil image, this method forms a statistical model such that array images are the product of the body images and the sensitivity contaminated by noise.

$$I(r) = C(r)M(r) + \varepsilon \quad (3.12)$$

Where $I(r)$ is the array images, $M(r)$ is the body coil image and ε is the noise. Since the noise is mainly white Gaussian noise in MRI, the penalized least squares cost function is chosen as:

$$\Psi(\mathbf{C}) = \frac{1}{2} \|I - \mathbf{C}M\|_w^2 + \beta\Phi(\mathbf{C}), \text{ so that } \hat{\mathbf{C}} = \arg \min_{\mathbf{C}} \Psi(\mathbf{C}) \quad (3.13)$$

where W is a weighting function, and $\Phi(\mathbf{C})$ is a quadratic regularization function. The sensitivity maps $C(r)$ can be obtained by iteratively solving the inverse problem using the Conjugate-gradient method. The main advantage of this method is the sensitivity maps obtained are extended to the whole FOV (see Fig.3.7 (b)).

Another important sensitivity estimation method is the self-calibrating method, which samples the k -space with variable density. The edges of the k -space are down-sampled with the reduction factor R as the regular parallel imaging experiments. The center k -space is fully sampled or over-sampled. The sensitivities are extracted from this small center region assuming the sensitivities are smooth and contain only low frequency information. An example of the self-calibration method is demonstrated in Reference (35). Exploiting the intrinsic over-sampling property at the center of the spiral trajectory, the normalized coil sensitivity maps are estimated from a fully sampled low-resolution reference scan:

$$C_l(r) = \frac{L_l(r)}{\sqrt{\sum_l |L_l(r)|^2}} \quad (3.14)$$

For the proposed self-calibration, these reference scans are replaced with the k -space center data in the accelerated acquisition itself. For accurate coil sensitivity estimation, the spatial resolution must be sufficiently high to contain all of the major spatial frequencies in the coil sensitivity. However, at such spatial resolution there are substantial under-sampling artifacts. The size of the k -space center is selected by balancing between the spatial details for coil sensitivity.

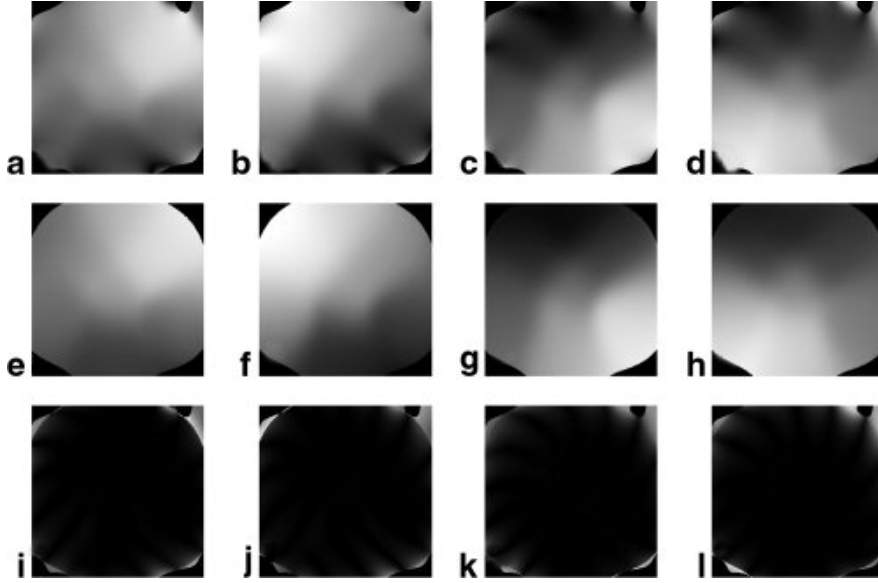


Figure.3.8: a-d: (top) Normalized low-resolution images obtained from the $2\times$ undersampled data in a k-space center of radius $4/\text{FOV}$, acquired with a four-element coil array. e-h: (middle) Corresponding normalized low-resolution images from fully sampled data. i-l: (bottom) The difference between the top and middle images, with an average error of 4%. All images are displayed with the same window/level. The slight difference indicates that the undersampling artifacts at k-space size of $4/\text{FOV}$ are marginal

3.4.2 SNR and g-Factor

SNR is an important indicator of image quality. In principle, image SNR is proportional to the volume of the voxel (V_s) and the square root of the total number of sampling points, and is inversely proportional to the square root of the bandwidth:

$$SNR \propto V_s \frac{\sqrt{N_x N_y N_z}}{\sqrt{BW}} \quad (3.15)$$

It is obvious that the parallel imaging saves scan time with the penalty in image SNR because the number of sampling points is reduced. For an image acquired with an R-fold undersampled

parallel imaging technique, the maximum achievable (SNR_R) will be $\frac{1}{\sqrt{R}}$ of the SNR of the fully sampled image (SNR_F):

$$SNR_R = \frac{SNR_F}{\sqrt{R}} \quad (3.16)$$

This equation is deduced with the assumption that the sensitivities of the coil elements are independent of each other. In reality, however, there is always some coupling among coil elements. The actual SNR in parallel imaging (SNR_p) is therefore less than the value calculated with Equation (3.16). The ratio between the theoretical optimal SNR_R and the actual SNR_p from the parallel imaging experiment is defined as the g-factor.

$$g(r) = \frac{SNR_R}{SNR_p} = \frac{SNR_F / \sqrt{R}}{SNR_p} \quad (3.17)$$

This g-factor is an indicator of the parallel imaging efficiency. An optimal g-factor can be achieved with a well-designed coil and carefully selected image plane.

4.0 RF PULSE DESIGN

4.1 INTRODUCTION

RF pulses prepare the magnetization for imaging. The most often used RF pulse is the slice-selective SINC pulse, where it excites spins within a slice. The received MR signal will only come from this slice. This RF pulse is basically a simple 1D spatial-selective pulse. More complex pulses like multi-dimensional spatial-selective pulses or spectral-spatial pulses can also be applied in MR experiments. The behavior of RF pulses can be explained by the Bloch equation as we have seen in previous chapters. However, there is no closed form solution for the Bloch equation for the B_1 field given the desired magnetization pattern and gradients waveforms, which makes it difficult to be used as a convenient tool for RF pulse design. In this chapter we will discuss the analysis and design of the major types of RF pulses in multi-dimensions for spatial and spectral selective excitations (17, 38-44).

4.2 THE SMALL-TIP ANGLE APPROXIMATION

4.2.1 Fourier Relationship

Let's start with the Bloch equation

$$\frac{d}{dt} \begin{pmatrix} M_x \\ M_y \\ M_z \end{pmatrix} = \begin{pmatrix} -1/T_2 & \gamma \mathbf{G} \cdot \mathbf{r} & -\gamma B_{1,y} \\ -\gamma \mathbf{G} \cdot \mathbf{r} & -1/T_2 & \gamma B_{1,x} \\ \gamma B_{1,y} & -\gamma B_{1,x} & -1/T_1 \end{pmatrix} \begin{pmatrix} M_x \\ M_y \\ M_z \end{pmatrix} + M_0 \begin{pmatrix} 0 \\ 0 \\ 1/T_1 \end{pmatrix} \quad (4.1)$$

Where the gradient vector $\mathbf{G} = (G_x \ G_y \ G_z)$, and position vector $\mathbf{r} = (x \ y \ z)$

Assuming that the excitation is fast compared to relaxation, we will ignore T_1, T_2 . i.e. $1/T_1$ and $1/T_2 \sim 0$

$$\frac{d}{dt} \begin{pmatrix} M_x \\ M_y \\ M_z \end{pmatrix} = \begin{pmatrix} 0 & \gamma \mathbf{G} \cdot \mathbf{r} & -\gamma B_{1,y} \\ -\gamma \mathbf{G} \cdot \mathbf{r} & 0 & \gamma B_{1,x} \\ \gamma B_{1,y} & -\gamma B_{1,x} & 0 \end{pmatrix} \begin{pmatrix} M_x \\ M_y \\ M_z \end{pmatrix} \quad (4.2)$$

In the small-tip-angle approximation (39), we assume tip angle θ is small so that $M_z \approx M_0$. Then

Equation (4.2) becomes

$$\begin{aligned} \frac{d}{dt} M_x &= 0 + \gamma \mathbf{G} \cdot \mathbf{r} M_y - \gamma B_{1,y} M_0 \\ \frac{d}{dt} M_y &= -\gamma \mathbf{G} \cdot \mathbf{r} M_x + 0 + \gamma B_{1,x} M_0 \end{aligned} \quad (4.3)$$

Define

$$\begin{aligned} M_{xy} &= M_x + iM_y \\ B_1 &= B_{1,x} + iB_{1,y} \end{aligned} \quad (4.4)$$

The two equations in (4.3) can be combined into one equation:

$$\frac{d}{dt} M_{xy}(\mathbf{r}, t) = -i\gamma \mathbf{G}(t) \cdot \mathbf{r} M_{xy}(\mathbf{r}) + iM_0 \gamma B_1(t) \quad (4.5)$$

This is a simple first order differential equation, and the solution will be:

$$M_{xy}(\mathbf{r}, T) = iM_0 \int_{-\infty}^T \gamma B_1(t) e^{-i \int_t^T \gamma \mathbf{G}(s) \cdot \mathbf{r} ds} dt \quad (4.6)$$

where T is the end time of the RF pulse. Equation (4.6) is the form of a Fourier transform. Exploiting this relationship between B_1 and M_{xy} , one can easily determine the RF waveform B_1 for a given transverse magnetization M_{xy} and gradients \mathbf{G} .

4.2.2 k -Space Interpretation

Let's define

$$k(t, T) = -\frac{\gamma}{2\pi} \int_t^T \mathbf{G}(s) ds \quad (4.7)$$

Then equation (4.6) will be:

$$M_{xy}(\mathbf{r}, T) = iM_0 \int_{-\infty}^T \gamma B_1(t) e^{i2\pi \mathbf{k}(t, T) \cdot \mathbf{r}} dt \quad (4.8)$$

Equation (4.7) is the definition of the excitation k -space. We should notice that the excitation k -space is defined differently from that of the readout k -space, where

$$k^r(t) = \frac{\gamma}{2\pi} \int_0^t \mathbf{G}(s) ds \quad (4.9)$$

The excitation k -space is the integral of remaining gradient, while the readout k -space is the integral of gradient from end of excitation to readout samples.

$$\begin{aligned} M_{xy}(\mathbf{r}, T) &= iM_0 \int_{-\infty}^T \gamma B_1(t) \int_{\mathbf{k}} \delta(\mathbf{k}(t, T) - \mathbf{k}) e^{i2\pi \mathbf{k} \cdot \mathbf{r}} d\mathbf{k} dt \\ &= iM_0 \int_{\mathbf{k}} \left[\int_{-\infty}^T \gamma B_1(t) \delta(\mathbf{k}(t, T) - \mathbf{k}) dt \right] e^{i2\pi \mathbf{k} \cdot \mathbf{r}} d\mathbf{k} \end{aligned} \quad (4.10)$$

Let's define the items within the bracket as $P(\mathbf{k})$

$$P(\mathbf{k}) = \left[\int_{-\infty}^T \gamma B_1(t) \delta(\mathbf{k}(t, T) - \mathbf{k}) dt \right] \quad (4.11)$$

Then $P(\mathbf{k})$ is the Fourier transform of the magnetization.

If the trajectory in k -space is derivable, i.e., there is no singular point, we can rewrite the equation (4.11) so that we have a unit delta function

$$P(\mathbf{k}) = \left[\int_{-\infty}^T \frac{\gamma B_1(t)}{|\mathbf{k}'(t)|} \delta(\mathbf{k}(t, T) - \mathbf{k}) |\mathbf{k}'(t, T)| dt \right] \quad (4.12)$$

Let

$$W(\mathbf{k}) = \frac{\gamma B_1(\tau)}{|\mathbf{k}'(\tau)|} \quad (4.13)$$

if we assume $W(\mathbf{k})$ is a constant,

$$P(\mathbf{k}) = W(\mathbf{k})S(\mathbf{k}) \quad (4.14)$$

where

$$S(\mathbf{k}) = \int_{-\infty}^T \delta(\mathbf{k}(t, T) - \mathbf{k}) |\mathbf{k}'(t, T)| dt \quad (4.15)$$

Then

$$M_{xy}(\mathbf{r}, T) = iM_0 \int_{\mathbf{k}} W(\mathbf{k})S(\mathbf{k})e^{i2\pi\mathbf{k}\cdot\mathbf{r}} d\mathbf{k} \quad (4.16)$$

In equation(4.16), $W(\mathbf{k})$ is the k -space weighting function, and $S(\mathbf{k})$ is the k -space sampling function.

Let's see a simple 1D slice selection example. In figure 4.1 we can see the RF waveform that is a SINC and Gradient G_z that is a trapezoid with a half area refocusing lobe. $\mathbf{k}(t)$ is calculated according to equation (4.7).

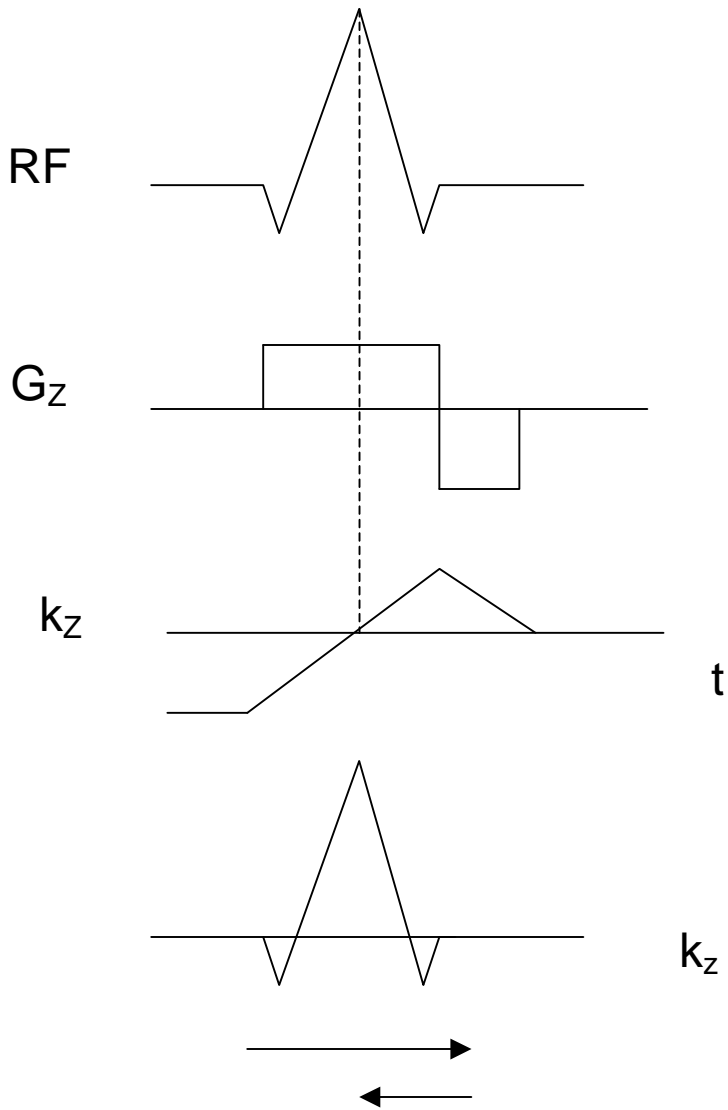


Figure 4.1: The k -space interpretation of RF pulse.(45)

The k -space is sampled from left to right during the positive G_z lobe, and weighted with the RF waveform. The half-area negative lobe of the gradient pushes the trajectory back to the center k -space while no RF weighting applied (45). This is a rephasing process.

4.3 TWO-DIMENSIONAL PULSE DESIGN

Under the small-tip-angle approximation regime, we can start our pulse design from the equation 3.16. First, we will need to pick a k -space trajectory. Spiral or EPI trajectories are the most common choices because they can cover a 2D k -space with a single shot. Then, we will prescribe an excitation profile $M(\mathbf{r})$ which is the Fourier transform of the product of $S(\mathbf{k})$ and $W(\mathbf{k})$. Since the sampling function $S(\mathbf{k})$ is a unit delta function, the weighting function $W(\mathbf{k})$ is a discretized version of the Fourier transform of the desired excitation profile. According to the equation (4.13), the desired B_1 waveform will be:

$$B_1(t) = \frac{|\mathbf{k}'(t)|}{\gamma} W(\mathbf{k}(t)) \quad (4.17)$$

The term $|\mathbf{k}'(t)|$ is an estimate of the sampling density function $d(t)$. If we have a better estimation of $d(t)$, we can replace the first term in equation (4.17) with $d(t)$ to achieve better accuracy(39).

4.3.1 Spiral Pulse

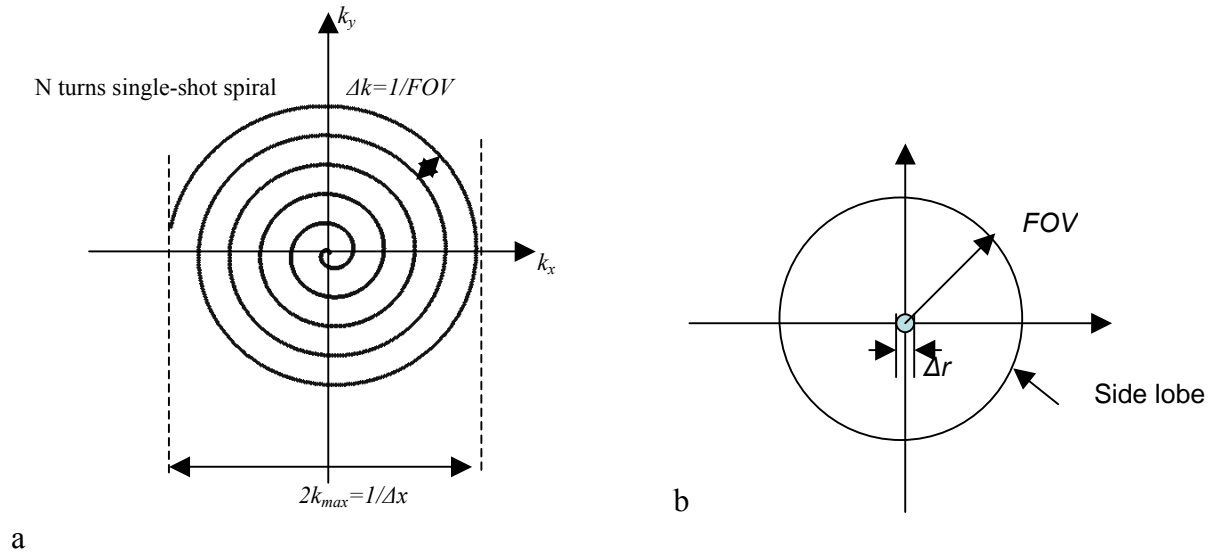


Figure 4.2: k -space trajectory design. (a) the single-shot spiral k -space. (b) the image space (45).

The pulse excitation resolution and excitation FOV are two important parameters to choose in the trajectory design. For a given pulse resolution Δr , the maximal k -space coverage is determined by:

$$k_{max} = \frac{1}{2\Delta r} \quad (4.18)$$

The excitation FOV will determine the resolution in k -space Δk , or the number of turns N of the spiral:

$$\Delta k = \frac{1}{FOV} \quad (4.19)$$

Noticing $\Delta k = 2k_{max}/(2N) = 1/(2N\Delta r)$, we have:

$$N = \frac{FOV}{2\Delta r} \quad (4.20)$$

Since $k = -\frac{\gamma}{2\pi} \int_t^T G(s)ds$, we have

$$\Delta k(t) = \frac{\gamma}{2\pi} G(t)\Delta t \quad (4.21)$$

where Δt is the scanner's gradient interval. To avoid aliasing, the maximal $G(t)$ allowed will be:

$$G_{\max} = \max\left(\frac{2\pi}{\gamma \cdot \Delta t \cdot FOV}, g_{\max}\right) \quad (4.22)$$

,where g_{\max} is the scanner's gradient limit. We always want to obtain a minimal length spiral for given hardware constrains. Thus, we should exploit maximal slew rate at the start of the spiral until the maximal gradient G_{\max} is achieved or the k_{\max} is reached. The remaining k -space will be covered by the spiral with constant gradient G_{\max} . This spiral design algorithm was introduced by Glover. Figure 4.3 shows (a) a single-shot spiral with a 22cm FOV and 6.9mm resolution on a Siemens 3T Trio scanner ($g_{\max}=4\text{g/cm}$, Slewrate= 20000g/cm/s), and (b) its corresponding gradients.

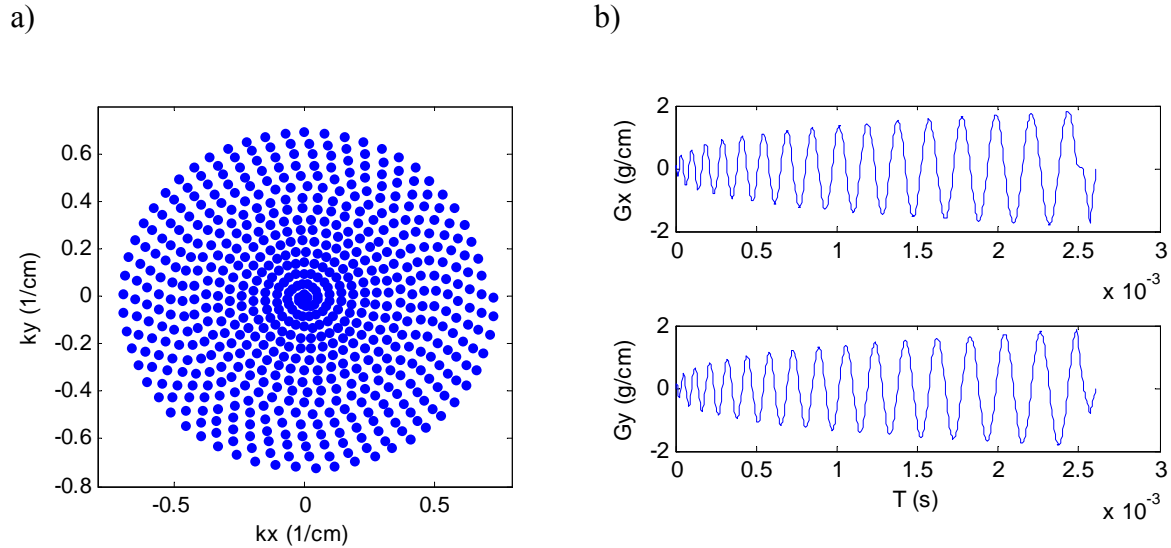


Figure 4.3: a) Single-shot spiral with a 22cm FOV and 6.9mm resolution. b) Its corresponding gradients G_x , G_y .

After we get the trajectory, the next step will be determining the weighting function $W(\mathbf{k})$. For a uniform excitation pattern M_{xy} , e.g. a uniform disc, the k -space weighing should be its Fourier transform which is a jinc function:

$$W(\mathbf{k}) = \text{jinc}(\mathbf{k}) \quad (4.23)$$

where the jinc function is defined as $\text{jinc}(\mathbf{r}) = \frac{J_1(\pi\mathbf{r})}{2\mathbf{r}}$, J_1 is a Bessel function the first kind.

Since a jinc is a function of infinite extent, in the real world, a windowed jinc will be applied. The resulted magnetization M_{xy} will be a convolution of the uniform disc and the Fourier counterpart of the window function $A(r)$. The net result is the excitation profile will have a wider transient.

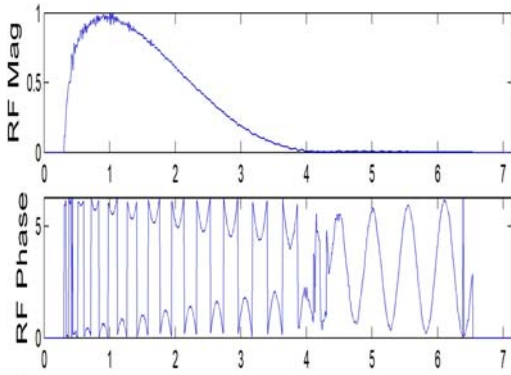
$$W(\mathbf{k}) = \text{jinc}\left(N \frac{\mathbf{k}}{k_{\max}}\right) \cdot A\left(\frac{\mathbf{k}}{2k_{\max}}\right) \quad (4.24)$$

and

$$M_{xy}(\mathbf{r}) \propto \text{circ}\left(\frac{\mathbf{r}}{2N\Delta r}\right) \otimes a\left(\frac{\mathbf{r}}{\Delta r}\right) \quad (4.25)$$

Sampling the $W(\mathbf{k})$ in equation (4.24) along the trajectory $\mathbf{k}(t)$ to get $W(t)$, and the RF waveform $B_1(t)$ will be calculated according to the equation (4.17).

a)



b)

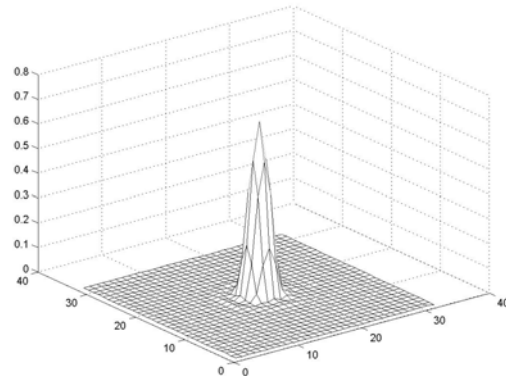
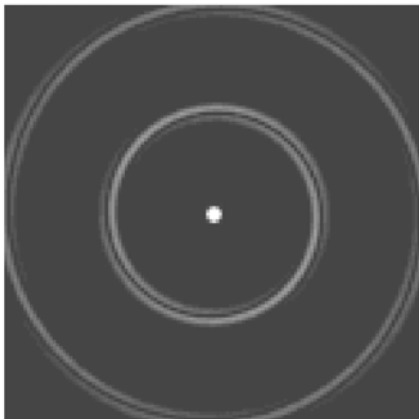


Figure 4.4: a) The spiral RF pulse and its phase. b) The point-spread-function in mesh plot.

In Figure 4.3, we show the designed RF pulse, and its point spread function in mesh plot. In Figure 4.4.a, the point spread function is plotted in an extended FOV so that we can see the side lobes clearly. The profile from the center line of a) is plotted in b). We can see the first side lobe appears at $\pm 22\text{cm}$, which is the defined excitation FOV.

a)



b)

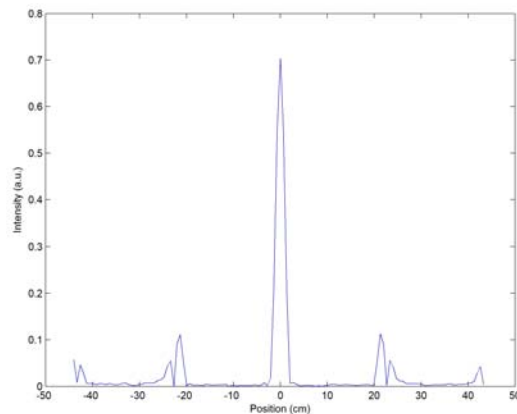


Figure 4.5: a) The point spread function of the spiral pulse in a extended FOV so that we can see side lobes. b) The profile from the center line of a). We can see the first side lobe appears at $\pm 22\text{cm}$, which is the defined excitation FOV.

4.3.2 Off-Center Excitation

Under the small-tip-angle regime, since the RF pulse and the excitation magnetization have a Fourier relationship, an off-center excitation can be easily implemented using a phase modulation.

$$B_{1,s}(t) = B_1(t)e^{-i2\pi\mathbf{k}\cdot\mathbf{r}_0} = B_1(t)e^{i\gamma\int_t^T \mathbf{G}(s)\cdot\mathbf{r}_0 ds} \quad (4.26)$$

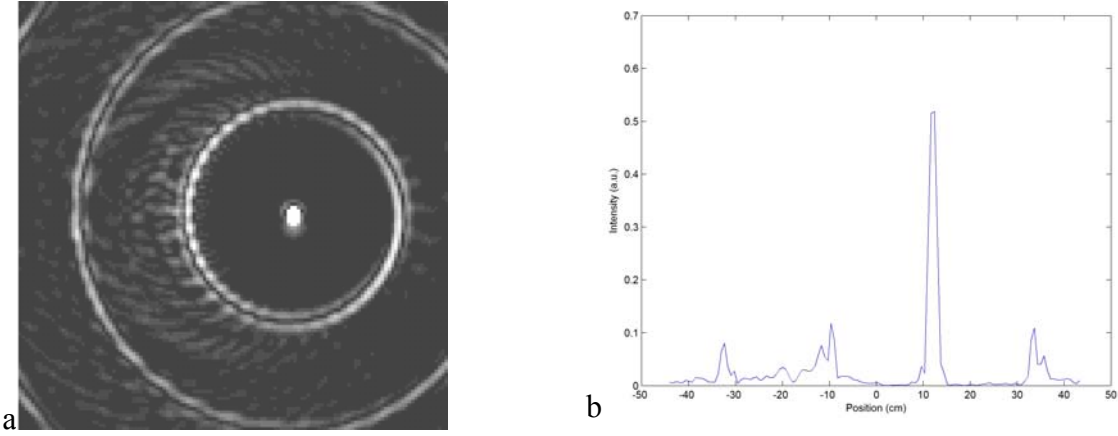


Figure 4.6: The shift FOV by modulation

For the slice-selective pulse, it would be more convenient to use the same RF pulse to acquire multiple slices. The modulation item can be further decomposed as:

$$e^{i\gamma\int_t^T \mathbf{G}(s)\cdot\mathbf{r}_0 ds} = e^{i\gamma\int_{-\infty}^T \mathbf{G}(s)\cdot\mathbf{r}_0 ds} \cdot e^{-i\gamma\int_{-\infty}^t \mathbf{G}(s)\cdot\mathbf{r}_0 ds} \quad (4.27)$$

The first term is a constant phase φ_s . The second term imposes a frequency shift f_s .

$$\varphi_s = e^{i\gamma\int_{-\infty}^T \mathbf{G}(s)\cdot\mathbf{r}_0 ds} \quad (4.28)$$

and

$$f_s = \gamma\mathbf{G}(t)\cdot\mathbf{r}_0 \quad (4.29)$$

For a constant gradient, the frequency and phase shift are both constant. MR hardware can be easily adjusted for it. However, for the time-varying gradient, things are more complicated. On the GE scanner, a separate theta channel can be used to accommodate this frequency shift f_s . On Siemens scanner, however, it is more difficult to realize the off-center excitation since it has no spare channels to play out the time-varying frequency shift.

4.4 3D TAILORED RF PULSE DESIGN

4.4.1 Separable Design

The method to design 2D pulses can be easily extended to more dimensions. 3D tailored RF pulse was first proposed by Pauly et al.(38). It has been demonstrated its usage in correcting for B_0 and B_1 artifacts.(17,19,43) The 3D tailored RF pulse was designed to excite a 3D volume with certain magnetization pattern to compensate for the B_0 or B_1 artifacts.

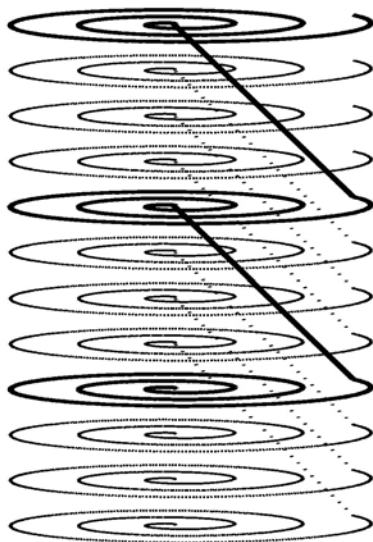


Figure 4.7: The 3D tack spirals trajectory. The transverse plan is sampled with spiral trajectory, and the through-plan is covered using phase encoding.

Giving the consideration of the T_2^* decay, a practical RF pulse normally should be less $3T_2^*$ long. This time limit means that the 3D pulses cannot achieve high resolution in all three dimensions. In this thesis, we will discuss two major types of trajectories to cover 3D k -space. The first samples the in-plane k -space denser and through-plane sparser. A commonly used trajectory in this category is the stack-spirals. (Fig. 4.7) The in-plane is covered with spiral discs, and the through-plane is phase encoded. The high in-plane resolution achieved with spiral sampling is suitable to the localized excitation. Another type, on the other hand, samples through-plane denser and in-plane sparser. EPI trajectories were used in this case. The through-plane direction is frequency-encoded, and each point in the transverse plane (k_x - k_y) is a delta function (Fig. 4.8). The in-plane points can be located on any trajectory as long as this trajectory meets the sampling requirements. The high resolution in the through-plane direction makes this pulse highly slice-selective. The pulse can excite thin slices with a relatively short pulse length. For applications like B_1 inhomogeneity reduction, this pulse is very promising, since the B_1 is smoothly varying in the transverse plane, and does not need high in-plane resolution.

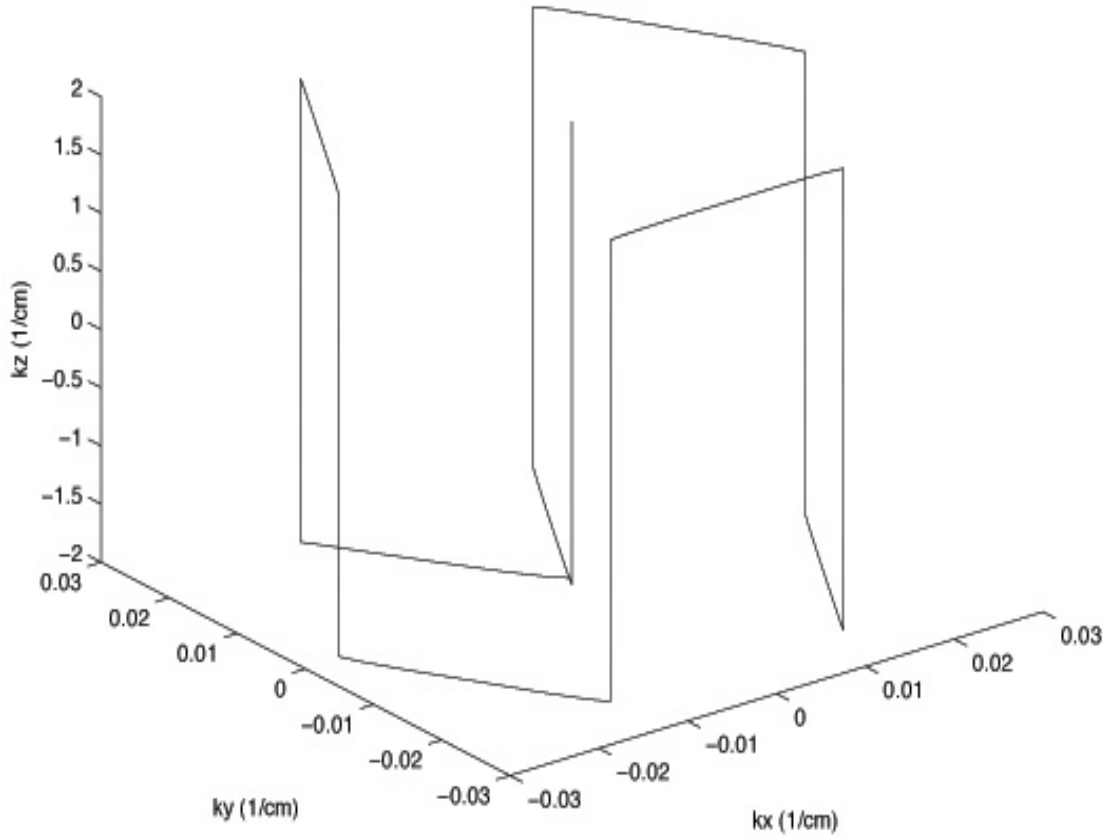


Figure 4.8: The 3D EPI trajectory. The through-plan is sampled densely with frequency encoding, and the transverse plan is sampled sparsely with a hexagonal trajectory.

In both cases, we select separable design for through-plane and in-plane. Then the excitation weighting function $W(\mathbf{k})$ will become:

$$W(\mathbf{k}) = Q(k_x, k_y)P(k_z) \quad (4.30)$$

where $Q(k_x, k_y)$ is the in-plane weighting, and $P(k_z)$ is the through-plane weighting. A simple and practical choice for $P(k_z)$ is a Gaussian profile.

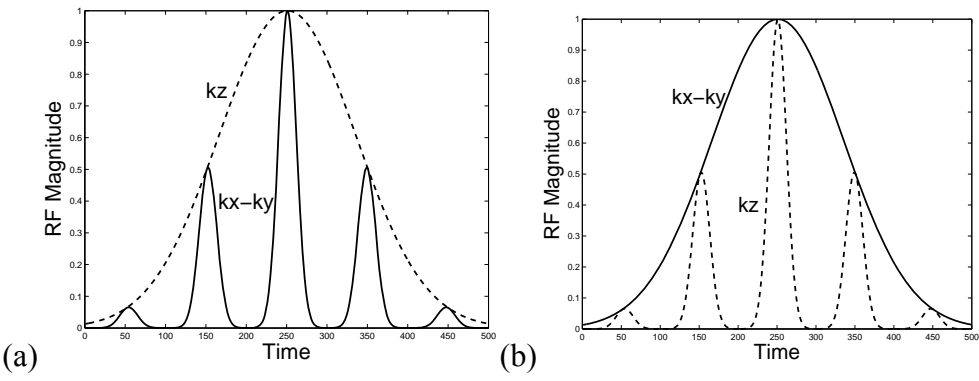


Figure 4.9: 3D TRF pulse designs. (a) Diagram of the RF magnitude envelope and (b) Diagram of the RF magnitude envelope.

Figure 4.9 shows a general explanation of this separable design idea. For the stack of spirals pulses, $Q(k_x, k_y)$ determines the shape of sub-pulses, and $P(k_z)$ determines the envelope. While for the EPI pulses, $P(k_z)$ determines the shape of sub-pulses, and $Q(k_x, k_y)$ determines the envelope. Specifically, for the stack spirals pulse, each sub-pulse is a 2D spiral pulse as we saw previously. The amplitude envelope is the Gaussian determined by $P(k_z)$. For the EPI pulse, each sub-pulse is a 1D Gaussian pulse. The envelope is determined by $Q(k_x, k_y)$ which is the inverse Fourier transform of the transverse magnetization M_{xy} . The points in transverse plane are chosen to be on hexagonal grid shown in Figure 4.10, or even manually selected optimized trajectory as described in Yip's abstract(46).

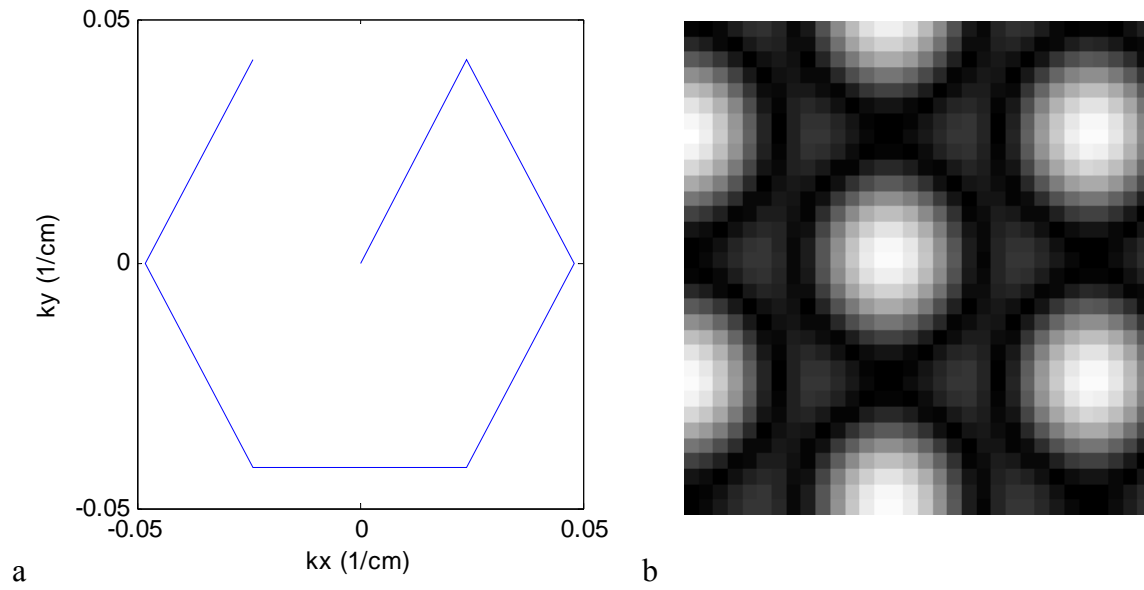


Figure 4.10: a) The hexagonal trajectory used in transverse plane, and b) its point spread function.

5.0 TRANSMIT SENSE

5.1 TRANSMIT SENSE FORMULISM

3D tailored RF pulses are usually too long to be practical. Long pulses are susceptible to T2* and off-resonance artifacts. Given the analogy of excitation and reception, the parallel imaging technique used for the receiving process can be also used in the excitation to shorten RF pulse length or increase excitation resolution. The idea of transmit SENSE was first introduced by Katscher *et al.*(47) and Zhu(48). Katscher *et al.*(47) formulated the transmit SENSE equation based on a convolution of the parallel transmitter sensitivities in excitation k -space. It can be applied to arbitrary k -space trajectories. Zhu(48) formulated the transmit SENSE equation as an optimization problem in the spatial domain. The method is only applied to Cartesian sampling EPI trajectories. More recently, Griswold *et al.* proposed a transmit-GRAPPA method(49). Like the GRAPPA (33) method in receiving part, it does not require a separate scan to calibrate sensitivity patterns. Instead it uses a self-calibration step in the pulse design.

In this thesis, we implemented the transmit SENSE problem using the iterative RF design method in spatial domain proposed by Grissom *et al.*(50)

In equation (4.8), we assumed a single coil with a uniform transmit sensitivity. A more generalized form for a phased array coil with independent transmit sensitivities will be:

$$M_{xy}(\mathbf{r}) = iM_0 \sum_{n=1}^{N_c} s_n(\mathbf{r}) \int_{-\infty}^T \gamma B_{1,n}(t) e^{i2\pi\mathbf{k}(t)\cdot\mathbf{r}} dt \quad (5.1)$$

where $s_n(\mathbf{r})$ and $B_{1,n}(t)$ are the transmit sensitivity and RF waveform of the n^{th} coil for the phased array coil with N_c elements. Discretizing time t and space \mathbf{r} to N_t and N_s samples respectively, we can write equation (5.1) into a matrix formula:

$$M = A_{full} B_{full} \quad (5.2)$$

where M is a discretized column vector for the desired excitation pattern; B_{full} is the vertical concatenation of the discretized column vector of the RF waveform; and the individual items in the matrix A_{full} will be:

$$a_{i,(n,j)} = i\gamma M_0 \Delta t s_n(r_i) e^{ik(t_j)\cdot r_i} \quad (5.3)$$

Least squares minimization approach can be used to estimate the N_c RF pulses,

$$B_{full} = \arg \min_{B_{full}} \|A_{full} B_{full} - M\|^2 \quad (5.4)$$

A more sophisticated formulism to solve for B_{full} can include regularization terms in the minimization problem as described in reference (50)

$$B_{full} = \arg \min_{B_{full}} \left\{ \|A_{full} B_{full} - M\|_W^2 + R(B_{full}) \right\} \quad (5.5)$$

where W is a diagonal weighting matrix which can be used to increase the excitation accuracy of the specified region. $R(B_{full})$ is a regularization term which can be used to control RF power, excitation accuracy or waveform smoothness.

5.2 TRANSMIT SENSE NUMERICAL SIMULATION

As a simulation demonstration of the algorithms, we took a gray-scaled jpeg of a girl and sensitivity maps measured from a phased array receiver on the 1.5T GE scanner (MRI Devices, Gainesville, FA) and designed an $R = 2$ transmit SENSE 2D TRF pulse that excites a 64×64 image using Matlab (The Mathworks Inc., Natick, MA). We used a standard conjugate gradient algorithm included in the Matlab package to perform the least squares solution. The sensitivity maps were estimated from images of a uniform phantom acquired with each receiver and dividing by a body coil reference image. The quotient was smoothed using a Gaussian filter and the sensitivity maps were derived from a 2D fit using a 3rd order polynomial. Figure 5.1 (a) shows an input jpeg of the girl. Figure 5.1 (b) shows real and imaginary images of the four sensitivity maps estimated from the four-channel phased array coil. Shown below are the corresponding Bloch equation simulations of the magnetization profiles produced by each transmitter displayed as real and imaginary images. Figure 5.1 (c) shows the Bloch equation simulation result of the girl's face. The final result was obtained by taking the magnitude after summing the individual complex images shown in the bottom of (c).

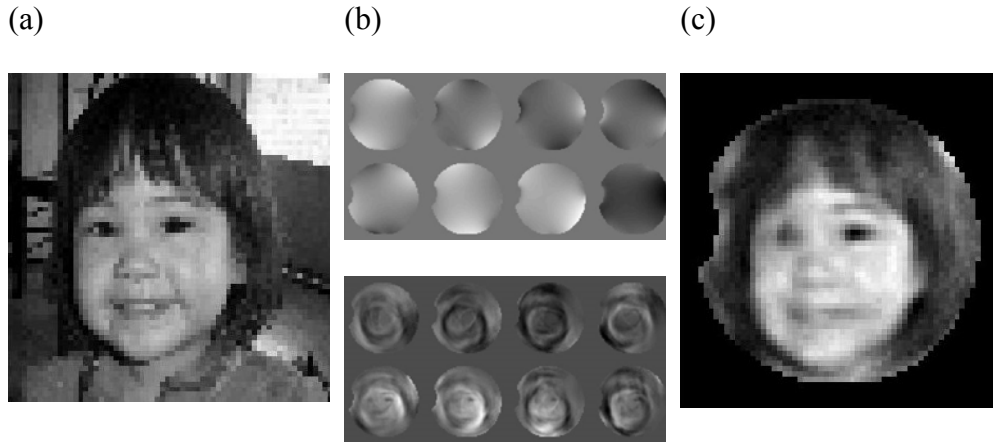


Figure 5.1: Transmit SENSE simulation. (a) Input jpeg image. (b) (Top) Sensitivity maps measured from array coil displayed as real and imaginary images. (Bottom) Real and imaginary magnetization profiles from Bloch equation simulations. (c) Complex summation of the magnetization from all transmitters.

Using the numeric simulation, we calculated the point spread function of the transmit SENSE 3D pulse with the EPI design. In the implementation of SENSE problem, we fixed the length of R pulses, and use the sensitivities to increase the resolution. In Figure 5.2, we show the profiles from the center line of the PSFs. The narrower peaks with the increased reduction factor R demonstrate the increased pulse resolutions. As we should notice that the inclusion of sensitivities alone (R=1 transmit SENSE pulse) will increase the pulse resolution. However, the ill-posed sensitivity matrix inverting gives rise to residual artifacts as shown with the arrow bar in the figure.

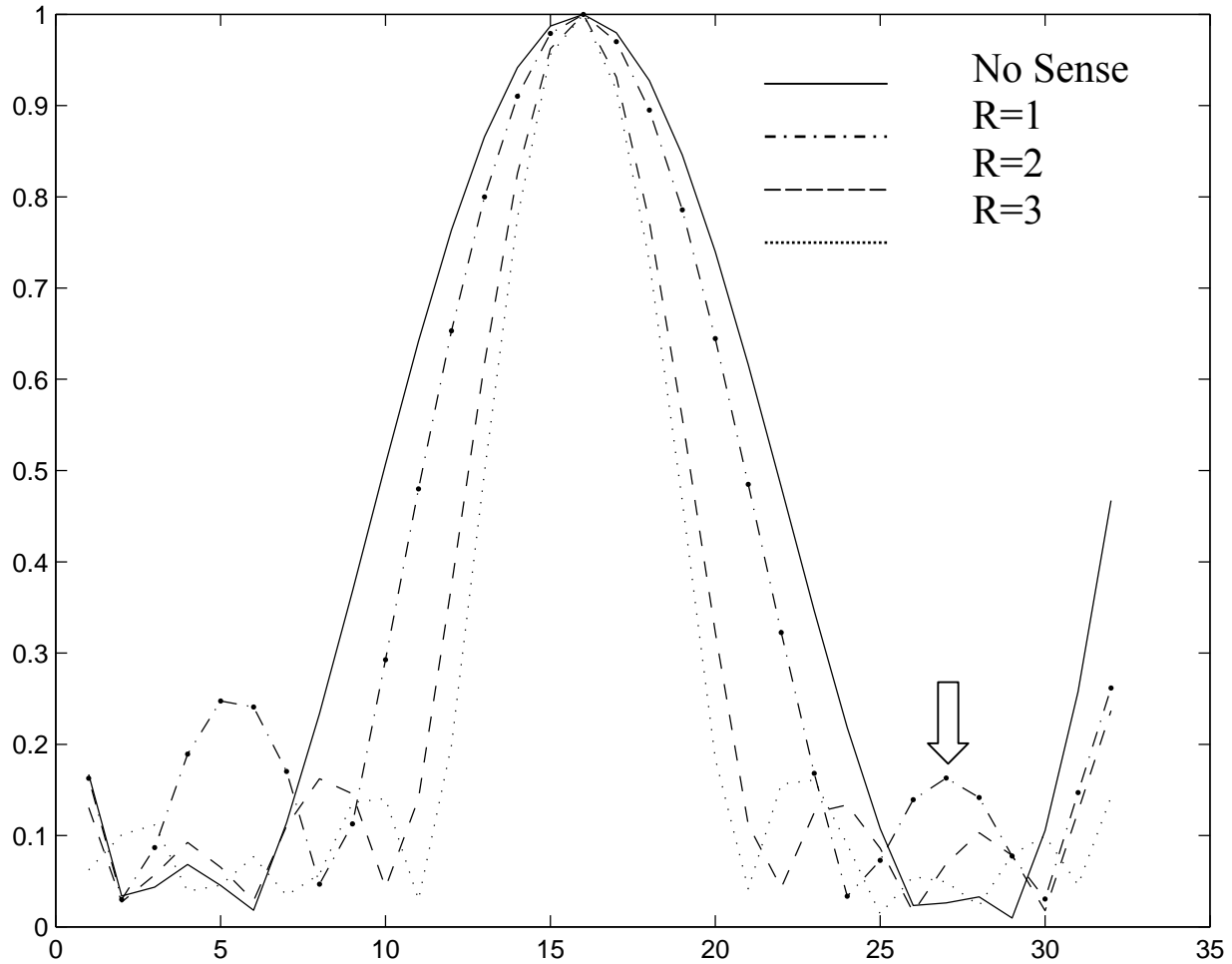


Figure. 5.2: The point spread function profile of the 3D EPI pulse. The resolution is increased with the SENSE reduction factor.

5.3 PSEUDO-TRANSMIT SENSE

Given the limit that current commercial scanners have only one independent transmit channel, real transmit SENSE experiments cannot be performed directly. Most experimental validations were done by transmitting the waveforms through different transmit coil elements individually in sequential measurements. However, using this method, a multi-element transmit coil is needed

and the elements need to be decoupled. We introduced a pseudo-transmit SENSE method to mimic real transmit SENSE experiment using widely available hardware.(50,51)

Exploiting the linearity assumption between the reconstructed images, transmit sensitivity, and receive sensitivity in the small-tip-angle approximation, we can swap the roles of the non-uniform transmit sensitivity patterns of the transmit coil array with the uniform receive sensitivity pattern of the body coil in the signal equation. Specifically, we will use the body coil to transmit N unique RF pulses separately in N successive scans. During each scan, measurements are acquired on the phased-array coil element whose sensitivity is the same as that used in the RF pulse being played. The complex measurements of each scans are added together to mimic a transmit SENSE experiment of an N-element phased-array coil transmission and body coil reception.

Mathematically, we can prove the equivalency of this pseudo-transmit SENSE and transmit SENSE experiments. Neglecting off-resonance and T_1 and T_2 decay, the combined image $I(\mathbf{r})$ in the pseudo-transmit SENSE experiment is given by:

$$I(\mathbf{r}) = \sum_{n=1}^N C_n(\mathbf{r}) \cdot (s(\mathbf{r})M_n(\mathbf{r})) = is(\mathbf{r})M_0 \sum_{n=1}^N C_n(\mathbf{r}) \int_{-\infty}^T B_{1,n}(t) e^{i2\pi\mathbf{k}(t)\cdot\mathbf{r}} dt \quad (5.6)$$

where $C_n(\mathbf{r})$ is the receive sensitivity of the n^{th} coil, $s(\mathbf{r})$ is the transmit sensitivity of the body coil, and $M_n(\mathbf{r})$ and $B_{1,n}$ are the excitation pattern and the RF pulse corresponding to the n^{th} coil, respectively.

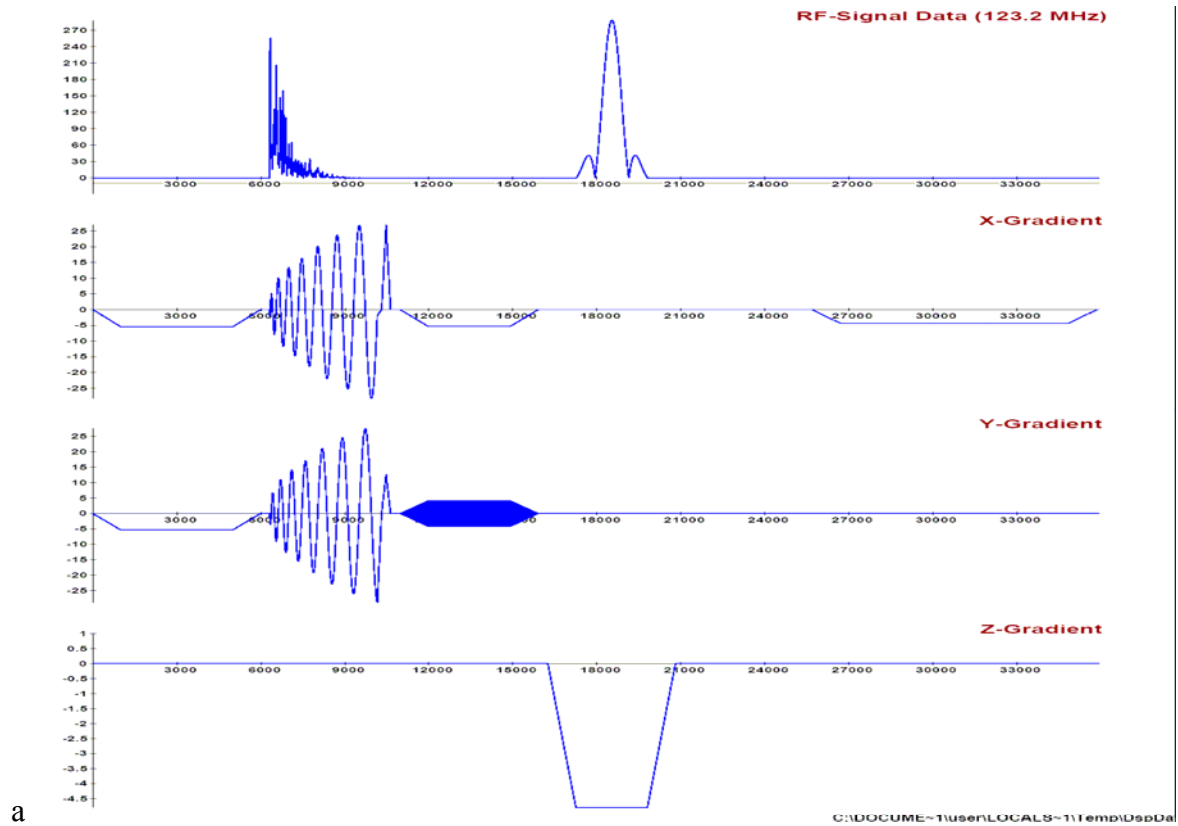
For the real transmit SENSE experiment, the body coil image $I(\mathbf{r})$ will be:

$$I(\mathbf{r}) = C(\mathbf{r}) \sum_{n=1}^N s_n(\mathbf{r}) M_n(\mathbf{r}) = i C(\mathbf{r}) M_0 \sum_{n=1}^N s_n(\mathbf{r}) \int_{-\infty}^T B_{1,n}(t) e^{i2\pi \mathbf{k}(t) \cdot \mathbf{r}} dt \quad (5.7)$$

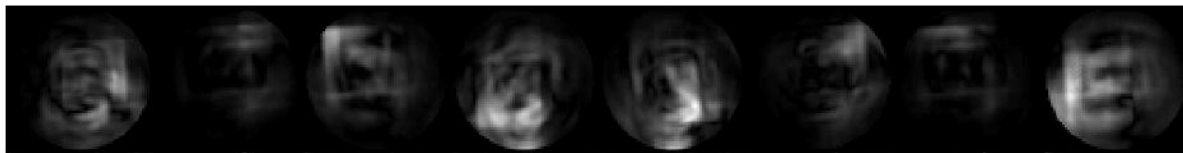
where $s_n(\mathbf{r})$ is the transmit sensitivity of the n^{th} coil, $C(\mathbf{r})$ is the receive sensitivity of the body coil. Assuming that the body coil has a uniform transmit and receive sensitivity (i.e., $s(\mathbf{r})=C(\mathbf{r})=1$), and we can find a phased-array receive coil whose receive sensitivity patterns are the same as the transmit sensitivity patterns of the phased-array transmit coil (i.e., $C_n(\mathbf{r})=s_n(\mathbf{r})$), images generated from equations (5.6) and (5.7) are the same.

In general, this approach may not produce transmit patterns that are realizable in arbitrary objects, but it does allow for testing of the pulse design method. The procedure is useful for validating pulse design methods without requiring parallel transmit hardware that is still in the early stages of development.

Here is an example of our pseudo-transmit SENSE experiment on a 3T Siemens Trio Scanner. We excited an Einstein face. The images were acquired using spin-echo sequence on a uniform ball phantom.



a



b



c

Figure 5.3: (a) One of the eight pulses we applied. This pulse used a spiral trajectory to achieve high resolution in transverse plane, and was embedded into a spin-echo sequence. (b) The 8 individual images resulted by the 8 pulses on corresponding coil elements. (c) The complex sum of the 8 images in Fig. 2, which is the R=3 transmit SENSE pulse image.

5.4 VARIABLE DENSITY EXCITATION WITH TRANSMIT SENSE

The idea to use a variable density trajectory to sample the k -space in image acquisition can be also applied to the RF pulse design in the small-tip-angle regime. The pulse lengths can be shortened by undersampling the edge of the k -space. Since the k -space is predominantly weighted around the center, the undersampling gives rise to a small amount of artifacts. The variable density trajectory can be used in the transmit SENSE pulse design. With a little bit of oversampling at the center k -space for the high reduction factor transmit SENSE pulse, we are able to greatly reduce the aliasing artifacts. In figure 5.4, we show a uniform phantom images acquired with an L-shape excitation pattern using a 2D TRF transmit SENSE pulse with variable density spiral trajectories. The images from the upper row use uniform density spiral trajectories with different transmit SENSE reduction factors. The images from the lower row use variable density spiral which maintain the sampling density at the center k -space (first 150 points) as that of the $R=1$ case, and down sampling at the edge k -space. RF pulse lengths are shown underneath images. We can see the excitation imperfections are greatly reduced with a little bit longer pulse length due to the oversampling at the center k -space.

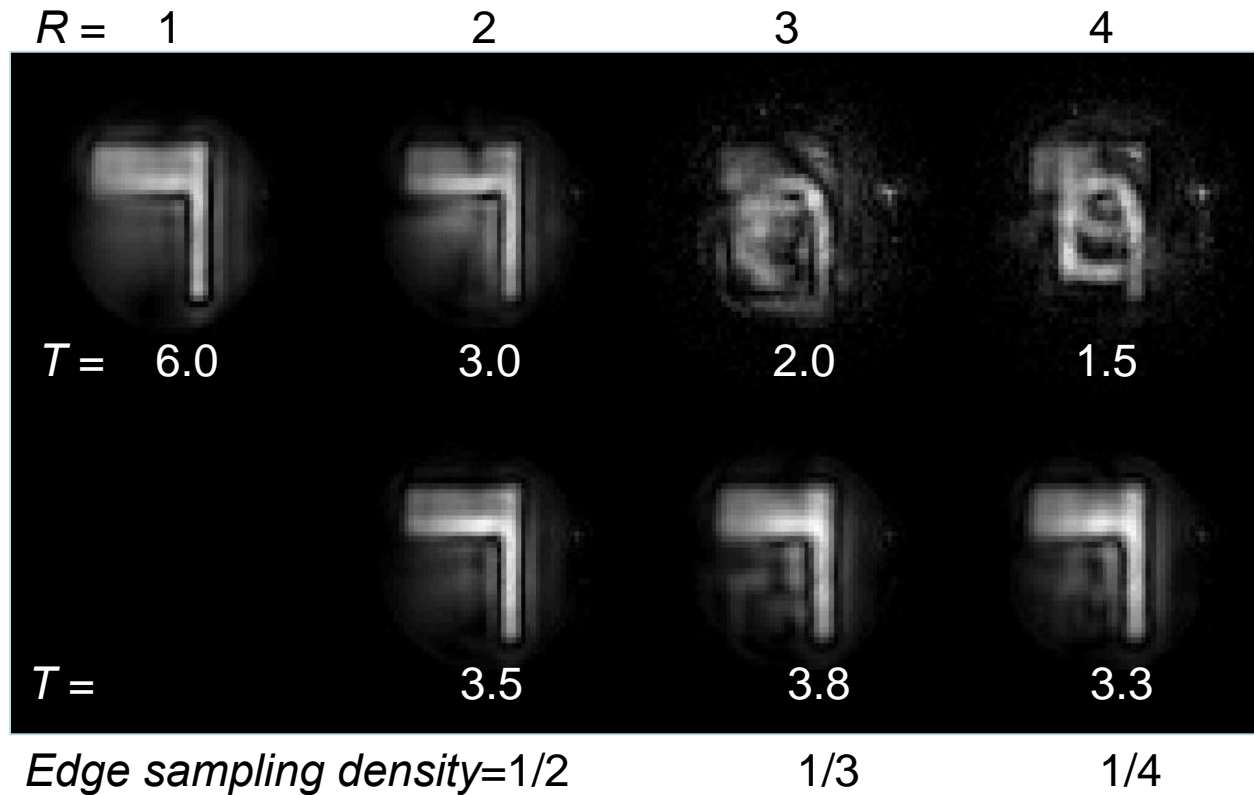


Figure 5.4: 2D L-shape transmit SENSE pulse images acquired with a SE sequence on a uniform ball phantom. The upper row uses uniform spiral trajectory with different reduction factors R from 1 to 4. The lower row uses variable density spirals that maintain the sampling density at the center k -space as that of the $R=1$ uniform spiral trajectory, while undersampled at the edges of k -space. RF pulse lengths are shown underneath images.

5.5 SPECIFIC ABSORPTION RATE (SAR)

RF pulses will deposit energy in the object being imaged. The energy of MR systems is not efficiently used and only part of the energy is transmitted to the spin systems to create the MR signal. Most of the energy is deposited in the tissue as heat which is a safety issue for in-vivo MR experiments.

The specific absorption rate (SAR) is defined as the RF power in watts absorbed by one kilogram in an object. It is an indicator of the risk of body temperature increase. The SAR increases with the main field strength, the RF pulse power and duty cycle(45).

$$SAR \propto B_0^2 B_1^2 \Delta f \quad (5.8)$$

For the field strength up to 1.5T, the SAR is seldom a big concern. However, for the high field MRI, the SAR is always an important issue to consider when designing experiments. Inhomogeneity of RF field causes the power deposited non-uniformly in different part of the object. This is called the local SAR. Regions have the highest local SAR are called hot spots, which should be monitored carefully to make sure no damages are exposed to the body. The global SAR is the local SAR average over the whole body. The FDA guidelines for MRI experiments SAR (52) is:

1. 4W/kg averaged over the whole body for any 15 minutes period.
2. 3W/kg averaged over the whole head for any 10 minutes period.
3. 8W/kg for the local SAR in head or torso for any 5 minutes period.
4. 12W/kg for the local SAR in extremities for any 5 minutes period.

The transmit coil selection and the object position can also affect the SAR. The bigger volume coil generally has a larger SAR than the smaller surface coils. Experiments with objects placed near the isocenter also have smaller SARs than those with objects placed off-center.

In transmit SENSE experiments, the ill-posed sensitivity matrix inverting will penalize the SAR, which is parallel to the SNR penalty in the receive SENSE experiments.

Numerical simulation using the FDTD tool can be used to calculate the local and global SAR(13). This can be used as a valuable tool to guide the coil and experiment design. In figure

5.5, we show a SAR calculation of our transmit SENSE 3D TRF pulses provided in courtesy of Collins.

We simulated a two-element coil placed at the back of a 3D human head model (Figure 5.5a). The coils were tuned to 128 MHz with equal currents (1A) and 90° phase difference. The resulting magnetic field magnitude was shown in (b). The SAR distribution was shown in (c). The average SAR and the maximal SAR over 1g of tissue were found to be 0.12 W/kg and 2.56 W/kg assuming using a rectangle 5 ms long pulse and a minimum TR of 50 ms, which is well below the FDA requirements. The 5 ms rectangular pulse is capable of a 77° flip angle in a $1 \mu\text{T}$ B_1 field, which is adequate for fMRI studies.

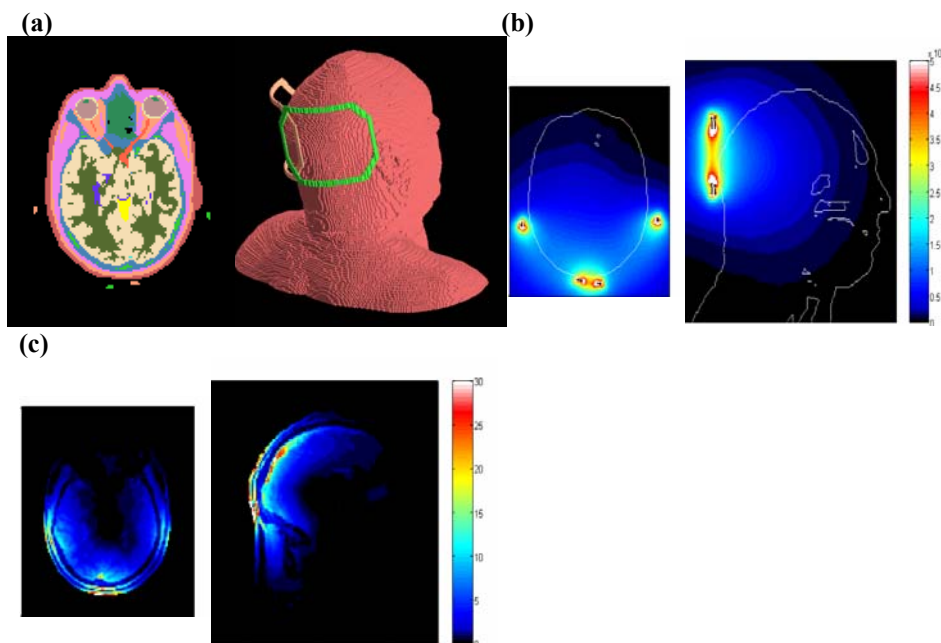


Figure 5.5. SAR Calculations. (a) Geometry of two coils and the head model on axial plane through level of eyes (left), and 3D shaded surface diagram (right). (b) Magnetic field magnitude (μT) on axial plane through level of eyes (left), and mid-sagittal plane (right). White contour shows interface between tissue and air. (c) SAR magnitude (W/kg) at a resolution of $(2\text{mm})^3$ on axial plane through level of eyes (left), and mid-sagittal plane (right). (in courtesy to Dr. Collins)

6.0 REDUCTION OF B₁ INHOMOGENEITY WITH TRANSMIT SENSE SLICE-SELECT PULSES

6.1 INTRODUCTION

The advantages of MRI at high static magnetic field strengths ($B_0 \geq 3T$) include increased signal to noise ratio (SNR) (2) and increased BOLD functional MRI contrast (4). A confound at high field, however, is increased artifact from RF field (B_1) inhomogeneity (53,54). The two factors that produce B_1 inhomogeneity are the shorter RF wavelength that is further shortened by the dielectric properties of tissue and the attenuation of RF amplitude due to tissue conductivity (15,16,55). These artifacts typically appear in the images as regions increased and decreased brightness at 3T (56). The brightness can lead to a loss of contrast in the image and an improper measure of the spin density.

Numerous methods have been proposed to mitigate B_1 inhomogeneity artifacts. These include specially designed coils (11,20), adiabatic pulses (57), image post-processing (58), and small-tip-angle tailored RF (TRF) pulses (43,59,60). TRF pulse techniques have the advantage of being able to compensate for the transmit B_1 inhomogeneity using a predetermined spatial excitation. More recently, it has been shown that “ B_1 shimming” can be performed using multiple transmitters (61,62). A homogenous slice can be achieved by adjusting the magnitude and phase

on each transmitter channel until a uniform composite excitation is obtained. The disadvantage of this approach is that there is no straightforward way to relate the observed inhomogeneity to the required RF pulse parameters for each transmitter.

Recently our group has proposed that the transmit sensitivity encoding (transmit SENSE) techniques (47,48) can also be used to reduce B_1 inhomogeneity (63). The concept behind the use of transmit SENSE is that the resultant TRF pulses will be inherently compensated for inhomogeneity in the transmit B_1 by the inclusion of transmit coil sensitivities in the pulse design. Furthermore, the use of the coil spatial information allows for either reduce pulse lengths or increased excitation resolution. Although this concept has been validated with parallel transmit hardware using a two-dimensional TRF pulse in a spin-echo sequence in phantoms (64), there has been no demonstration using a practical slice-select three-dimensional (3D) TRF implementation in vivo. Furthermore, there has been no concise theoretical description of the inherent B_1 compensation provided by transmit SENSE.

This chapter presents in vivo proof of concept data using an transmit SENSE implementation of the “fast- k_z ” 3D TRF pulse design (46) that can be used to excite 2-5 mm thick slices with pulse lengths of 4-5 ms. Parallel transmit hardware was mimicked using an eight channel receiver and body coil (51,65). The pulse was shown to reduce B_1 inhomogeneity in both uniform phantom and human brain images at 3T.

6.2 THEORY

Assuming small flip angles, the composite spatial excitation profile $w(\mathbf{r})$ from N simultaneous 3D TRF pulses can be written as the sum of the individual excitation profiles produced by each pulse

$$w(\mathbf{r}) = \sum_{n=1}^N w_n(\mathbf{r}) = p(z) \sum_{n=1}^N q_n(x, y) \quad (6.1)$$

Here $p(z)$ is the excitation profile along the slice-select direction, which we will make identical for all pulses such that there is a uniform slice thickness. The term $q_n(x, y)$ represents the in-plane excitation profile that we have the freedom to control with the pulse design provided that we have adequate pulse k -space sampling. The actual profile $w_{\text{act}}(\mathbf{r})$ that gets excited in the object will then be

$$w_{\text{act}}(\mathbf{r}) = p(z) \sum_{n=1}^N \alpha_n(x, y) q_n(x, y) \quad (6.2)$$

where $\alpha_n(x, y)$ is the transmitter sensitivity or equivalently the transmit B_1 inhomogeneity. If we desire a uniform image with a slice thickness defined by the width of $p(z)$ then

$$\sum_{n=1}^N \alpha_n(x, y) q_n(x, y) = 1 \quad (6.3)$$

This can be rewritten using the Fourier transform $Q_n(k_x, k_y)$ of the in-plane excitation profile

$$\sum_{n=1}^N \alpha_n(x, y) \int Q_n(k_x, k_y) e^{-ik_x x - ik_y y} dk_x dk_y = 1 \quad (6.4)$$

This equation is now easily recognizable the image domain transmit SENSE equation (50) with the restriction that the resultant magnetization be constant. The inclusion of the spatial

sensitivities of the multiple transmitters also allows for reduced sampling in k_x - k_y , which translates to shorter pulses or higher excitation resolutions. This equation can be rewritten as a matrix equation

$$\alpha Q = 1 \tag{6.5}$$

and approximate solutions for Q can be obtained by least squares minimization

$$Q_{\text{app}} = \underset{Q}{\text{argmin}} \|1 - \alpha Q\|^2 \tag{6.6}$$

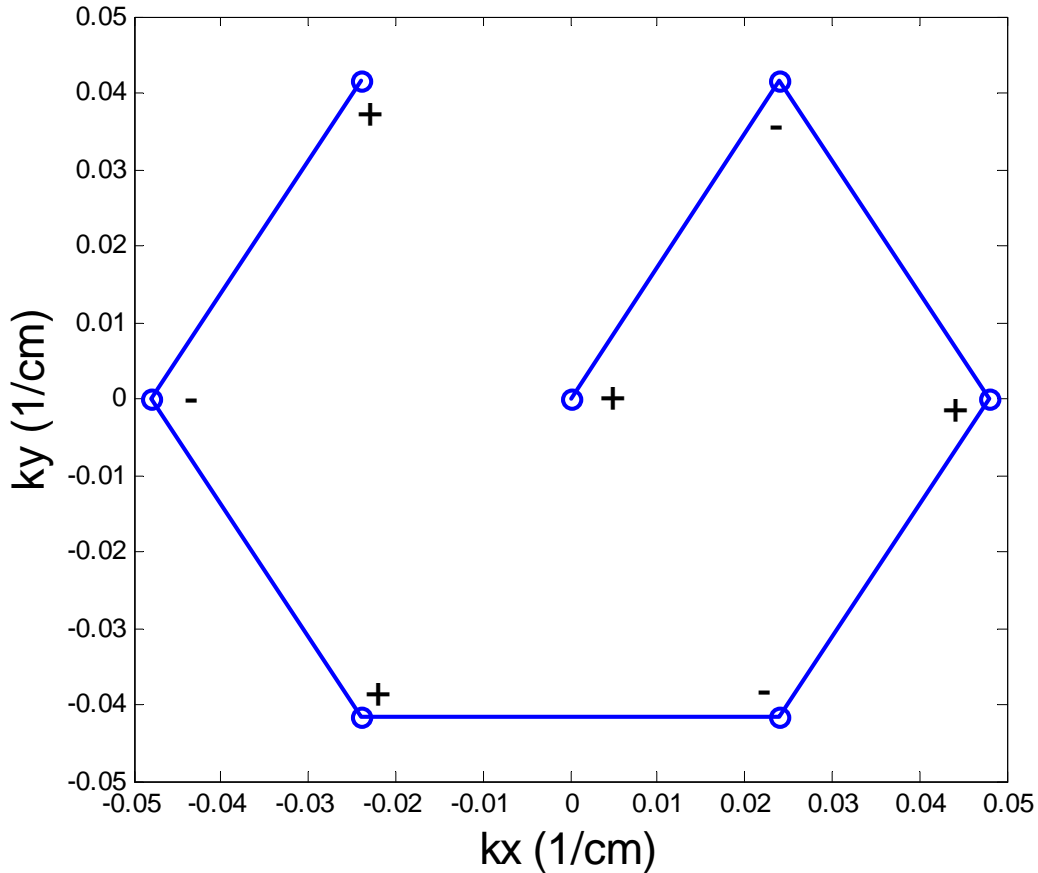


Figure 6.1: Hexagonal k -space trajectory of the transmit SENSE 3D “fast- k_z ” TRF pulse in k_x - k_y plane. Each sampling point (circle) corresponds to a vertical line along the k_z direction. Polarities of these k_z lines are shown with the position (+) and negative (-) signs.

The requirements of the above theoretical arguments are easily implemented using the “fast- k_z ” pulse design, which consists of a train of slice-select sub-pulses with shape $P(k_z)$ separated by phase encoding blips in x and y . This design is optimal if thin slices are required along z with no sidelobes and minimal resolution in x - y is desired. This is the case for a slice-select 3D TRF pulse that compensates for a smoothly varying transmitter inhomogeneity. Figure 6.1 shows the k_x - k_y sampling used in the pulse design, which was chosen to be hexagonal for optimal alias placement. Each point corresponds to the location of one of seven slice-select sub-pulses, where the sign corresponds to the polarity of the z -gradient. The transmit SENSE acceleration factor R stretches the spacing between adjacent k -space sampling points. Figure 6.2 shows an example a fast- k_z transmit SENSE 3D TRF pulse for one transmitter that was used in the human imaging experiments. Further details of the pulses are given below in the Methods section.

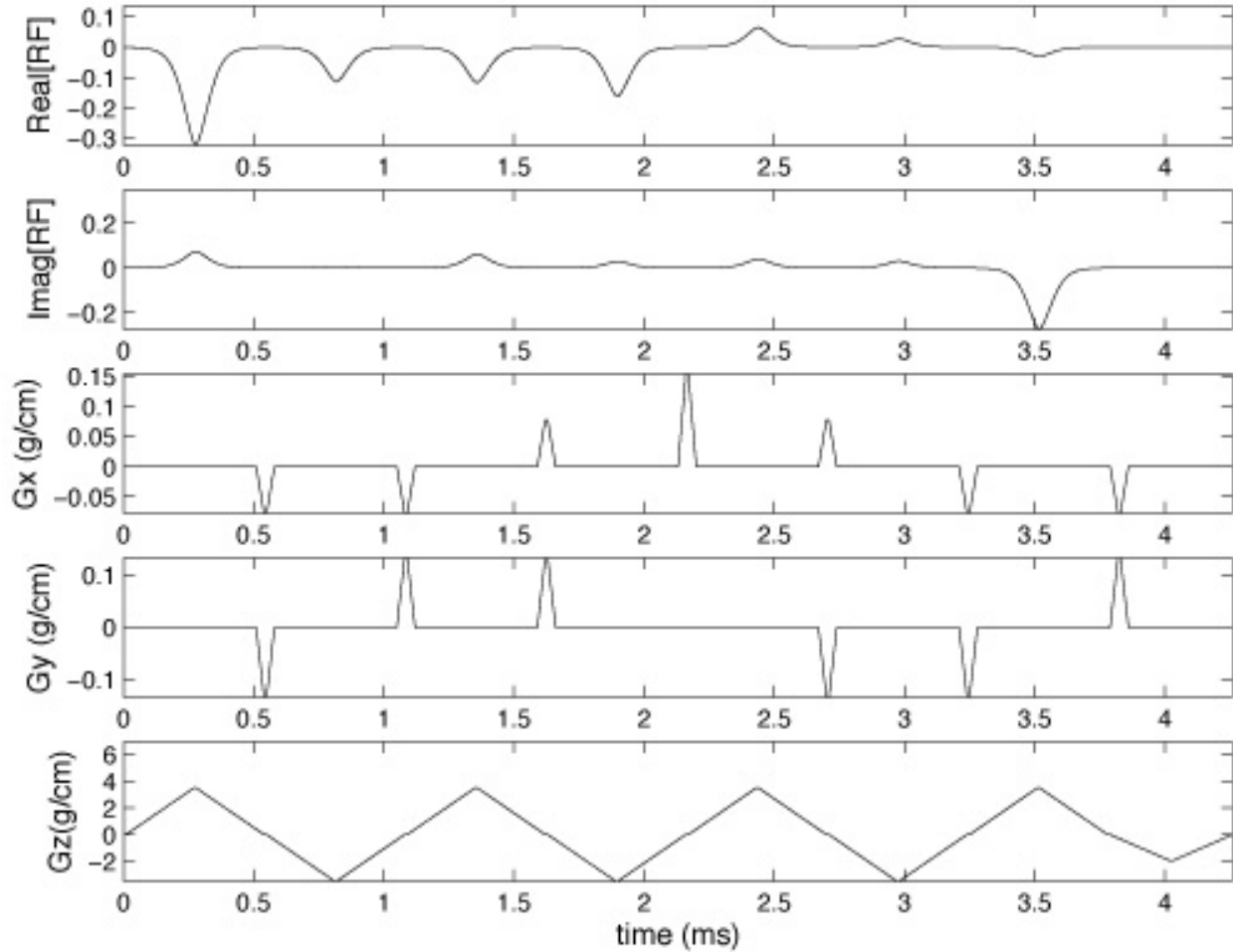


Figure 6.2: One of the eight $R=2$ transmit SENSE pulses used in human brain images. The rows from top to bottom are the real and imaginary parts of the RF, and the x , y , and z gradients.

6.3 METHODS

The transmit SENSE 3D TRF pulses were designed for use on a Siemens 3T Trio scanner (Siemens Medical Systems, Erlangen, Germany). The gradient slew rate and peak were 200 T/m/sec and 40 mT/m. Due to a lack of parallel transmit hardware, the pseudo-transmit SENSE method described in section 5.3 was used to validate the effectiveness of the transmit SENSE pulses. For B_1 inhomogeneity reduction experiments, the transmit SENSE pulses consisted of

seven sub-pulses giving total length of 4.3 ms. The excitation resolution was 3.7 cm over a 22 cm excitation FOV. The reduction factor of transmit SENSE, R , was used to increase the pulse resolution. An $R=1.5$ transmit SENSE 3D TRF pulse was designed by stretching the spacing between two adjacent k-space sampling points with a 1.5 factor. The corresponding resolution of the pulse was 2.5 cm. The slice-select profile $p(z)$ was chosen to be Gaussian with a half width of 5 mm.

The coil sensitivity maps were determined with an iterative fitting method (37) using images acquired with the body coil and from each receiver during a two-minute pre-scan. Figure 6.3 shows an example of the eight sensitivity maps for one slice in one subject. Once the sensitivity maps were determined for the slices of interest, the amplitudes Q of each sub-pulse were determined from Eq. (6.6) using a conjugate gradient technique. The pulse construction programs were executed using Matlab (The Mathworks, Natick, MA), taking approximately 1-2 seconds. The pulses were then replaced the regular SINC pulse in a standard FLASH sequence to acquire images with matrix size of 128^2 over a 22 cm FOV.

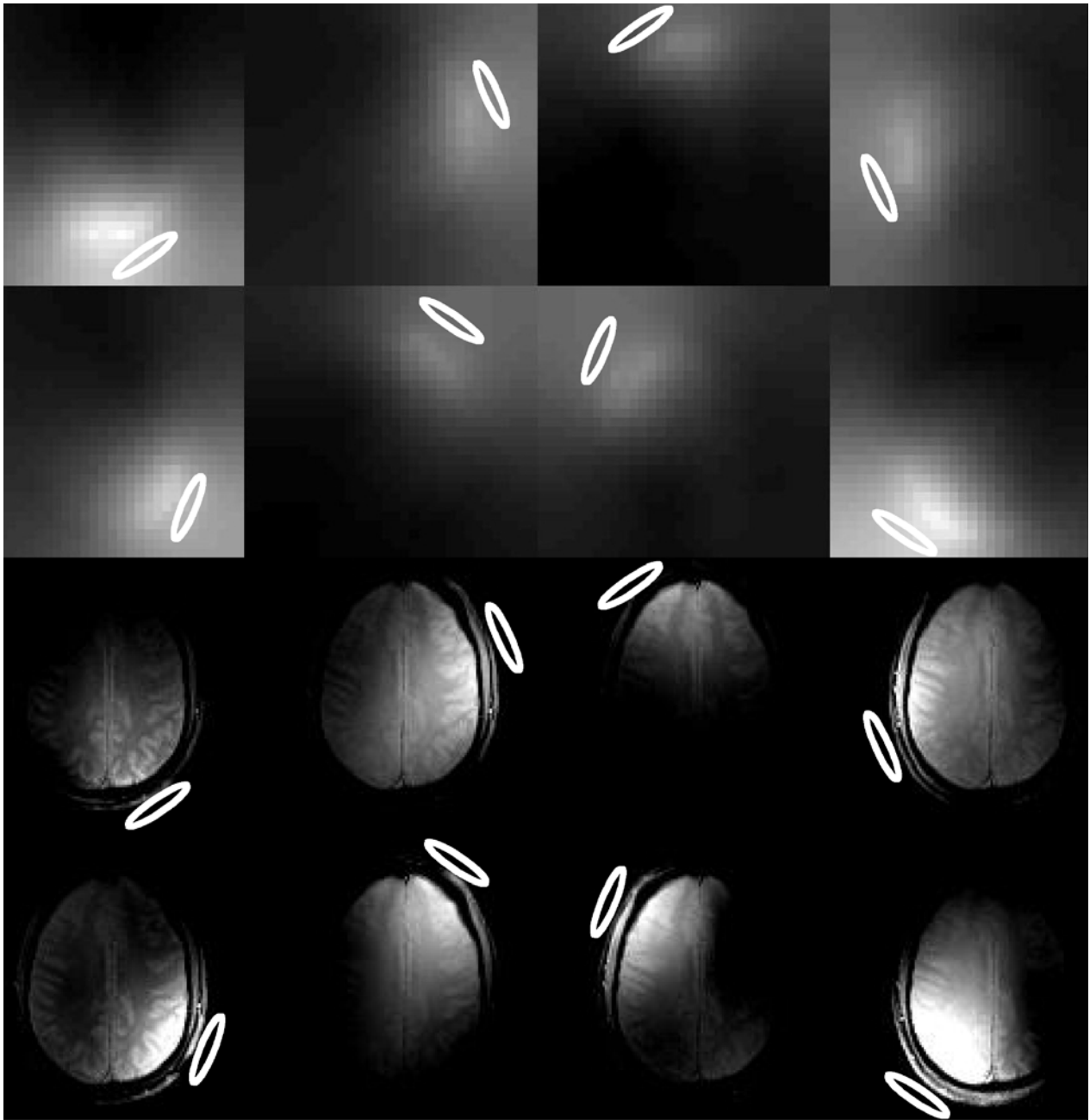


Figure 6.3: The coil sensitivity of the eight-channel phased array coil (up row), and the eight individual coil images of a R=2 transmit SENSE 3D TRF pulse. The complex sum of the eight images is shown as Slice 1 in Fig. 6.6

A phantom study with readout along the z direction was used to verify the accuracy of z profile.

The imaging parameters were TE = 15 ms, TR = 100 ms, and Flip Angle = 3°. One-dimensional

profile was plotted from the z read image. The slice thickness was measured by a least squares fit of the histograms with a Gaussian function $g(x)$,

$$g(x) = ae^{-\frac{(x-b)^2}{c^2}} \quad (6.7)$$

The parameters a , b , and c were determined by the fitting procedure. The full width half maximum (FWHM) of the histograms was calculated with

$$\text{FWHM} = 2\sqrt{\log 2}c \quad (6.8)$$

To demonstrate B_1 inhomogeneity reduction effects of transmit SENSE 3D TRF pulses, both uniform ball phantom and human brain images were acquired and compared with the images acquired with standard SINC pulse with same imaging parameters. For phantom study, TR was 100 ms. Since the uniform ball phantom has a high conductivity, the excitation profile was chosen to be an inverted Fermi-like function to compensate for the non-uniformity of the body coil transmitter. Both $R=1$ and $R=1.5$ transmit SENSE pulses were applied, and a comparison was shown. For the human brain experiment, TR was 300 ms, and a uniform excitation profile was applied. Other parameters were the same for both experiments which were TE = 15 ms, FOV = 22 cm, Flip Angle = 30° , and matrix size = 128^2 . Final images from the standard pulse were obtained from either a complex summation or from a magnitude sum of squares of the individual coil images; representing either a simultaneous excitation with multiple transmitters without transmit SENSE or the standard receiver array image, respectively. Four normal adult human subjects were studied under approval of the University of Hawaii and Queens Medical Center Joint Institutional Review Board.

Two methods were used to analyze B_1 inhomogeneity in the resultant slices. The first approach constructed histograms of the image magnitude distributed among all of the pixels in an image. A smaller width of the histogram is indicative of the degree of magnitude uniformity. The width was determined by a least squares fit of the histograms with a Gaussian function in the same way as described in the experiment to determine slice thickness.

The second method was to calculate the normalized standard deviation (SD/Mean) of all of the pixel magnitudes in a given slice, excluding the region outside brain (66). A larger standard deviation is indicative of a large degree of B_1 inhomogeneity. The data analyses and statistical methods were all performed using Matlab.

6.4 RESULTS

Figure 6.4 shows the image with readout along the z axis on the left. A profile through centerline is plotted on the right together with the Gaussian fitting curve. The measured FWHM of the Gaussian is 4.7 mm which is approximate the prescribed 5 mm slice thickness.

a



b

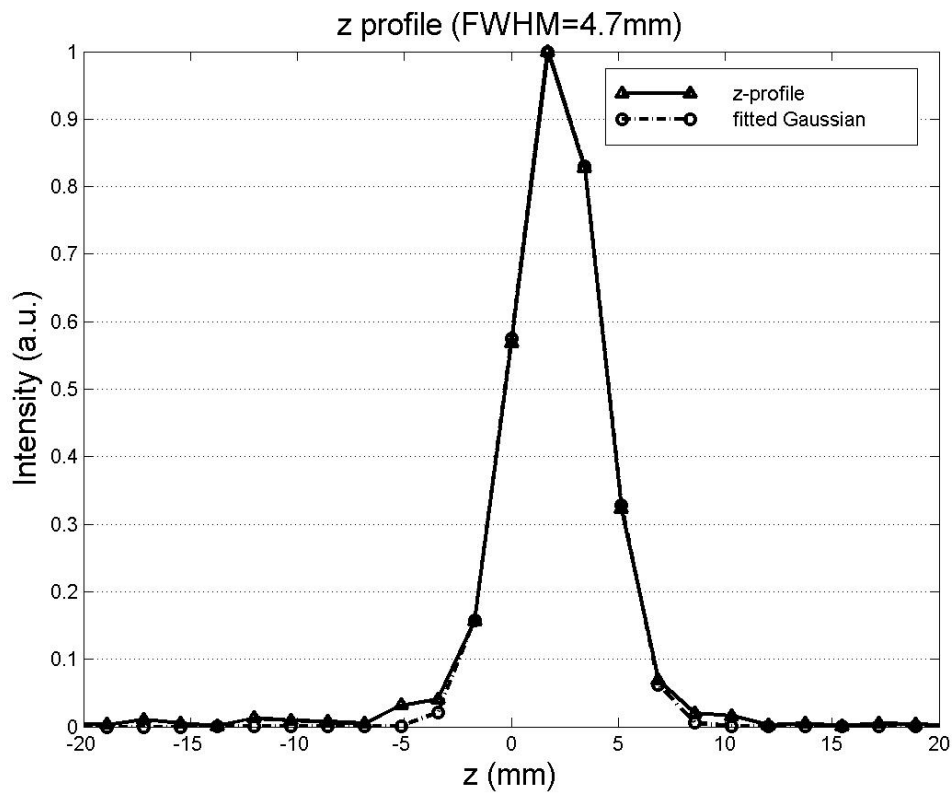


Figure 6.4: The slice profile along the z axis. (a) The transmit SENSE 3D TRF pulse image with readout in z direction. (b) The z profile from the center line of image (a). The fitted Gaussian has a FWHM of 4.7 mm which is very close to the prescribed 5 mm slice thickness.

The bottom half of Figure 6.3 shows the corresponding eight individual coil images acquired using an $R=1$ transmit SENSE pulse. The complex sum of these eight images is the Slice 1 shown in Fig. 6.6.

Figure 6.5 shows the uniform ball phantom images acquired with both the $R=1$ transmit SENSE pulses and the SINC pulse. The histograms with FWHM measurement are shown in the bottom half. The image acquired with transmit SENSE pulses has a FWHM of 0.31 which is much smaller than the FWHM of the other three images acquired with SINC pulse. Both visual inspection and the FWHM measurement indicate the image acquired with the transmit SENSE pulses is more uniform.

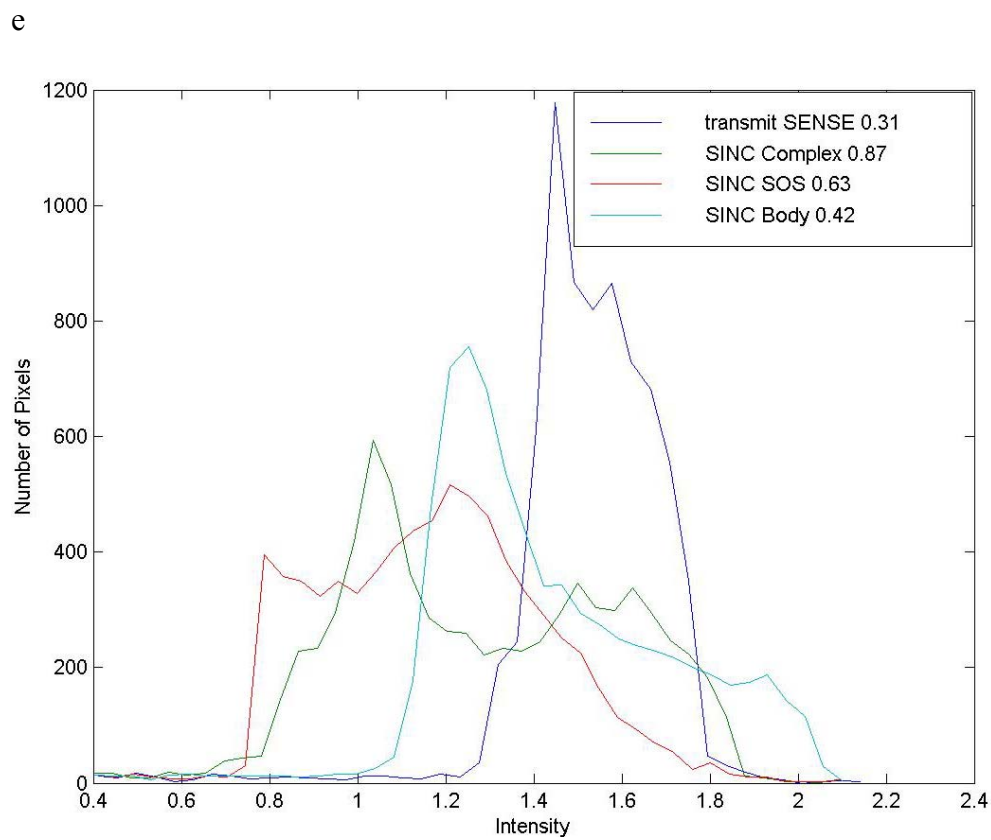
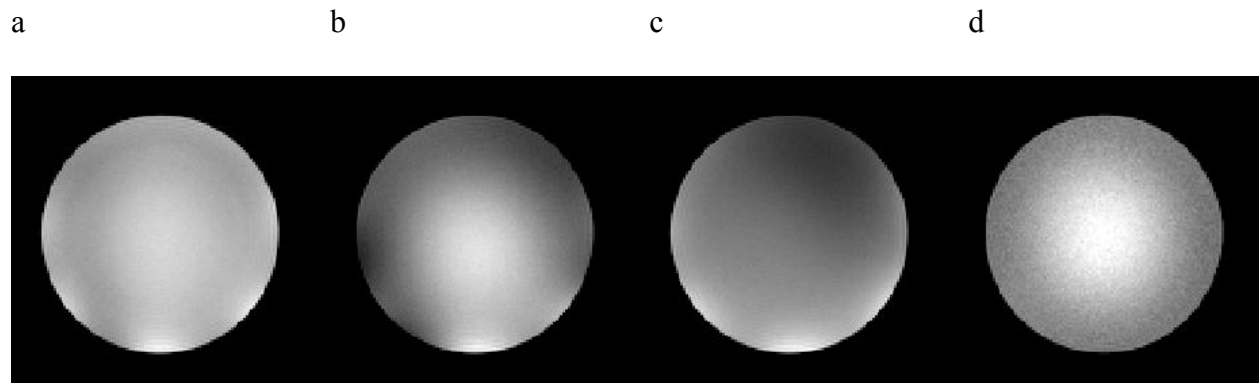


Figure 6.5: The uniform ball phantom images acquired with the transmit SENSE 3D TRF pulses (a) and the SINC pulse (b-d). The three SINC pulse images are complex sum (b) and sum of squared (c) images of the phased array receiver and the body coil receiver image (d). The histograms of the four images in (a-d) are shown in (e) with the FWHM measurements shown in the legend.

Figure 6.6 shows a comparison of four slices taken from two of the acquired using the $R=1$ transmit SENSE pulses as well as with the standard slice-select pulse. All of the images are shown with the same window and level (the magnitude sum was multiplied by 0.8 for visualization purposes). By visual inspection, the images acquired with the transmit SENSE pulses are more uniform than those obtained from either a complex or magnitude sum using the standard pulse.

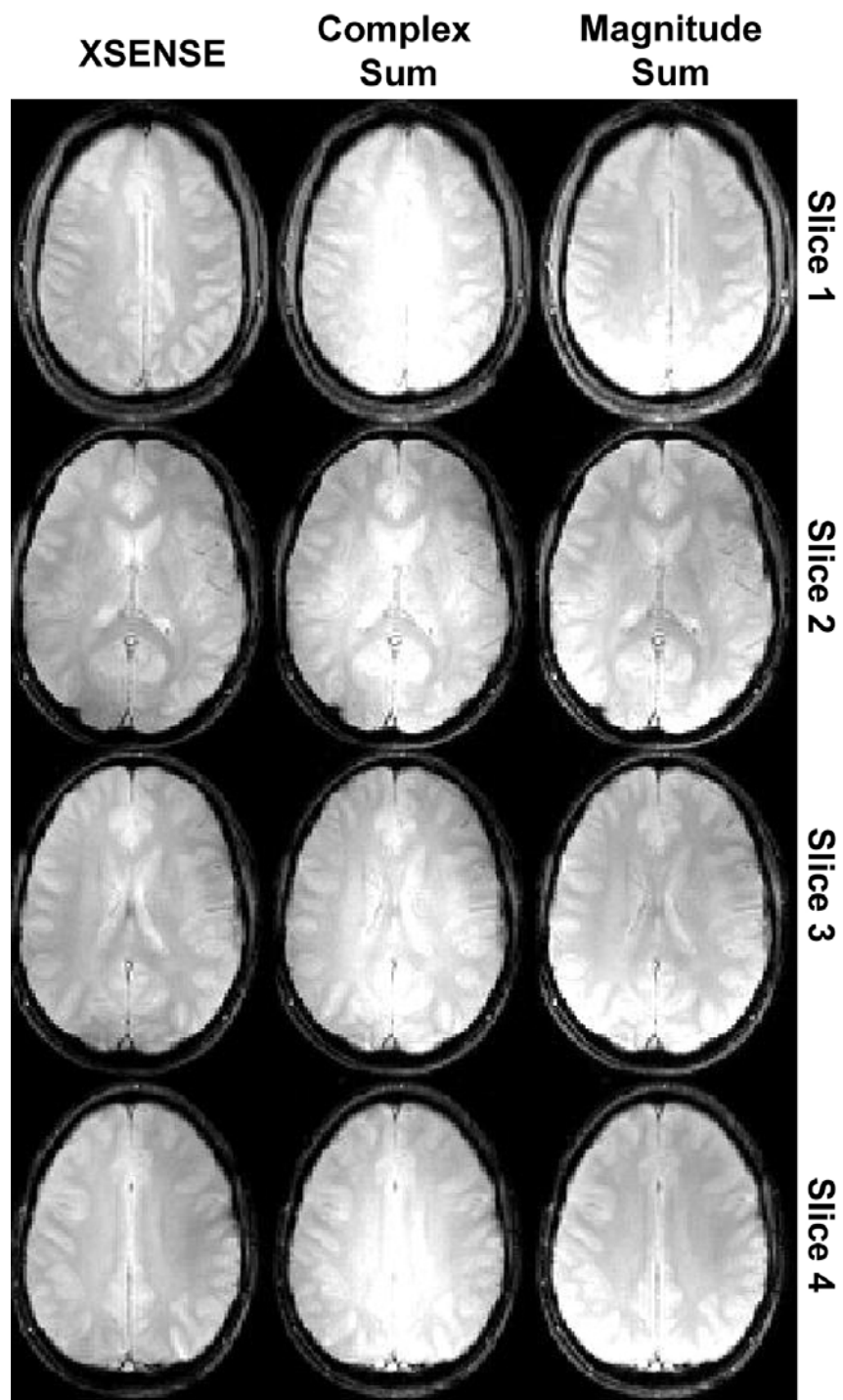


Figure 6.6: Four slices generated with the $R=1$ transmit SENSE pulses and by the complex and magnitude sums using the standard pulse. Images acquired with the transmit SENSE pulses are more uniform than those generated using the other two methods.

Figure 6.7 shows the histograms of the distribution of image magnitudes of the slices shown in Fig. 6.6. The histogram of the images generated using the transmit SENSE pulses and the complex and magnitude sums using the standard pulse are shown by the solid, dashed, and dotted lines respectively. Visual inspection shows that the histograms from the transmit SENSE images are narrower than the other methods, corresponding to a more uniform distribution of pixels. The FWHM of the histograms and the SD/Mean measurements of the slices are listed in Table 1. Both the FWHM and SD/Mean measurements of the transmit SENSE pulse images are smaller than the corresponding slices generated using the other methods. A t-test was performed comparing the FWHM and SD/Mean of the transmit SENSE slices to the slices generated with the other two methods. The subsequent p-values all indicate that the differences in means of these parameters are statistically significant.

Table 1: Full width at half maximum (FWHM) of histograms as well as standard deviations (SD) divided by the mean of the image magnitudes of the slices shown in Fig. 6.6. Also shown are p-values from a t-test between the respective column and the corresponding Transmit SENSE slices.

	FWHM			SD/Mean		
	Transmit SENSE	Complex Sum	Magnitude Sum	Transmit SENSE	Complex Sum	Magnitude Sum
Slice 1	0.16	0.22	0.17	0.13	0.17	0.17
Slice 2	0.15	0.22	0.20	0.13	0.16	0.15
Slice 3	0.15	0.27	0.19	0.12	0.16	0.15
Slice 4	0.17	0.23	0.20	0.15	0.19	0.18
Slice 5	0.15	0.26	0.25	0.15	0.18	0.15
p-value		0.0002	0.01		0.003	0.02

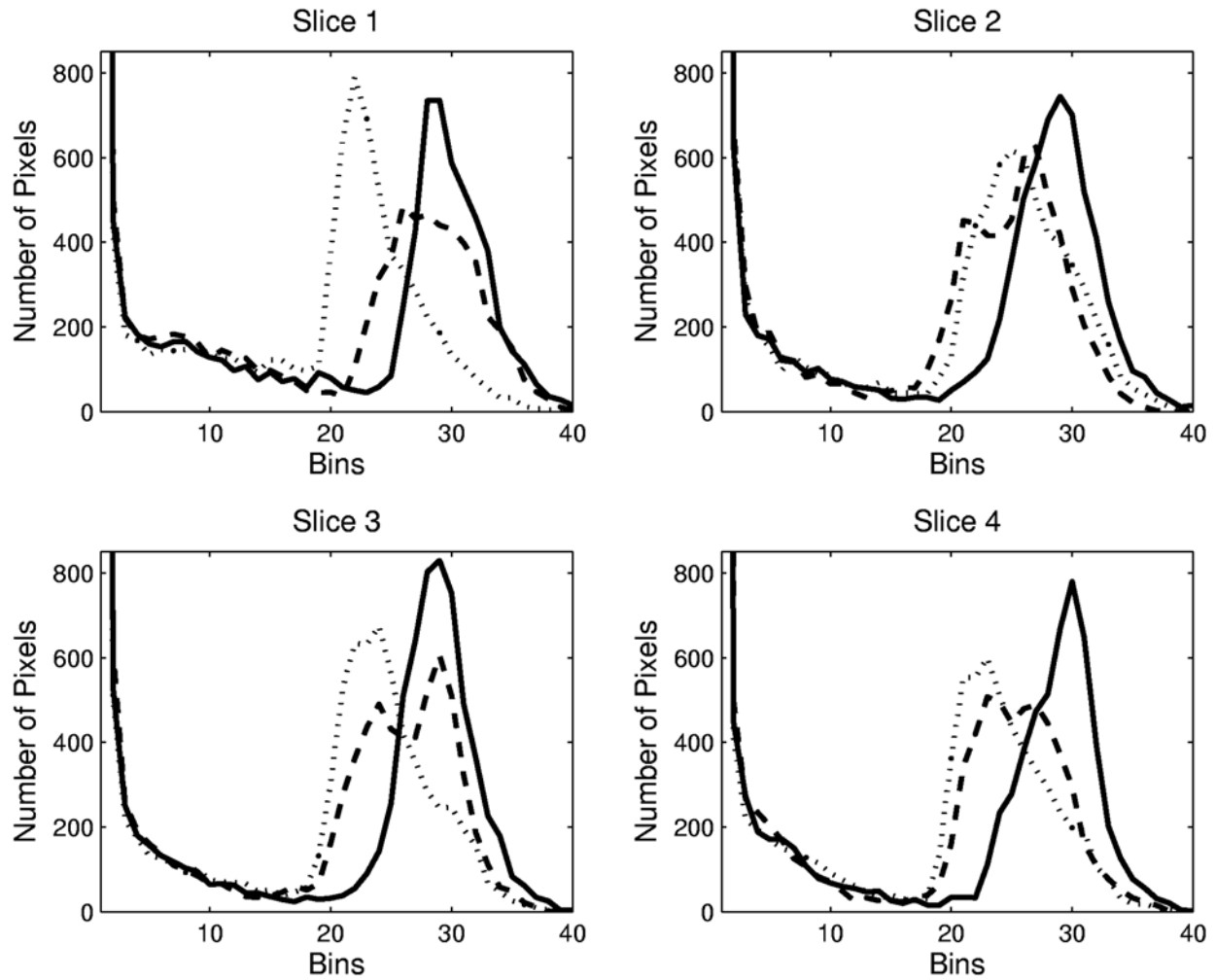


Figure 6.7: Histograms of the distribution of image magnitude among the pixels in the slices shown in Fig. 5.6. The black, dashed and dotted lines correspond to the histograms from the slices generated with the $R=1$ pulses and from the complex and magnitude sums using the standard pulse. The histograms from images acquired with the transmit SENSE pulses are narrower, indicative of a more homogeneous distribution of pixel magnitudes.

The images acquired with $R=1$ and $R=1.5$ transmit SENSE 3D TRF pulses are shown in Figure 6.8. The image of the $R=1.5$ pulses is much more uneven than that of the $R=1$ pulses.

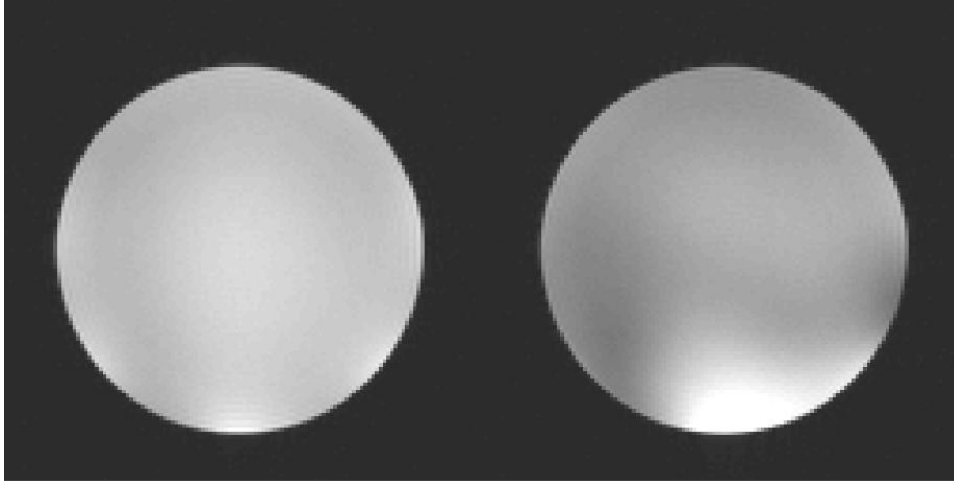


Figure 6.8: The images acquired with the R=1 (Left) and R=1.5 (Right) transmit SENSE 3D TRF pulses. The image of the R=1.5 pulses is more inhomogeneous than that of the R=1 pulses.

6.5 DISCUSSION AND CONCLUSIONS

This work presents a theoretical description of the inherent B_1 inhomogeneity compensation property of the transmit SENSE technique as well as presents proof of concept demonstration using a practical slice-select 3D TRF pulse implementation. We found a 4.3 ms long R=1 pulse with an excitation resolution and FOV of 3.7 and 22 cm provided statistically significant improvement at 3T. Higher resolution pulses were more prone to either off-resonance effects due to longer lengths in the non-accelerated pulses or aliasing residues in the accelerated pulses. Further investigation of the off-resonance properties of the fast- k_z 3D TRF design and calibration schemes need to be evaluated (67).

The limitations of this work include a lack of a demonstration using true parallel transmission hardware. As of now, the authors are aware of only a two groups that have such hardware, although the number is certainly growing. One of the groups has published that the images

obtained through complex summation and using parallel hardware are very similar (64), which supports the assumptions made in this work.

The use of parallel transmission has been mainly proposed to address the problems of ultra high field imaging such as at 7T. Although, our demonstration was at 3T and it is difficult to assess its utility at 7T, there is no theoretical reason to suggest that some implementation of transmit SENSE will not have a possible role at ultra high fields. The use of the coil sensitivity information in the transmit SENSE pulse design has the potential advantage of a more complete correction and should work readily with the receive SENSE techniques as well. Investigation into the effects of power absorption is also of great importance and will need to be evaluated before final judgment can be made.

7.0 B_0 INHOMOGENEITY CORRECTION WITH TRANSMIT SENSE 3D TRF PULSES IN ULTRA-HIGH FIELD MRI

7.1 INTRODUCTION

Susceptibility artifacts result from local field variations that usually occur at interfaces of substances with different susceptibilities. These artifacts lead to blurring (see Appendix A), distortion or even signal loss in T_2^* -weighted images (19). In the long TE BOLD fMRI images, large susceptibility artifacts usually occur in regions around the sinuses like the orbitalfrontal and inferior and medial temporal cortices, which are of significant importance for psychiatric and neuroscientific research. At higher field strengths, susceptibility artifacts will be more severe since magnetic susceptibility is proportional to field strength B_0 . (5) Many methods have been proposed to mitigate the susceptibility artifacts in T_2^* -weighted images. Image post-processing methods that include field map information in the signal equation and use segmented FFTs with conjugate phases (68,69) or conjugate gradient matrix inverting (70) are one means. A problem with the image post-processing approach is the long computing time. Gradient compensation methods tune a refocusing lobe to compensate for the static field inhomogeneity. (18,71) However, this approach requires numerous steps and leads to decreased temporal resolution. TRF pulses have also been demonstrated to be effective in susceptibility artifact reduction.(17,19,72-74) The main advantage of the 3D TRF pulse approach is the potential for a single-shot correction. The main problem of this approach, however, is the long pulse length of the TRF pulse.

In this chapter, we simulated the potential of the 3D TRF approach using the transmit SENSE pulse design method. The simulated pulse is less than 10ms long, and should be more practical to be applied in research studies or clinical investigations. Numeric simulations were shown to demonstrate that the effectiveness of the transmit SENSE 3D pulse in correcting for the intravoxel phase disperse.

7.2 THEORY

There are two types of off-resonance effects that we will be concerned with: the through-plane intravoxel dephasing in the image at TE, which is characterized as a through-plane gradient $G_z(x,y)$, and the distortion in the in-plane slice profile characterized by an off-resonance that is represented by $\Delta\omega(x,y)$ or $\Delta f(x,y)$. The through-plane intravoxel dephasing artifact is the major source of signal loss in T2* weighted imaging applications such as fMRI.

Assuming small flip angles, we still choose the “fast- k_z ” 3D TRF pulse design described in chapter 6.2. We rewrite Equation (6.2) by adding the through-plane gradient and off-resonance map mentioned above:

$$w(\mathbf{r}) = \sum_{n=1}^N w_n(\mathbf{r}) = p(z) e^{i\gamma G_z(x,y)TEz} \sum_{n=1}^N \alpha_n(x,y) q_n(x,y) e^{-i\Delta\omega(x,y)(T-t)}. \quad (7.1)$$

In this equation $\gamma G_z TEz$ is the through-plane phase at echo time TE. According to Equation(4.17), the RF waveform will be derived from the Fourier transform of this slice profile function $w(\mathbf{r})$. Since the 3D TRF pulse uses a separable design for in-plane and through-plane

directions, we can take the Fourier transform in z direction first. By the shifting theorem of Fourier transform, the first exponential term corresponds to a shift in k_z direction:

$$w(x, y, k_z) = P(k_z - \frac{\gamma}{2\pi} G_z(x, y)TE) \sum_{n=1}^N \alpha_n(x, y) q_n(x, y) e^{-i\Delta\omega(x, y)(T-t)} \quad (7.2)$$

In absence of the off-resonance map, 2D FFT can be applied to Equation (7.2) to get $W(\mathbf{k})$. However, in presence of the off- resonance map, we need to use the conjugate phase method to solve for the B_1 waveform:

$$B_{1,n}(t) = \frac{|k'_z(t)|}{\gamma} \iint_{xy} \sum_{n=1}^N \alpha_n(x, y) q_n(x, y) P(k_z - \frac{\gamma}{2\pi} G_z(x, y)TE) e^{i2\pi(xk_x(t)+yk_y(t)+\Delta f(x, y)(T-t))} dx dy \quad (7.3)$$

or we can use conjugate gradient method to solve for the RF waveform as what described in reference (46,50). The inclusion of transmit sensitivity $\alpha_n(x, y)$ can be used to reduce the pulse length and the B_1 inhomogeneity artifact as well.

7.3 METHOD

The coil sensitivities were estimated from the eight-channel phased array coil with an iterative fitting method (37) using images acquired with the body coil and from each receiver during a two-minute pre-scan. Figure 7.1 shows an example of the eight sensitivity maps for one slice in one subject.

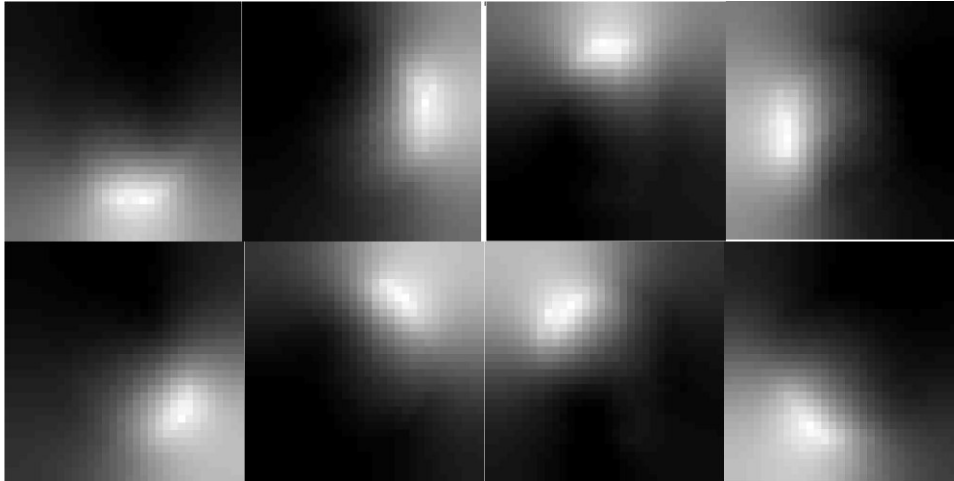


Figure 7.1: The sensitivity map from an eight-channel phased array coil.

The transmit SENSE 3D TRF pulses were computed in Matlab (Mathworks, Natick, MA) using the conjugate gradient iterative method with 15 iterations. The maximum gradient slew rate and peak were 200 T/m/sec and 40 mT/m, respectively. The z profile $p(z)$ was chosen to be a Gaussian function with a full width half maximum (FWHM) of 5 mm (i.e. the slice thickness is 5 mm).

The transmit SENSE 3D TRF pulses were evaluated with a numeric Bloch equation simulator written in the C programming language. Specifically, the Bloch equation simulator read in the magnitude and phase of the RF pulse and all three gradients in the x, y, and z directions from ASCII files outputted from the Matlab pulse design program. The output file of the Bloch equation simulator was the transverse magnetization stored in a binary file. This binary file then was read and displayed in Matlab.

For the first experiment, we demonstrated a 2D phase map correction. We excite a uniform profile with an off-resonance map from a human brain image. The through-plane excitation resolution is 2.5 mm. The in-plane excitation k -space was sampled with either 61 points (R=1) or 19 points (R=2) along a hexagonal trajectory such that there was a fixed excitation resolution of 2.4 cm over a 22 cm excitation FOV. The 3D TRF pulse length was 34.3 ms for the R=1 pulse and 10.7 ms for the R=2 pulse.

In the second experiment, we included a through-plane gradient in the pulse design. We put a synthetic gradient in the sinus region of the off-resonance map used in previous experiment. For the pulse design, we used a 1 mm through-plane excitation resolution. The in-plane excitation k -space was sampled in the same way as the previous experiment. The pulse length was 54.4 ms for the non-accelerated pulse, and 17.5 ms for the two fold accelerated transmit SENSE TRF pulse.

7.4 RESULTS

Figure 7.2 demonstrated the ability to compensate for the off-resonance frequency of the transmit SENSE 3D TRF pulses. The R=1 34.3 ms long pulse (c) and R=2 10.7 ms long pulse (d) produce the off-resonance map (b) precisely. However, the result of the R=1 10.7 ms long pulse is not as accurate as those of the other two pulses. In a real experiment, the sign of the excitation phase map will be inverted to cancel the phase on (b).

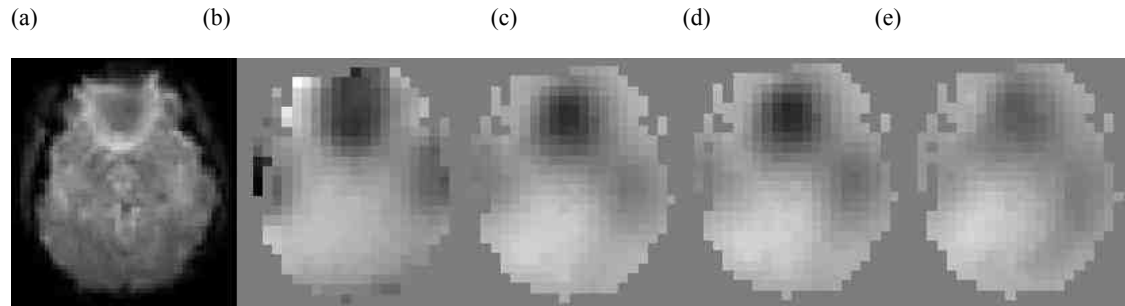


Figure 7.2: (a, b) True image and through plane phase at 3T. (c-e) Phase excitation produced by Bloch equations simulation of R=1 34.3 ms, R=2 10.7 ms, and R=1 10.7 ms transmit SENSE 3D TRF pulses, respectively. The 10.7 ms R=2 pulse produces the desired result. Note that in a real experiment we will tailor minus the phase to cancel the phase on (b).

Figure 7.3 showed the numerical simulation of the through-plane phase correction with a 54.4 ms long regular 3D TRF pulse. The magnitude and phase of the RF channel were shown in (a). The phase of the 3D transverse magnetization M_{xy} was shown in (b). The through-plane phase profile from one point in sinus region of the 3D phase in was plotted in (c). This linear phase will compensate for the introvoxle dephasing around sinus region.

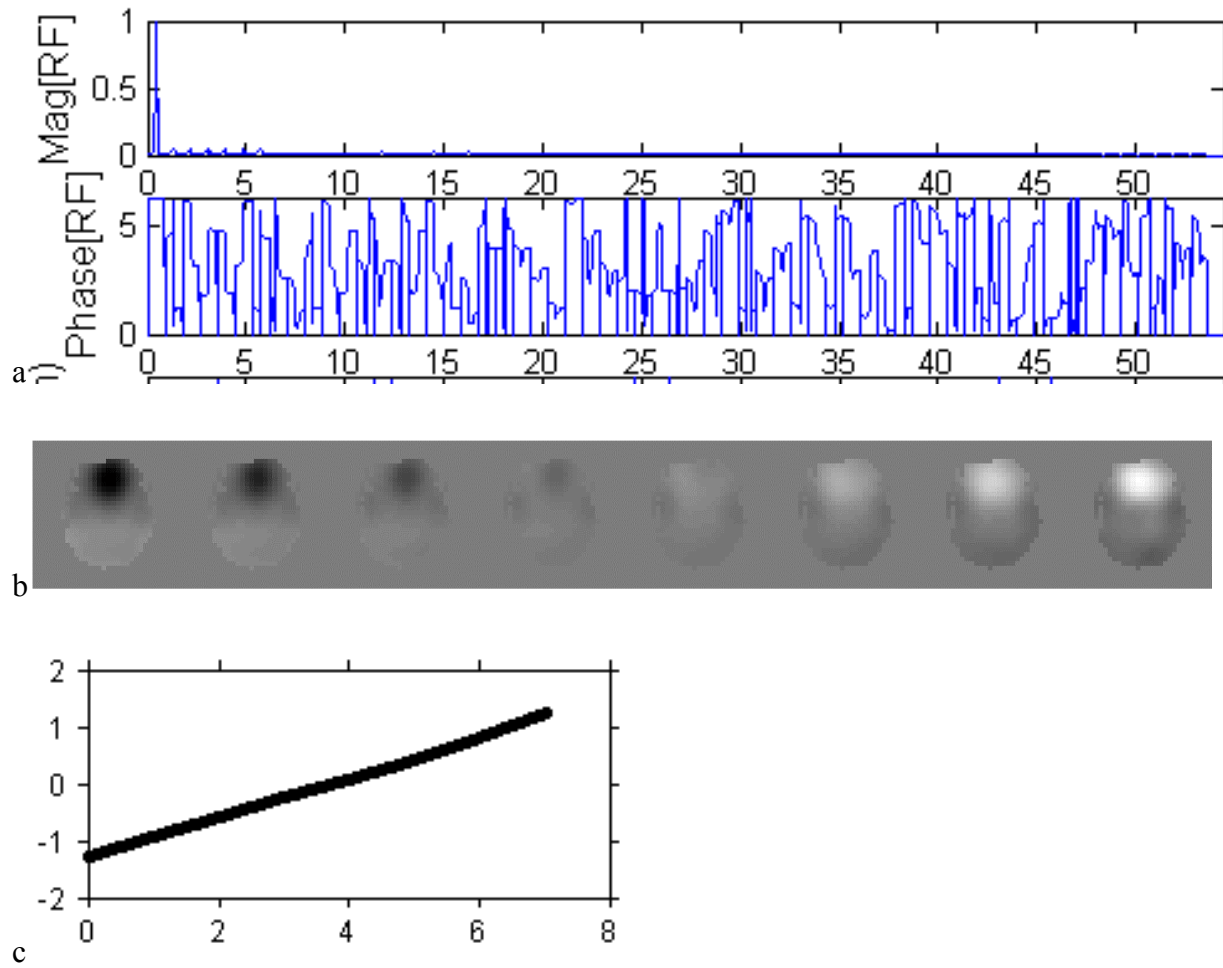


Figure 7.3: The numerical simulation with a regular 3D TRF pulse with 54.4 ms long. (a) The magnitude and phase of the 3D TRF pulses. (b) The simulated phase of the 3D transverse magnetization M_{xy} . (c) The through-plane phase profile from one point in sinus region of the simulated phase.

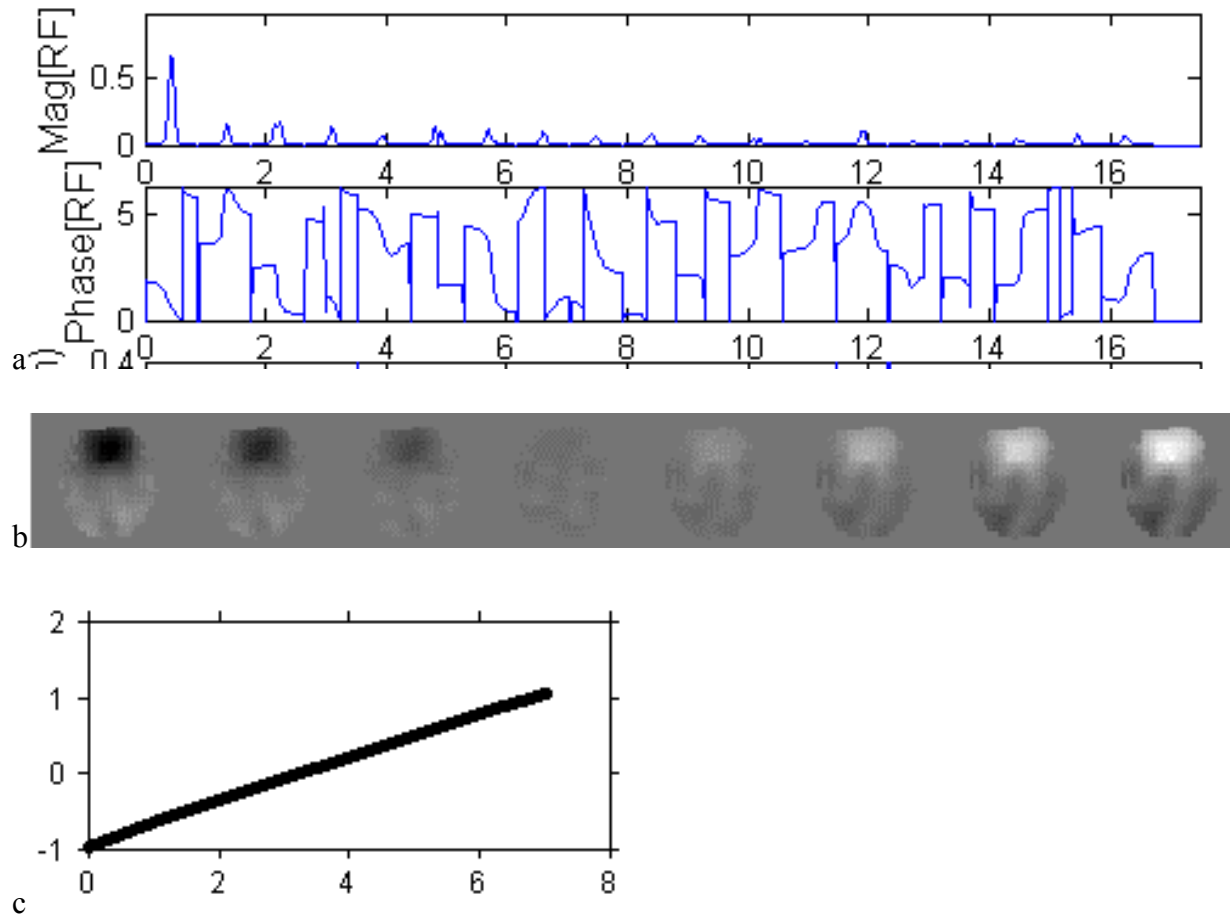


Figure 7.4: The numerical simulation with an R=2 transmit SENSE 3D TRF pulses with 17.5 ms long. (a) The magnitude and phase of one of the eight transmit SENSE 3D TRF pulses. (b) The simulated phase of the 3D transverse magnetization M_{xy} . (c) The through-plane phase profile from one point in sinus region of the simulated phase.

With the R=2 transmit SENSE technique, the same compensation for the introvoxel dephasing can be produced with 17.5 ms long pulses (Figure 7.4) as the result with the 54.4 ms long pulse. The transmit SENSE pulse is approximately 68% shorter than the regular TRF pulse.

7.5 DISCUSSION and CONCLUSIONS

This work demonstrated the potentials of the transmit SENSE 3D TRF pulses in susceptibility reduction. The 17.5 ms long transmit SENSE pulses can excite a $22 \times 22 \times 7$ cm³ FOV with a $2.4 \times 2.4 \times 0.1$ cm³ resolution. The “fast- k_z ” EPI pulse design enables the high resolution in z direction. With the inclusion of the through-plane gradient, these pulses can effectively produce a linear phase in the 3D transverse magnetization that offsets the introvoxel dephasing. With the transmit SENSE technique, the pulse length is shorten by 68% of the length of the regular 3D TRF pulse. Compared with the variable density spiral TRF pulse design proposed by Stenger *et al.*(75), which used a four-shot 19.7 ms long pulse, the pulse proposed here only need one shot through parallel transmitters and is 78% shorter. Furthmore, given the inherently B₁ inhomogeneity reduction property of the transmit SENSE pulse as discussed in the previous chapter, the pulse design method proposed here has one more advantage than the regular TRF pulse design method.

In our study we used the sensitivity information of a standard Siemens eight-channel phased array head coil to validate the pulse design method. The 17.5 ms pulse length is still a little bit too long for the clinical application. A better multi-channel transmit coil design will enable a higher reduction factor and result in a shorter pulse. Also, we should investigate to use other trajectory to sample the in-plane k -space in additional to the hexagonal trajectory we selected in this work. A possible alternative is the adaptive trajectory shown by Yip *et al.*(46)

8.0 CONCLUSIONS

B_0 and B_1 inhomogeneities are major technical problems in high field MRI. This thesis proposed methods to correct for the B_0 and B_1 inhomogeneity with transmit SENSE 3D TRF pulses on 3T scanners. The parallel transmitters were mimicked with our pseudo-transmit SENSE method using current commercial scanners with only single transmit channel and a multi-channel receiver. Below we list the key contributions.

8.1 KEY CONTRIBUTIONS

This thesis makes three major contributions. The first is the development of the pseudo-transmit SENSE method. Current commercial scanners cannot implement transmit SENSE experiments directly since there is only one independent transmit channel. In this thesis, we use the linearity of the signal equation and swap the role of the receive and transmit sensitivities, which makes it possible to use the single transmitter and a phased array receive coil to validate the transmit SENSE experiment assuming the sensitivity maps of the real parallel transmitters are the same as the maps of the phased array receiver coil. The RF waveforms corresponding to those sensitivities are transmitted through the single transmit channel of a regular commercial scanner one by one in sequential scans. In each scan, the image is acquired on the coil element with the

same sensitivity as the one built in the RF pulse. The final transmit SENSE image is the complex summation of all the individual images.

The second major contribution of this work is the exploration of the feasibility of using the transmit SENSE 3D TRF slice-select pulses for B_1 inhomogeneity reduction in high field MRI. The 3D TRF pulse uses the fast- k_z EPI pulse design that achieves thin slice-selectivity with a short pulse length. The transverse plane is sampled with hexagonal trajectories, and the transmit SENSE technique is used to accelerate the sampling in-plane if needed. By including the transmit sensitivity information, the pulse intrinsically compensates the B_1 inhomogeneity. Compared with other methods using 3D TRF pulses for B_1 inhomogeneity reduction, this technique is more straightforward and flexible. It does not need to adjust the empirical parameter in method proposed by Saekho et al. (60), and the transmit SENSE formalism can easily adjust the pulse resolution or pulse width to accommodate appropriate applications. B_1 inhomogeneity was reduced in phantom and head images with 3-5mm slice thickness using 4.3ms long transmit SENSE 3D TRF pulses, which is very promising to be used in research or the clinic.

The third contribution of this thesis is the numerical demonstration of through-plane susceptibility artifact reduction using transmit SENSE 3D TRF pulses. We showed the effectiveness of a 12.6 ms long R=2 transmit SENSE 3D TRF pulse in the susceptibility artifacts reduction in numerical simulation. Compared with the old 3D stack of spirals TRF pulse(17,19), this pulse is 40% shorter and can excite thinner slice which is more robust for clinical applications.

8.2 FUTURE DIRECTIONS

In this thesis, we already demonstrated the feasibility to use transmit SENSE 3D TRF pulse for B_1 inhomogeneity correction. However, due to the hardware limitation of current MR scanners, only few research sites can perform the real transmit SENSE experiments. Thus, the immediate next step of this research will be developing the parallel transmitter system. The parallel transmitter system needs to have multiple independent transmit channels. Each RF channel should be able to handle magnitude and phase waveforms, and also to synchronize with the gradient system and the host clock. We plan to use the TEGMAC system to develop the parallel transmitter system.

The next step is to evaluate the SAR value of the transmit SENSE experiments. Although for the B_1 inhomogeneity reduction application on 3T the SAR does not place a strong limitation since the sensitivity patterns for 3T experiments are relatively smooth, this is a critical step to lead the technique to the clinical application especially on the upcoming 7T application. Numerical simulation using the FDTD tool can be used to calculate the local and global SAR. Our collaborator, Dr. Collins from Penn State University already did some initial calculation for us. We need make this simulation a routine in our coil and pulse design to provide a robust solution for the ultimate clinical application.

Third, we need verify the effectiveness of the B_0 inhomogeneity reduction with the transmit SENSE 3D TRF pulses in phantom and in-vivo experiments. The regular 3D TRF pulses have been shown to effectively reduce the B_0 inhomogeneity. Instead of adjusting the non-uniform

magnitudes within FOV in B_1 inhomogeneity reduction application, the pulses are used to offset phase accrual in the susceptibility reduction experiments. The problem of the previous studies is the long pulse lengths of the 3D TRF pulses. Using the transmit SENSE pulse design, the pulse can be shorten to a practical length. In this work, we already showed the potentials of this technique by numerical simulation. Further evaluations on scanners should be done before it can be used in clinical applications.

APPENDIX A

OBSERVATION OF OFF-RESONANCE BLURRING IN SPIRAL IMAGING

It is well-known that the spiral image will become blurred in presence of off-resonance frequency. However, these blurring effects have not been described and quantified before.

In this study, we quantified the blurring with the FWHM of fitted Gaussian profile. Two main factors affect the blurring are: the object size and the off-resonance frequency. For a Gaussian profile, the FWHM of it is $w = 2\sqrt{2\ln 2}\sigma$. The blurred Gaussian point spread function (psf) sampled with a constant linear velocity spiral trajectory is still a Gaussian, and its FWHM is:

$$w^* = \sqrt{w^2 + \frac{(16 \cdot \ln 2 \cdot a)^2}{w^2}}, \text{ where } a = \frac{\Delta\omega \cdot T_{acq}}{k_{\max}^2} \quad (9.1)$$

where w^* is the FWHM of the blurred image, and w is the FWHM of the original object size. In Figure A.1, we plotted the relationship of w^* with respect to w and off-resonance frequency $\Delta\omega$. Figure A.2 shows the numerical simulation results of the psf's in presence of no off-resonance and a 200 Hz off-resonance frequency in (a) with different object sizes from 1 to 10 mm. The blurred FWHM vs. original FWHM was plotted in (b). The measurements from the numerical simulation are in squares, and analytical solution from equation (A.1) is in spaces. The two types

of measurements match each other as we expected. The minimal blurred FWHM is achieved for object size around 3.5 mm.

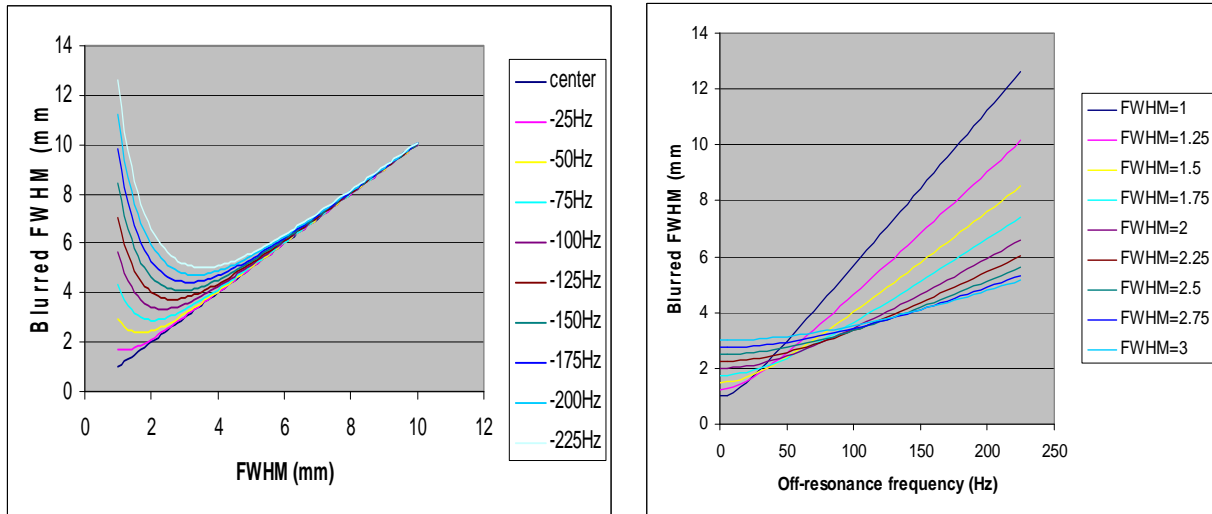


Figure A.1: The blurred FWHM vs. the original FWHM (a), and vs. the off-resonance frequency (b). At a certain off-resonance frequency, there is a minimum blurred FWHM achieved.

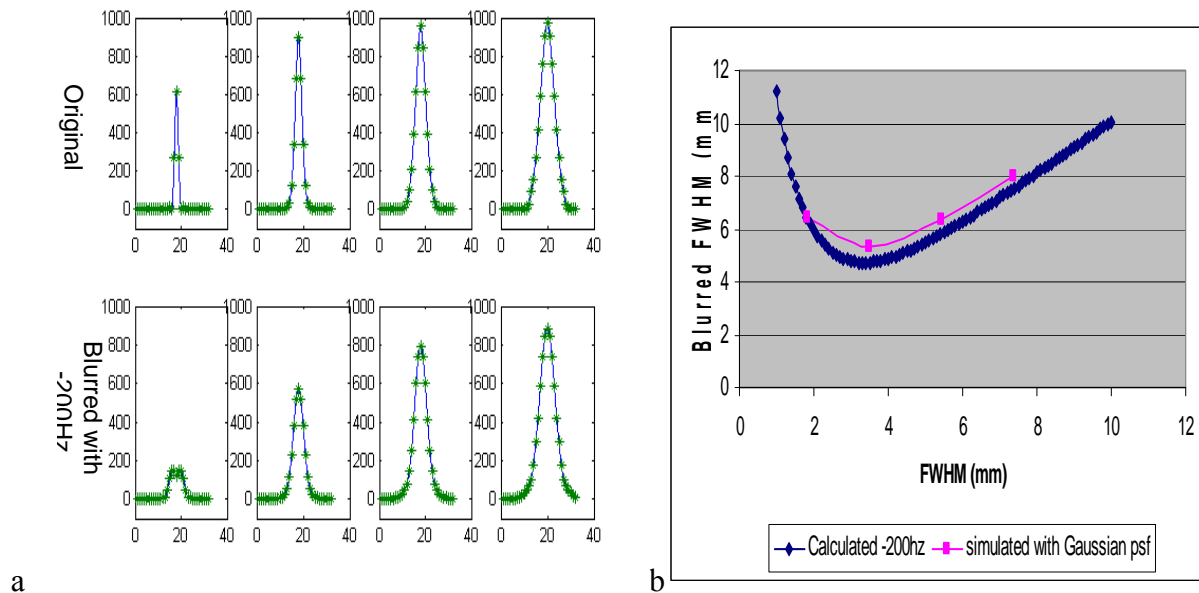


Figure A.2: Profiles of round discs (Gaussian intensity profile) with different sizes were plotted in (a). The upper row is the original profile, and the lower row is the corresponding profiles blurred with 200Hz off-resonance. The blurred FWHM vs. original FWHM was plotted in (b). The measurements from the numerical simulation are in squares, and analytical solution from equation (A.1) is in spaces. The two types of measurements match each other as we expected.

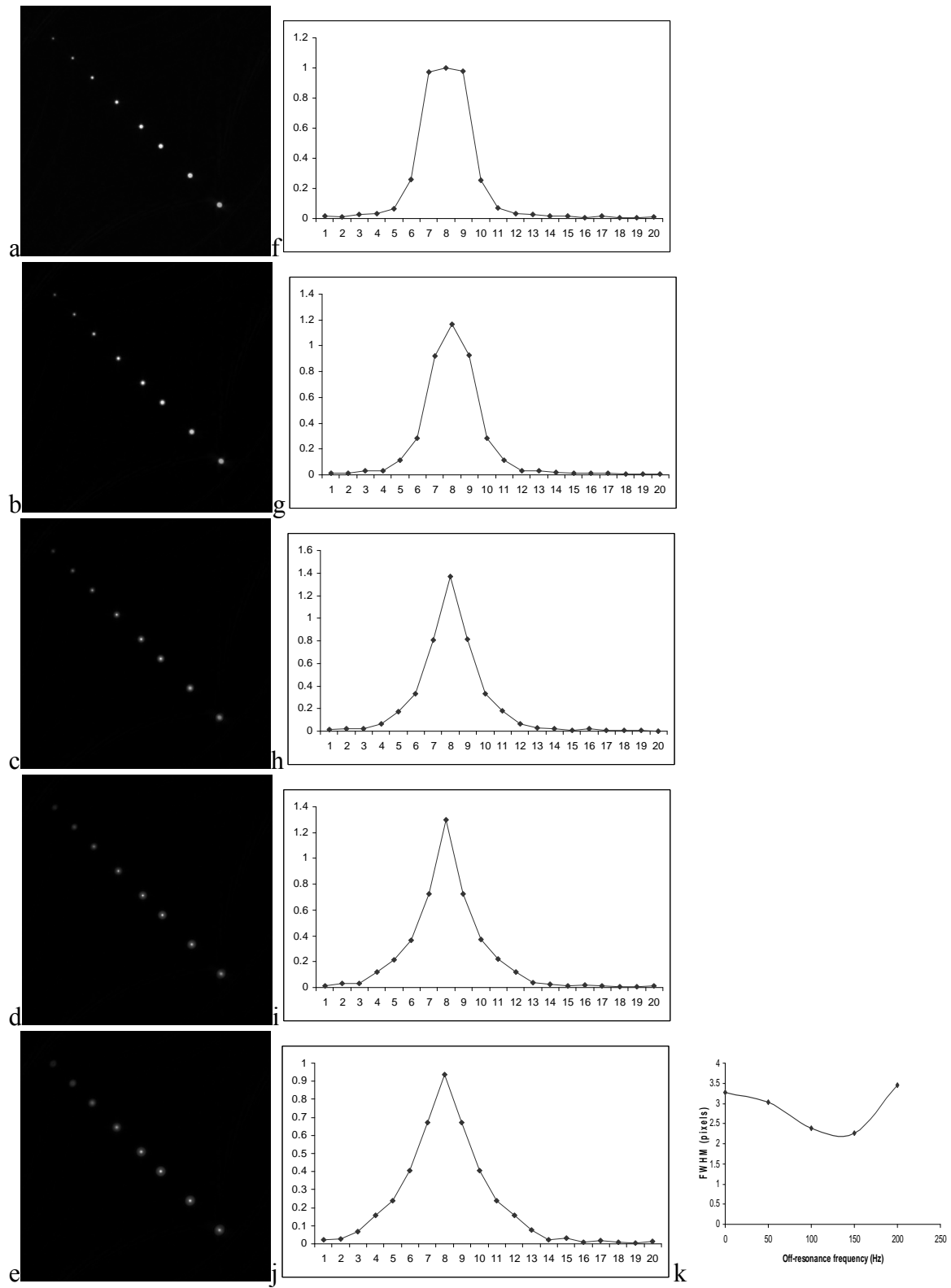
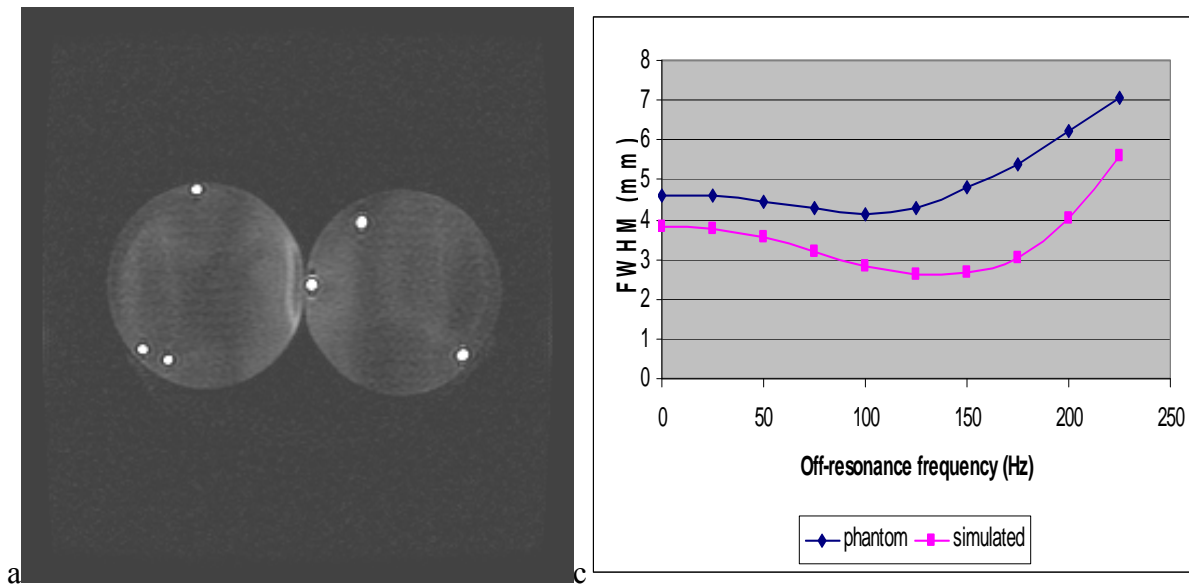


Figure A.3: Numerical simulation of round discs (rectangular profile) with different sizes ($r=1, 1.25, 1.5, 1.75, 2, 2.25, 2.5, 2.75$ pixels) were blurred with off-resonance frequency 0(a),

50Hz(b), 100Hz(c), 150Hz(d), 200Hz(e). Profiles along the round disc ($r=1.75$) were plotted correspondingly in (f-j). The blurred FWHM vs. off-resonance frequency was plotted in (k). A minimum FWHM is achieved when off-resonance is 150Hz.

Figure A.3 shows the numerical simulation of round discs (rectangular profile) with different sizes ($r=1, 1.25, 1.5, 1.75, 2, 2.25, 2.5, 2.75$ pixels) which were blurred with off-resonance frequency 0(a), 50Hz(b), 100Hz(c), 150Hz(d), 200Hz(e). Profiles along the round disc ($r=1.75$) were plotted correspondingly in (f-j). The blurred FWHM vs. off-resonance frequency was plotted in (k). A minimum FWHM is achieved when off-resonance is 150Hz.



b

Figure A.4: The bottle phantom with gadolinium filled tubes inside was imaged at the center frequency (a). The profiles along the center bright dot with different off-resonance frequencies were plotted in (b). The FWHM vs. the off-resonance frequency was plotted in (c). The phantom measurements (space) and the numerical simulation data (square) have the same trend, and the former are slightly larger than the latter. This difference might be caused by the DC component of the inhomogeneity and field variance of the scanner.

We made a phantom to verify our observation. The phantom consists of two bottle of water with tubes inside. Gadolinium doped water was filled in the tubes to generate enough contrast for measurement. The diameter of the tube is 4.5 mm. The phantom was imaged in presence of different off-resonance frequencies from 0 to 225 Hz with a 25 Hz step. The profiles along the center bright dot with different off-resonance frequencies were plotted in (b). The FWHM vs. the off-resonance frequency was plotted in (c). The phantom measurements (space) and the numerical simulation data (square) have the same trend, and the former are slightly larger than the latter. This difference might be caused by the DC component of the inhomogeneity and field variance of the scanner.

BIBLIOGRAPHY

1. Hoult D, Richards R. The signal to noise ratio of the nuclear magnetic resonance experiment. *J Magn Reson* 1976;24:71-85.
2. Edelstein WA, Glover GH, Hardy CJ, Redington RW. The intrinsic signal-to-noise ratio in NMR imaging. *Magn Reson Med* 1986;3(4):604-618.
3. Hu X, Norris DG. Advances in high-field magnetic resonance imaging. *Annu Rev Biomed Eng* 2004;6:157-184.
4. Ogawa S, Lee T, Nayak A, Glynn P. Oxygenation-sensitive contrast in magnetic resonance image of rodent brain at high magnetic fields. *Magn Reson Med* 1990;14:68-78.
5. Elster AD. How much contrast is enough?. Dependence of enhancement on field strength and MR pulse sequence. *Eur Radiol* 1997;7 Suppl 5:276-280.
6. Frayne R, Goodyear BG, Dickhoff P, Lauzon ML, Sevick RJ. Magnetic resonance imaging at 3.0 Tesla: challenges and advantages in clinical neurological imaging. *Invest Radiol* 2003;38(7):385-402.
7. Kim DS, Garwood M. High-field magnetic resonance techniques for brain research. *Curr Opin Neurobiol* 2003;13(5):612-619.
8. Scarabino T, Nemore F, Giannatempo GM, Bertolino A, Di Salle F, Salvolini U. 3.0 T magnetic resonance in neuroradiology. *Eur J Radiol* 2003;48(2):154-164.
9. Barth M, Metzler A, Klarhofer M, Roll S, Moser E, Leibfritz D. Functional MRI of the human motor cortex using single-shot, multiple gradient-echo spiral imaging. *Magn Reson Imaging* 1999;17(9):1239-1243.
10. Chen YC, Mandeville JB, Nguyen TV, Talele A, Cavagna F, Jenkins BG. Improved mapping of pharmacologically induced neuronal activation using the IRON technique with superparamagnetic blood pool agents. *J Magn Reson Imaging* 2001;14(5):517-524.
11. Vaughan J, Adriany G, Garwood M, Yacoub E, Duong T, DelaBarre L, Anderson P, Ugurbil K. Detunable transverse electromagnetic (TEM) volume coil for high-field NMR. *Magn Reson Med* 2002;47:990-1000.

12. Ruggieri PM, Laub GA, Masaryk TJ, Modic MT. Intracranial circulation: pulse-sequence considerations in three-dimensional (volume) MR angiography. *Radiology* 1989;171(3):785-791.
13. Collins CM, Li S, Smith MB. SAR and B1 field distributions in a heterogeneous human head model within a birdcage coil. Specific energy absorption rate. *Magn Reson Med* 1998;40(6):847-856.
14. Schwarz AJ, Rijpkema M, Collins DJ, Payne GS, Prock T, Woodward AC, Heerschap A, Leach MO. SAR and tissue heating with a clinical (31)P MRS protocol using surface coils, adiabatic pulses, and proton-decoupling. *Magn Reson Med* 2000;44(5):692-700.
15. Yang QX, Wang J, Zhang X, Collins CM, Smith MB, Liu H, Zhu XH, Vaughan JT, Ugurbil K, Chen W. Analysis of wave behavior in lossy dielectric samples at high field. *Magn Reson Med* 2002;47(5):982-989.
16. Ibrahim TS, Lee R, Abduljalil AM, Baertlein BA, Robitaille PM. Dielectric resonances and B(1) field inhomogeneity in UHFMRI: computational analysis and experimental findings. *Magn Reson Imaging* 2001;19(2):219-226.
17. Stenger VA, Boada FE, Noll DC. Three-dimensional tailored RF pulses for the reduction of susceptibility artifacts in T2*-weighted functional MRI. *Magn Reson Med* 2000;44:525-531.
18. Yang Q, Dardzinski B, Li S, Eslinger P, Smith M. Removal of local field gradient artifacts in T2*-weighted images at high fields by gradient-echo slice excitation profile imaging. *Magn Reson Med* 1998;39:402-409.
19. Stenger VA, Boada FE, Noll DC. Multishot 3D slice-select tailored RF pulses for MRI. *Magn Reson Med* 2002;48:157-165.
20. Alsop D, Connick T, Mizsei G. A spiral volume coil for improved RF field homogeneity at high static magnetic field strength. *Magn Reson Med* 1998;40:49-54.
21. Chen J, Feng Z, Jin JM. Numerical simulation of SAR and B1-field inhomogeneity of shielded RF coils loaded with the human head. *IEEE Trans Biomed Eng* 1998;45(5):650-659.
22. Lauterbur PC. Image Formation by Induced Local Interactions: Examples Employing Nuclear Magnetic Resonance. *Nature* 1973;242:190-191.
23. Kumar A. WD, Ernst P.R. NMR Fourier Zeugmatography. *J Magn Reson* 1975;18:69-83.

24. Haacke EM, Brown R.W.,Thompson M.R., Venkatesan R. . Magnetic Resonance Imaging: Physical Principles and Sequence Design. New York: John Wiley & Sons, Inc; 1999.
25. Liang Z-P, Lauterbur, P.C. Principles of Magnetic Resonance Imaging: A Signal Processing Perspective. New York: IEEE Press; 2000.
26. Nishimura D. Principles of Magnetic Resonance Imaging; 1995.
27. Pruessmann KP, Weiger M, Scheidegger MB, Boesiger P. SENSE: Sensitivity encoding for fast MRI. Magnetic Resonance in Medicine 1999;42:952-962.
28. Sodickson DK, Manning WJ. Simultaneous acquisition of spatial harmonics (SMASH). Magnetic Resonance in Medicine 1997;38:591-603.
29. Meijering E. A Chronology of Interplotation From Ancient Astronomy to Modern Signal and Image Processing. Proc IEEE 2002(90).
30. Heidemann RM, Griswald MA, Haase A, Jakob PM. VD-AUTO-SMASH Imaging. Magnetic Resonance in Medicine 2001;45:1066-1074.
31. Sodickson DK, McKenzie CA. A generalized approach to parallel magnetic resonance imaging. Med Phys 2001;28(8):1629-1643.
32. Jakob PM, Griswold MA, Edelman RR, Sodickson DK. AUTO-SMASH: a self-calibrating technique for SMASH imaging. SiMultaneous Acquisition of Spatial Harmonics. Magma 1998;7(1):42-54.
33. Griswold MA, Jakob PM, Heidemann RM, Nittka M, Jellus V, Wang J, Kiefer B, Haase A. Generalized autocalibrating partially parallel acquisitions (GRAPPA). Magn Reson Med 2002;47(6):1202-1210.
34. McKenzie CA, Yeh EN, Ohliger MA, Price MD, Sodickson DK. Self-calibrating parallel iaging with automatic coil sensitivity extraction. Magnetic Resonance in Medicine 2002;47:529-538.
35. Qian Y, Zhang Z, Stenger VA, Wang Y. Self-calibrated spiral SENSE. Magn Reson Med 2004;52(3):688-692.
36. Qian Y, Zhang Z, Wang Y, Boada FE. Decomposed direct matrix inversion for fast non-cartesian SENSE reconstructions. Magn Reson Med 2006.
37. Fessler JA. Penalized weighted least-squares image reconstruction for positron emission tomography. IEEE Trans Med Imaging 1994;13(4):290-300.

38. Pauly JM, Hu BS, Wang SJ, Nishimura DG, Macovski A. A Three Dimensional Spin-Echo or Inversion Pulse. *Magnetic Resonance in Medicine* 1993;29:2-6.
39. Pauly JM, Nishimura D, Macovski A. A k-space analysis of small-tip-angle excitation. *J Magn Reson* 1989;81:43-56.
40. Pauly J, Nishimura D, Macovski A. A Linear Class of Large Tip-Angle Selective Excitation Pulses. *Journal of Magnetic Resonance* 1989;82:571-587.
41. Zhu Y. RF power reduction with parallel excitation. 2004; Kyoto. p 331.
42. Yip C-P, Fessler J, Noll D. A constrained minimization approach to designing multi-dimensional, spatially selective RF pulses. 2004; Kyoto. p 188.
43. Saekho S, Boada FE, Noll DC, Stenger VA. A Small Tip Angle 3D Tailored RF Slab-Select Pulse For Reduced B1 Inhomogeneity at 3T. *Magn Reson Med* 2005;53:479-484.
44. Katscher U, Rohrs J, Bornert P. Basic considerations on the impact of the coil array on the performance of Transmit SENSE. *Magma* 2005;18(2):81-88.
45. Pauly JM. Course Notes: EE469B: RF Pulse Design for Magnetic Resonance Imaging (<http://www.stanford.edu/class/ee469b/>). 2004.
46. Yip C-P, Fessler JA, Noll DC. A Novel Fast and Adaptive Trajectory in Three-Dimensional Excitation k-Space. 2005; Miami, Florida, USA. p 2350.
47. Katscher U, Bornert P, Leussler C, van den Brink J. Transmit SENSE. *Magn Reson Med* 2003;49(1):144-150.
48. Zhu Y. Parallel excitation with an array of transmit coils. *Magn Reson Med* 2004;51(4):775-784.
49. Griswold MA, Kannengiesse S, Muller M, Jakob PM. Autocalibrated Accelerated Parallel Excitation (Transmit-GRAPPA). 2005; Miami, FL. p 2435.
50. Grissom W, Yip C-P, Zhang Z, Stenger VA, Fessler JA, Noll DC. A Spatial Domain Method for the Design of RF Pulses in Multi-Coil Parallel Excitation. *Magn Reson Med* Accepted.
51. Zhang Z, Stenger VA. Validate of Transmit SENSE with Reciprocity. 2005; Miami. p 2434.
52. US Food and Drug Administration. Guidance for Industry and FDA Staff: Criteria for Significant Risk Investigations of Magnetic Resonance Diagnostic Devices. 2003.

53. Bottomley P, Andrews E. RF magnetic field penetration, phase shift and power dissipation in biological tissue: Implications for NMR imaging. *Phys Med Biol* 1978;23:630-643.
54. Glover GH, Hayes CE, Pelc NJ, Edelstein WA, Mueller OM, Hart HR, Hardy CJ, O'Donnell M, Barber WD. Comparison of linear and circular polarization for magnetic resonance imaging. *J Magn Reson* 1985;64:255-270.
55. Collins CM, Liu W, Schreiber W, Yang QX, Smith MB. Central brightening due to constructive interference with, without, and despite dielectric resonance. *J Magn Reson Imaging* 2005;21(2):192-196.
56. Jin J, Chen J. On the SAR and field inhomogeneity of birdcage coils loaded with the human head. *Magn Reson Med* 1997;38:953-863.
57. Staewen R, Johnson A, Ross B, Parrish T, Merkle H, Garwood M. 3-D FLASH imaging using a single surface coil and a new adiabatic pulse, BIR-4. *Invest Radiol* 1990;25:559-567.
58. Cohen MS, DuBois RM, Zeineh MM. Rapid and effective correction of RF inhomogeneity for high field magnetic resonance imaging. *Hum Brain Mapp* 2000;10(4):204-211.
59. Deichmann R, Good C, Turner R. RF inhomogeneity compensation in structural brain imaging. *Magn Reson Med* 2002;47:398-402.
60. Saekho S, Yip CY, Noll DC, Boada FE, Stenger VA. Fast- k_z three-dimensional tailored radiofrequency pulse for reduced B1 inhomogeneity. *Magn Reson Med* 2006;55(4):719-724.
61. Collins CM, Liu W, Swift BJ, Smith MB. Combination of optimized transmit arrays and some receive array reconstruction methods can yield homogeneous images at very high frequencies. *Magn Reson Med* 2005;54(6):1327-1332.
62. King SB, Duensing GR, Varosi S, Peterson D, Molyneaux DA. A four channel transceive phased array head coil for 3T.; 2001; Glasgow, Scotland. p 12.
63. Stenger V, Zhang Z, Yu S, Boada F. B1 Inhomogeneity reduction with transmit SENSE. 2004; Zurich, Switzerland.
64. Ullmann P, Junge S, Wick M, Seifert F, Ruhm W, Hennig J. Experimental analysis of parallel excitation using dedicated coil setups and simultaneous RF transmission on multiple channels. *Magn Reson Med* 2005;54(4):994-1001.
65. Hoult D. The principle of Reciprocity in Signal Strength Calculations-A Mathematical Guide. *Concepts in Magnetic Resonance* 2000;12:173-187.

66. Wang J, Qiu M, Yang QX, Smith MB, Constable RT. Measurement and correction of transmitter and receiver induced nonuniformities in vivo. *Magn Reson Med* 2005;53(2):408-417.
67. Oelhafen M, Pruessmann KP, Kozerke S, Boesiger P. Calibration of echo-planar 2D-selective RF excitation pulses. *Magn Reson Med* 2004;52(5):1136-1145.
68. Noll D, Pauly J, Meyer C, Nishimura D, Macovski A. Deblurring for non-2D Fourier transform magnetic resonance imaging. *Magn Reson Med* 1992;25(2):319-333.
69. Noll DC, Meyer CH, Pauly JM, Nishimura DG, Macovski A. A homogeneity correction method for magnetic resonance imaging with time-varying gradients. *IEEE Trans Med Imaging* 1991;10(4):629-637.
70. Sutton BP, Noll DC, Fessler JA. Fast, iterative image reconstruction for MRI in the presence of field inhomogeneities. *IEEE Trans Med Imaging* 2003;22(2):178-188.
71. Constable RT. Functional MR imaging using gradient-echo echo-planar imaging in the presence of large static field inhomogeneities. *J Magn Reson Imaging* 1995;5(6):746-752.
72. Cho Z, Ro Y. Reduction of susceptibility artifact in gradient-echo imaging. *Magn Reson Med* 1992;23:193-200.
73. Glover G, Lai S. Reduction of susceptibility effects in BOLD fMRI using tailored RF pulses. 1998. p 298.
74. Stenger VA, Santos R, Boada FE, Noll DC. Simulated Multi-Dimensional RF Excitation for Reducing Susceptibility Artifacts in fMRI Acquisitions at 3 Tesla. 1999. p 2080.
75. Stenger VA, Boada FE, Noll DC. Variable-density spiral 3D tailored RF pulses. *Magn Reson Med* 2003;50(5):1100-1106.